Università degli Studi di Trento
Facoltà di Scienze Matematiche
Fisiche e Naturali
Dipartimento di Fisica

Tesi di Dottorato di Ricerca in Fisica
Ph.D. Thesis in Physics

Study of Ultracold Fermi Gases in the BCS-BEC Crossover: Quantum Monte Carlo Methods, Hydrodynamics and Local Density Approximation.

Candidato
Gianluca Bertaina

Relatore
Prof. Stefano Giorgini

Dottorato di Ricerca in Fisica, XXIII ciclo
Trento, 13 Dicembre 2010

A Michela
e alla nuova vita dentro di lei.

Acknowledgments

I would like to thank my supervisor Prof. Stefano Giorgini for his scientific support, for encouraging me and advising me on researchers' life. I am grateful to Prof. Sandro Stringari for giving me the possibility of studying in the INO-CNR Bose-Einstein Condensation Center in Trento. This gave me the unique opportunity of very interesting scientific discussions at international level. I would like to thank Prof. Lev Pitaevskii, for his patience and love of Physics.

I thank all the present and former members of the BEC group with whom I shared scientific discussions, especially Sebastiano Pilati, Alessio Recati, Iacopo Carusotto, Francesco Piazza, Francesco Bariani, Gregory Astrakharchik. More importantly, I received a warm welcome by each member of the group, and I am grateful for this friendly atmosphere. Many thanks also to the secretaries Beatrice Ricci, Luisa Rossi Doria, Micaela Paoli for their support, and to the Department of Physics.

I would like to thank also all the Ph.D. students in Povo whom I met, especially those in my office: Paolo Armani (king of computers and Monte Carlo), Raffaele Millo, Emmanuel Autieri, Daniele Nicolodi. Among the others Marco Zanatta, Giacomo Gradenigo, Ilaria Dorigatti, Silvia Marchesi. I also acknowledge the enthusiasm of the members of ADI Trento.

Last but not the least I thank my wife Michela for this wonderful year in Trento with her and for her patience.

Contents

List of Figures

Chapter 1

Introduction

In this Thesis we will theoretically address some issues concerning the Physics of ultracold Fermi gases, all of them with experimental relevance. The field of ultracold gases, and more recently of ultracold Fermi gases, is gathering a lot of experimental and theoretical interest for two main reasons: the great control on the relevant parameters of the problem and the relative simplicity of the minimal theory which is able to correctly describe the system. Building upon this solid background, ultracold gases provided an ideal laboratory for testing more refined theories and also for addressing fundamental issues of quantum mechanics as well as for simulating more complex physical systems such as those encountered in condensed matter.

Even if the effective hamiltonian of ultracold gases can be simple, due to the diluteness of the system and the low temperature, which imply low energy physics, the solution of the quantum mechanic equations governing the state of these systems is not always simple. For the static properties usually mean-field solutions exist or perturbative expansions can be produced in some regimes. However Quantum Monte Carlo (QMC) techniques provide more accurate results especially in the strongly interacting regimes. For confined systems it is possible to use QMC only for a few particles, so that, for large number of particles, a fruitful combined use of Density Functional Theory (DFT) and QMC is necessary. The study of the dynamics of ultracold gases has received little attention with QMC techniques, due to the intrinsic computational difficulty of the many-body problem, so that general hydrodynamic equations are often used for studying the propagation of smoothly varying perturbations.

In this Thesis we use QMC techniques for studying the problem of ferromagnetism in repulsive or effectively repulsive ultracold gases without a lattice and the problem of the Bardeen-Cooper-Schrieffer to Bose-Einstein-Condensation (BCS-BEC) crossover in two dimensions. We use DFT in the Local Density Approximation (LDA) for calculating the density profiles of ultracold Fermi gases in harmonic magneto-optical traps, starting from

QMC equations of state. We study the propagation of first and second sound in ultracold Fermi gases in cylindrical geometry, using the hydrodynamic equations of superfluids.

The first project, which we report in Chap. 3, concerns itinerant ferromagnetism in fermionic gases in three dimensions. We study a system with two species of fermions with attractive interaction, but in an excited state with effective repulsion between the fermions. These results are compared to those obtained with a purely repulsive model. The aim of the research is to find the critical interaction at which a ferromagnetic transition takes place, even in the absence of a lattice (itinerant ferromagnetism). We study the magnetic susceptibility with increasing interaction, up to the divergence, signaling the quantum phase transition. We also characterize the polarized system, introducing a polaronic picture for high polarization.

The results we obtain are relevant in the present experimental and theoretical research concerning magnetism and superfluidity in the field of ultracold gases, but also in relation to solid state physics, where there is still a debate concerning the role of the lattice in ferromagnetic phenomena.

The second project, which we report in Chap. 4, concerns the study of an attractive Fermi gas in two dimensions, with the change in strength of the interaction. This system shows the crossover from a superfluid BCS regime to a BEC of molecules. Using Diffusion Monte Carlo we calculate such observables as the energy per particle and the gap in the excitation spectrum, finding an accurate description in the strongly interacting regime; moreover we verify a property concerning the short range nature of the interaction (Tan's relation).

This study is of relevance for ongoing and in-preparation experiments involving ultracold gases optically trapped in planar geometry, and it addresses the general topic of the interplay between geometry and superfluidity.

The third project, which we report in Chap. 5, concerns the density profiles of ultracold trapped Fermi gases with population imbalance in the strongly interacting regime of the BCS-BEC crossover in three dimensions. We use LDA and the equations of state of uniform polarized Fermi gases found with QMC, to quantitatively characterize the various shapes of the density profiles as a function of interaction and the global population imbalance. We interpret the density jumps in the profiles as signals of a quantum phase transition from a normal to a superfluid gas driven by population imbalance (Chandrasekhar-Clogston limit), finding good agreement with experiments.

This study is relevant in interpreting the results in experiments concerning imbalanced Fermi gases and in validating both the LDA approach and the QMC equations of state for this system.

The fourth project, which we report in Chap. 6, concerns the study of cylindrically trapped strongly interacting Fermi gases. By using the hydrodynamic equations and LDA, we characterize the low frequency modes

(sound) with the change of temperature and the phase of the system. We find peculiar differences with respect to uniform systems, depending on the role of the dissipative terms in the hydrodynamic equations.

This study is relevant for future experiments aiming at the characterization of second sound in ultracold Fermi gases; moreover it again focuses on the interplay between viscosity and geometry.

The results in this Thesis are published in three papers [PBGT10, BG09, BPS10] and a preprint [BG10].

In the rest of this introduction we review some general facts and theories concerning ultracold Fermi gases. In Chap. 2 we provide a self-contained introduction to the Variational and Diffusion Monte Carlo methods we use. In Chapters 3 - 6 we report and discuss the results concerning the previously outlined problems. In Chap. 7 we draw the conclusions.

1.1 Ultracold gases

From the experimental point of view, the field of ultracold gases has profited from the research in optics and in atomic and molecular physics. Laser cooling and optical and magnetic trapping allowed for the manipulation of large numbers of atoms; the use of Feshbach resonances, for changing the effective interaction between atoms, allowed for the exploration of many-body physics with a high degree of control.

From the theoretical point of view, ultracold gases allowed for the simulation of long standing models and the verification of theoretical predictions which were pure speculation before, in particular related to the Bose-Einstein condensation (BEC) of Bose gases [AEM$^+$95, BSTH95, DMA$^+$95] and to the crossover from Bardeen-Cooper-Schrieffer to Bose-Einstein condensation (BCS-BEC) in Fermi gases [BAR$^+$04, BKC$^+$04, RGJ04, ZSS$^+$04].

Excellent reviews, which we refer to for the rich bibliography related to this growing field of research, introduce to experimental and theoretical aspects of ultracold gases [PS02, PS03, BDZ08] and in particular to Bose gases [DGS99, Leg01] and to Fermi gases [GPS08, KZ08].

The physical regime of ultracold gases is characterized by diluteness and low temperature, in terms of three length scales: the range of the interaction R (we do not consider here long range interactions); the mean interparticle distance $l \approx n^{-d}$, n being the particle density and d the dimensionality; the thermal de Broglie wavelength $\lambda_T = \sqrt{\hbar/2\pi m k_B T}$, k_B being the Boltzmann constant, m the mass of an atom and T the temperature. The condition of diluteness is expressed by the inequality $R \ll l$, while the temperature can be considered low if $R \ll \lambda_T$: under these two conditions the scattering of particles is universal, not depending on the details of the interatomic potential, but only on the lowest angular momentum scattering length a. In case of bosons or fermions of different species the s-wave scattering length is

the only relevant interaction parameter. When theoretically treating these systems, pseudo-potential methods have been widely used [HY57, OP01], while in this Thesis, for the microscopic calculations at zero temperature, we use short range interactions such as the square well, hard sphere or soft sphere potentials, in the universal regime $nR^d \ll 1$.

While for relatively high temperatures ultracold gases can be treated as classical gases, for very low temperatures these systems enter the quantum degeneracy regime, where the statistics of particles plays a relevant role. This physically very interesting regime is characterized by the inequality $l \lesssim \lambda_T$. Since λ_T can be considered as the size of the wavepacket corresponding to a particle, the previous inequality corresponds to the loss of distinguishability of nearby particles.

Below the degeneracy temperature, depending on statistics, interactions, dimensionality and population imbalance, ultracold gases can undergo a superfluid phase transition. Superfluid systems show spectacular coherence phenomena, which are described in the previously cited reviews. A complex order parameter Ψ can be introduced, whose phase θ is related to a macroscopic irrotational superfluid velocity $v_s \propto \nabla\theta$. In case of bosons in the weakly interacting regime, the order parameter obeys the Gross-Pitaevskii equation [Pit61, Gro61] and its modulus square can be interpreted as the density of the system. In case of weakly attractive fermions an analogous role is played by the Bogoliubov-de Gennes equations [De 66]. The equations of hydrodynamics of superfluids [Kha65] are able to describe these systems at a macroscopic level even in the strongly interacting regime, provided local thermal and mechanical equilibrium are achieved, that is only when sufficiently smooth and slow perturbations in the density are considered; however a precise preliminary derivation of the equation of state at equilibrium is required.

1.2 Bose-Einstein condensation and Cooper pairing

The correlation functions of ultracold gases can be characterized by off-diagonal long range order (ODLRO) [Yan62], a property which is related to superfluidity and implies it. ODLRO is caused by a macroscopic occupancy of single particle orbitals (in case of bosons) or two-particle orbitals (in case of two species of fermions with attractive interaction). At zero temperature, both in three and two dimensions, ODLRO in a bosonic (fermionic) system manifests itself by a non vanishing value of the off-diagonal sector of the one-body (two-body) density matrix. In case of bosons this phenomenon is called Bose-Einstein condensation [Bos24, Ein25], while in case of fermions with attractive interaction it is called condensation of Cooper pairs (from the Bardeen-Cooper-Schrieffer theory of superconductivity [BCS57]).

Let us be more precise and introduce the relevant correlation functions in the case of two species of fermions, where the spin degree of freedom σ is involved. The field operators are indicated by $\hat{\Psi}_\sigma(\boldsymbol{r})$,$\hat{\Psi}^\dagger_\sigma(\boldsymbol{r})$. The correlation functions at $T = 0$ are expectation values of products of field operators, in the ground state of the system (or in the state of interest). The one-body density matrix (OBDM) is defined as:

$$G^{(1)}_\sigma(\boldsymbol{r}_i, \boldsymbol{r}_j) = \langle \hat{\Psi}^\dagger_\sigma(\boldsymbol{r}_j)\hat{\Psi}_\sigma(\boldsymbol{r}_i)\rangle \ . \tag{1.1}$$

The diagonal part of the OBDM is the density. In the case of an homogeneous system with density n_σ for the σ particles, the OBDM depends only on the distance $r = |\boldsymbol{r}_i - \boldsymbol{r}_j|$. It is convenient to introduce the normalized version, which goes to 1 as $r \to 0$:

$$n_\sigma(r) = G^{(1)}_\sigma(0, \boldsymbol{r})/n_\sigma \ . \tag{1.2}$$

The off-diagonal part indicates the overlap between the original state and that obtained by moving a particle from position i to position j, at a distance r: it therefore measures the single particle coherence of the original state. In the case of bosons, the OBDM does not decrease to zero at infinity if there is a BEC, but flattens to a constant n_0/n, which is the condensate fraction. In the case of an ideal gas of fermions, for the $3D$ and $2D$ case the OBDM is, respectively:

$$n_\sigma(r) = \frac{3}{k_F r}[\sin(k_F r) - k_F r \cos(k_F r)] \ ; \tag{1.3}$$

$$n_\sigma(r) = \frac{2}{k_F r} J_1(k_F r) \ , \tag{1.4}$$

where J_1 is the Bessel function of first kind and order 1 and k_F is the Fermi wavevector, related to the total density as $n = k_F^2/2\pi$ in two dimensions and $n = k_F^3/3\pi^2$ in three dimensions. The Fourier transform of the OBDM is the momentum distribution n_k, which is a step function in the case of non interacting fermions.

The two-body density matrix (TBDM) is defined as:

$$G^{(2)}_{\sigma\sigma'}(\boldsymbol{r}_{\sigma 1}, \boldsymbol{r}_{\sigma' 2}; \boldsymbol{r}_{\sigma 3}, \boldsymbol{r}_{\sigma' 4}) = \langle \hat{\Psi}^\dagger_{\sigma'}(\boldsymbol{r}_4)\hat{\Psi}^\dagger_\sigma(\boldsymbol{r}_3)\hat{\Psi}_\sigma(\boldsymbol{r}_1)\hat{\Psi}_{\sigma'}(\boldsymbol{r}_2)\rangle \ . \tag{1.5}$$

Again, in case of homogeneous systems, one position dependence can be shifted to zero and it is convenient to normalize $G^{(2)}$ with the densities, $g^{(2)}_{\sigma\sigma'} = G^{(2)}_{\sigma\sigma'}/n_\sigma n_{\sigma'}$. Some specific sectors of this matrix are the most meaningful: the pair distribution functions, and the off-diagonal TBDM. The pair distribution functions indicate the probability of having a σ' particle at a distance r from a σ particle in position zero:

$$g^{(2)}_{\sigma\sigma'}(r) = \frac{G^{(2)}_{\sigma\sigma'}(0, \boldsymbol{r}_{\sigma'}; 0, \boldsymbol{r}_{\sigma'})}{n_\sigma n_{\sigma'}} \ . \tag{1.6}$$

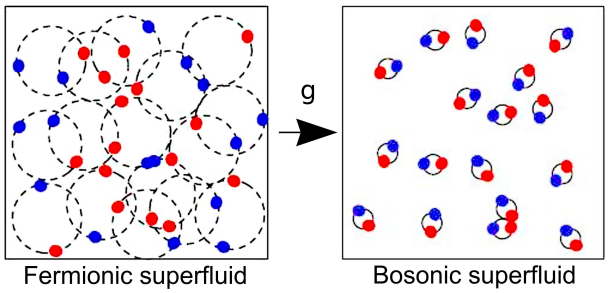

Figure 1.1: Pictorial view of the crossover from BCS pairing to a BEC of molecules. Red and blue particles indicate the two species of fermions.

Assuming a clustering property, which is valid in the mean-field regime and is exact in the case of non interacting fermions, one can expand the two-body parallel spin distribution functions in terms of the OBDM: $g^{(2)}_{\sigma\sigma}(r) = 1 - n_\sigma(r)^2$. The static structure factor $S_{\sigma\sigma'}(k)$, which is relevant in spectroscopy measurements, is related to the Fourier transform of the two-body distribution functions in the following way:

$$S_{\sigma\sigma'}(k) = 1 + \sqrt{n_\sigma n_{\sigma'}} \int d^d k [g^2_{\sigma\sigma'}(r) - 1] e^{i\boldsymbol{k}\boldsymbol{r}} \, . \tag{1.7}$$

The off-diagonal TBDM indicates the two-particle coherence of the original state:

$$g^{II}(r) = \frac{G^{(2)}_{\uparrow\downarrow}(0,0;\boldsymbol{r}_\uparrow,\boldsymbol{r}_\downarrow)}{n_\uparrow n_\downarrow} \, , \quad \boldsymbol{r}_\uparrow = \boldsymbol{r}_\downarrow \, ; \tag{1.8}$$

it is useful for fermions in a condensate regime, since in that case at large distance it flattens to $(n_0/n)^2$, where n_0/n can be considered as the condensate fraction.

1.3 BCS-BEC crossover

In this Thesis we consider various problems related to the BCS-BEC crossover. This quite general model has received increasing attention since its introduction by Leggett [Leg80] because of its applicability in the context of quantum gases, superfluid ^3He, high temperature superconductors and nuclear physics. The general idea is that a single theory should be able to describe a system of attractively interacting fermions of two species, from the weakly interacting limit, where many-body BCS correlations are dominant, to the strongly interacting limit, where the system becomes a BEC of dimers (Fig. 1.1). Actually Leggett showed that the BCS variational wavefunction

$$|\Psi_{BCS}\rangle = \prod_k (u_k + v_k \hat{a}^\dagger_{\uparrow k}, \hat{a}^\dagger_{\downarrow,-k})|0\rangle \tag{1.9}$$

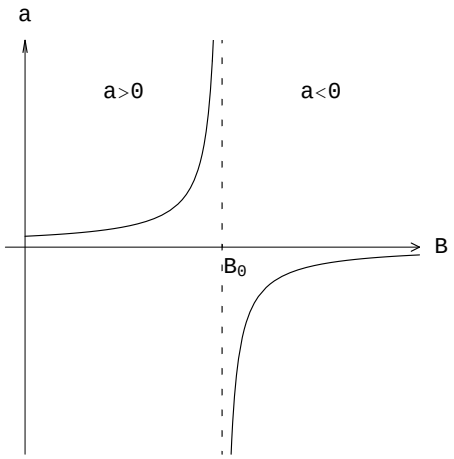

Figure 1.2: Dependence of the scattering length a on the external magnetic field B in three dimensions. Close to the resonance B_0 the behavior of a can be approximated by the formula $a = a_{bg}\left(1 - \frac{\Delta B}{B - B_0}\right)$, where a_{bg} is the background scattering length and ΔB and B_0 depend on the atomic species under consideration (see [TTHK99, GKG$^+$04, CGJT10]).

can be extended from weak coupling to strong coupling, qualitatively recovering the expected bosonic limit. Many theoretical efforts have been put in solving this problem with higher precision, among which in three dimensions Quantum Monte Carlo methods provided a valid benchmark [ABCG04].

In the field of ultracold gases it was possible to realize the BCS-BEC crossover in three dimensions thanks to the ability of tuning the effective interaction using Feshbach resonances [MVA95, CFH$^+$98, IAS$^+$98]. By applying an external magnetic field it is possible to tune the effective scattering length of the atoms (Fig. 1.2), from very small values to virtually infinite values (unitarity limit in three dimensions).

1.4 Properties of short range interacting systems

When a gas is dilute and with short range interactions, some analytical and universal properties can be derived. Recently a number of them was put in a general framework by Tan [Tan08a, Tan08b].

For such a system in three dimensions, the many-body wavefunction has the following asymptotic behavior [BP35, HY57]:

$$\Psi(r_1 \dots r_i \dots r_j \dots r_N) \xrightarrow[r_i \to r_j]{} \left(\frac{1}{|r_i - r_j|} - \frac{1}{a_{3D}}\right) \Phi\left[\frac{r_i + r_j}{2}, \{r_k\}, k \neq i, j\right], \quad (1.10)$$

valid for $|r_i - r_j| > R$, where R is the range of the potential and a_{3D} is the scattering length. In two dimensions an analogous expansion reads:

$$\Psi(r_1 \dots r_i \dots r_j \dots r_N) \xrightarrow[r_i \to r_j]{} \log\left(\frac{|r_i - r_j|}{a_{2D}}\right) \Phi\left[\frac{r_i + r_j}{2}, \{r_k\}, k \neq i, j\right] , \quad (1.11)$$

where a_{2D} is the $2D$ scattering length.

From these properties, which are also called cusp conditions, one can derive the asymptotic behavior of n_k in a system of fermions for large k (see also [WC10]):

$$n_{\uparrow k} \underset{k\to\infty}{\approx} n_{\downarrow k} \underset{k\to\infty}{\approx} \frac{C}{k^4} , \quad (1.12)$$

where again the limit $k \to \infty$ has to be considered as $k_F \ll k < 2\pi/R$ or equivalently $R < r \ll l$. The constant C is called the "contact" parameter. Analogously, for the pair distribution function $g^{(2)}_{\uparrow\downarrow}$ in three dimensions:

$$g^{(2)}_{\uparrow\downarrow}(r) \underset{r\to 0}{\approx} \frac{C}{k_F^4} \left(\frac{3\pi}{2k_F r}\right)^2 , \quad (1.13)$$

and in two dimensions:

$$g^{(2)}_{\uparrow\downarrow}(r) \underset{r\to 0}{\approx} \frac{C}{k_F^4} \left(2\log\left(\frac{r}{a_{2D}}\right)\right)^2 . \quad (1.14)$$

An interesting Tan's relation concerning the energy density $u = \frac{E}{N} n$ relates the contact parameter to the equation of state. In three dimensions

$$\frac{du}{d(-1/k_F a_{3D})} = \frac{\hbar^2 k_F}{4\pi m} C = \frac{3\pi}{2} n\varepsilon_F \frac{C}{k_F^4} , \quad (1.15)$$

where ε_F is the Fermi energy, while in two dimensions

$$\frac{du}{d\log(k_F a_{2D})} = \frac{\hbar^2}{2\pi m} C = 2n\varepsilon_F \frac{C}{k_F^4} . \quad (1.16)$$

In our Monte Carlo simulations, we use equations (1.13-1.16) as a check of the calculations, since, given the interaction parameter, the contact C extracted from the equation of state can be considered more precise than the same estimate of C obtained from the correlation functions.

Chapter 2

Monte Carlo method

The Monte Carlo method is a numerical stochastic approach to the calculation of multidimensional integrals or to the solution of differential equations of many variables (two problems which are equivalent in many relevant situations). The original idea was introduced in Nuclear Physics by Fermi and then studied by Metropolis and Ulam (see [MU49] for a general introduction).

The essence of the method is to interpret multidimensional integrals as expectation values of some functions (observables) of the multidimensional configurations, which are distributed according to a probability distribution function (*pdf*) that one is able to sample from. These expectation values are therefore estimated by sampling a relevant population of points in configuration space (walkers), which are distributed according to the given *pdf*, and taking the average of the observables calculated on the sampled walkers. An uncertainty in the estimated observables is intrinsic, given the numerical and stochastic nature of the calculation, but it can be systematically estimated and reduced with longer samplings or more efficient algorithms.

In the developing of the method the introduction of the Markov Chain Metropolis-Hastings acceptance/rejection technique was crucial [MRR$^+$53, Has70], because it allowed the sampling of arbitrarily complex *pdf*s. Again, it was first introduced in Physics and only after many years it arouse a significant interest in the field of Statistics [CG95].

In the context of Quantum Physics, major developments were the Variational Monte Carlo, introduced by McMillan [McM65], the Green's function Monte Carlo, introduced by Kalos [Kal62, Kal70] who also introduced importance sampling, and the Diffusion Monte Carlo, introduced by Anderson [And75] and refined by Reynolds, Ceperley and Alder [CA80, Rey82].

In this Chapter we will review some basic concepts about numerical integration (Sec. 2.1), we will introduce the Markov Chain Monte Carlo method (Sec. 2.2) and its application in the Variational Monte Carlo method (Sec. 2.3); we will then introduce the Diffusion Monte Carlo method both for

bosons (Sec. 2.4) and with importance sampling (Sec. 2.5) and for fermions (Sec. 2.6); we will finally introduce the wavefunctions that we used (Sec. 2.7), we will describe the calculation of correlation functions (Sec. 2.8) and we will discuss the issue of systematic errors (Sec. 2.9).

2.1 Integrals and Central limit theorem

In studying the properties of few- and many-body systems we are quite often driven to the calculation of multidimensional integrals, either needed for solving differential equations of motion, or involved in the evaluation of expectation values or averages in certain quantum or statistical distributions.

Such integrals can be calculated analytically in few relevant cases, but as soon as the number of degrees of freedom (DOF) is large most of the problems need some simplifications in order to be analytically solved, thus introducing some approximations, which are not always controllable. The positive feature of analytical results is the closed form of the solutions: if the problem depend on a set of parameters, a single analytical expression contains all the dependence on them.

When exact analytical results are not available and there is need for precise results, so that one wants to go beyond approximate analytical expressions, a possibility is to resort to numerical methods, which allow a more and more accurate answer the more the algorithms are iterated by the computer. The drawback of these methods is that the free parameters of the problem have to be specified from the beginning for each simulation so that the solution is known only in a discrete set of points in the parameter space, and one has to resort to fitting methods in order to give a more exhaustive answer.

The Monte Carlo methods are used to numerically calculate integrals by using stochastic techniques; they are very competitive with respect to other methods (see [KW08] and [PTVF92]) if the number of DOF is very large. Generally speaking, integration methods that calculate the values of the integrand function on a grid of points for each dimension of integration involve a number of operations which scales with a^N where a is the number of operations needed for each dimension and N is the number of DOF, while Monte Carlo methods scale as N^b, where b is some power depending on the algorithm; so for N larger than some critical dimension Monte Carlo methods are faster than any other integration method, given the same accuracy.

We will profit of the close relation between integration and the calculation of expectation values in statistics. A general multivariate *pdf* in the space $\mathbb{R}^N$ is a function $p(x) \geq 0$ such that $\int p(x)dx = 1$, where x is a point in the space $\mathbb{R}^N$. The expectation value of an observable is defined

as $\mathbb{E}[g(x)]|_p = \int g(x)p(x)dx$. Particular cases are the mean value of x: $\mu = \mathbb{E}[x]|_p = \int xp(x)dx$; and the variance of x, that is the second central moment: $\sigma^2 = \mathbb{E}[(x-\mu)^2]|_p = \int (x-\mu)^2 p(x)dx$.

Suppose that we want to numerically calculate the integral of a function depending on one variable:

$$I = \int_a^b f(x)dx \ . \tag{2.1}$$

Applying the Riemann definition of integrals we could simply partition the support $[a, b]$ into m segments $[x_i, x_{i+1})$ and construct the sum

$$\tilde{I} = \sum_{i=1}^{m} f(x_i)(x_{i+1} - x_i) \ ;$$

if the partition is refined then the sum $\tilde{I}$ converges to I. For definiteness let us consider regular partitions such that

$$\tilde{I} = \frac{b-a}{m} \sum_{i=1}^{m} f(x_i) \ ;$$

in such way one obtains an estimate of I with an error that scales as $1/m^2$; extended summation rules can improve the scaling to $1/m^4$ (see [PTVF92]). The number of function evaluations is m so that the time for obtaining a definite estimate of the error scales as a power of m. When considering multidimensional integrals, however, this power depends on the dimensionality, so that the scaling is exponential on the number of DOF.

One can approach the issue of integration from another perspective, by considering the integral (2.1) as the expectation value of the function $f(x)$, with x being a random variable with uniform $pdf(x) = u(x) = 1/(b-a)$, so that

$$I = \mathcal{N}\mathbb{E}[f(x)]|_u \ , \tag{2.2}$$

where $\mathcal{N} = (b-a)$ is the normalization. It is possible to estimate this mean value by sampling a large number of points from the uniform *pdf* and summing over the values of $f(x)$ in these points:

$$\mathbb{E}[f(x)]|_u \approx \bar{f} = \frac{1}{m} \sum_{i}^{m} f(x_i)$$

The error on the estimate of the integral I can be evaluated by using the central limit theorem. Actually the arithmetic average of m independent and equally distributed random variables $X = \frac{x_1+x_2+\cdots+x_m}{m}$ is a random variable whose distribution, in the large m limit, is a normal distribution with mean μ_X equal to the mean μ_x of the original random variables, and

variance σ_X^2 equal to their variance divided by m, $\sigma_X^2 = \sigma_x^2/m$. This is valid whatever the distribution of the original random variables is, under certain regularity conditions which are not going to be discussed here (see [KW08] for details). A good estimate for the variance of the variable f is

$$\sigma_f^2 \approx s_f^2 = \frac{1}{m-1}\sum_i^m (f(x_i) - \bar{f})^2 \ ,$$

so that the error on our approximation of the integral $I \approx \mathcal{N}\bar{f}$ can be obtained as

$$(\Delta I)^2 \approx \mathcal{N}^2 \frac{1}{m}\frac{1}{m-1}\sum_i^m (f(x_i) - \bar{f})^2 \ .$$

One can reduce the variance of the result by using importance sampling. This method is useful if one knows how to sample from a *pdf* $(x) = g(x)$ which has a shape similar to the integrand function $f(x)$ so that their ratio is smoother than the function f itself. One then rewrites the integral as:

$$I = \int_a^b \frac{f(x)}{g(x)} g(x)dx = \mathcal{N}\mathbb{E}\left[\frac{f(x)}{g(x)}\right]|_g \ ,$$

where the average is taken with the known distribution g. When approximating the integral with the sum $I \approx \mathcal{N}\frac{1}{m}\sum_i^m f(x_i)/g(x_i)$, with points x_i sampled from $g(x)$, the variance of the estimated sum is smaller than in the previous case, since $f(x_i)/g(x_i)$ has fluctuations smaller than those of $f(x_i)$.

For some simple *pdf*s a direct sampling method is known. The uniform distribution can be sampled by internal standard routines provided by any compiler (in fact the sequence of numbers provided by these routines can be considered pseudo-random numbers, in a sense discussed for example in [PTVF92]). A probability distribution which will be useful in the following is the Gaussian one, defined by:

$$g(x) = \frac{1}{\sqrt{2\pi}\sigma} e^{-\frac{(x-\mu)^2}{2\sigma^2}} \ , \text{with } x \in (-\infty, \infty) \ , \tag{2.3}$$

where μ is the mean and σ is the standard deviation; it can be sampled for example by the Box-Muller algorithm [BM58]:

- Sample u_1 and u_2 independently from the uniform distribution on the interval $[0, 1]$;
- calculate $x_1 = \sqrt{-2\log u_1}\cos(2\pi u_2)$ and $x_2 = \sqrt{-2\log u_1}\sin(2\pi u_2)$;
- x_1 and x_2 are two independent Gaussian random variables, with $\mu = 0$ and $\sigma = 1$;
- for generic mean and variance one takes $x_i \to \sigma x_i + \mu$.

2.2 Monte Carlo sampling with Markov Chains

When the probability distribution to be sampled is complicated and possibly multivariate, a general Monte Carlo sampling method, relying on Markov chains, can be used. Let us therefore introduce some basic concepts about Markov chains (see [HPS72]).

Let us consider a sequence $\{X_n\}$ of random variables, each of which is distributed according to $pdf(X_n) = \pi_n(X_n)$. For simplicity let X_n belong to some finite set, even if we will consider also the continuum case in the following. Let us introduce a rule for getting $\pi_n(X_n)$, once the past "history" $\{X_0, X_1 \cdots X_{n-1}\}$ is given: this is called the conditional probability of X_n. The sequence $\{X_n\}$ is called a Markov chain if the conditional probability of X_n, for $\forall n$, is conditioned only by the previous element in the sequence, X_{n-1}:

$$P(X_n = j | X_{n-1} = i, X_{n-2} = k, X_{n-3} = l, \cdots) = P(X_n = j | X_{n-1} = i) \equiv P(i \to j) \ , \quad (2.4)$$

where the notation $i \to j$ is a simple guide to the eye that means that i is the starting point and j is the final point. In general the conditional probability could also depend on the iteration index n, but here we only consider time homogeneous Markov chains.

By definition of probability,

$$P(i \to j) \geq 0 \ ; \quad (2.5)$$

$$\sum_j P(i \to j) = 1 \ , \forall i \ . \quad (2.6)$$

Then the evolution of the probability distribution can be described by the equation:

$$\pi_n(X_n = j) = \sum_i \pi_{n-1}(X_{n-1} = i) P(i \to j) \ , \quad (2.7)$$

and the conditional probability $P(i \to j)$ can be interpreted as a transition operator, or matrix.

An important concept, which will be useful for the purpose of using Markov chains to sample from generic distributions, is the stationary distribution of a Markov chain, defined by the relation:

$$\pi(j) = \sum_i \pi(i) P(i \to j) \ ; \quad (2.8)$$

this means that the distribution $\pi(i)$ is invariant under the action of the transition matrix. The existence of such a stationary distribution is guaranteed if each state j can be reached by any other state i in a finite number of steps (irreducibility); moreover each state i must be positive recurrent, meaning

that the average number of steps T_i for the state to appear again in the Markov chain must be finite. If moreover there is no characteristic period of recurrence, the chain is called aperiodic, and the stationary distribution π is also an equilibrium distribution, in the sense that for any initial distribution $\pi_0(X_0)$, the recursive action of the transition matrix asymptotically drives the chain to π:

$$\lim_{n\to\infty} P(X_0 = i, X_n = j) = \pi(X_n = j) \; . \tag{2.9}$$

The previous conditions for the existence of an equilibrium distribution are necessary and sufficient and are equivalent to saying that the Markov chain is ergodic.

If a Markov chain is reversible, detailed balance holds, which is expressed by the following condition:

$$\pi(j)P(j \to i) = \pi(i)P(i \to j) \; ; \tag{2.10}$$

this is a sufficient condition for π to be the equilibrium distribution, provided P is irreducible. Actually one can simply sum the above equation over i to obtain Eq. (2.9).

We can now introduce the Metropolis-Hastings algorithm [MRR$^+$53, Has70] for sampling a given probability distribution $\pi(x)$ (where x can be a vector, that is π can be multivariate). This algorithm exploits the properties of reversible Markov chains in order to asymptotically sample random variables from their equilibrium distribution. The initial distribution π_0 can be arbitrary, for example uniform on the space which is considered, and is represented by a collection of points belonging to that space, which are usually called walkers. Each walker, for example at position x, evolves independently thanks so the action of the transition matrix $P(x, y)$, which consists in the sampling of another point y in space from the distribution $pdf(y) = P(x, y)$; y will be the new position of the walker. If the transition matrix $P(x, y)$ simply adds a random variable to x in order to obtain y then the chain is called a random walk. One reaches the equilibrium distribution after a transient, by iterating the application of the transition matrix $P(x, y)$ over the entire population. After the transient, averages can be taken using all the walkers at subsequent times.

The transition matrix in the Metropolis-Hastings algorithm is produced in the following way:

$$\begin{aligned} P(x \to y) &= T(x \to y)A(x \to y) \; , \quad x \neq y \; , \\ P(x \to x) &= 1 - \sum_{j \neq i} T(x \to y)A(x \to y) \; , \end{aligned} \tag{2.11}$$

where $T(x \to y)$ is an arbitrary conditional probability distribution from which we are able to directly sample a proposed y, given the previous point

x and $A(x \to y)$ is the acceptance probability of the move proposed by T. The acceptance probability is constructed in such a way that, even if T is arbitrary, P fulfills detailed balance and drives the Markov chain to the equilibrium distribution. A suitable choice is

$$A(x \to y) = \min\left(1, \frac{\pi(y)T(y \to x)}{\pi(x)T(x \to y)}\right). \tag{2.12}$$

If T is symmetric under the exchange of x and y (for example it is a Gaussian distribution of $(x-y)$), then the acceptance probability is simpler, because it reduces to $A(x \to y) = \min\left(1, \frac{\pi(y)}{\pi(x)}\right)$.

When calculating the expected value of a function, or observable, $f(x)$ in the $pdf(x) = \pi(x)$, one follows the following algorithm:

- Start from a population of m walkers randomly distributed in space.
- Start iteration $iter$: for each walker $ipop$ at position x do:
  - Sample a point y' from the distribution $T(x \to y')$.
  - Calculate $\frac{\pi(y')T(y' \to x)}{\pi(x)T(x \to y')}$.
  - If it is higher than 1 then accept the move: $y = y'$, else reject the move: $y = x$.
  - Calculate $f_{ipop} = f(y)$.
- If the transient is finished, calculate the partial sum $\bar{f}_{iter} = \frac{1}{m}\sum_{ipop} f_{ipop}$.
- Go to next iteration
- The estimated $\mathbb{E}[f]|_\pi$ is $\bar{f} = \frac{1}{n}\sum_{iter>transient} \bar{f}_{iter}$, where n is the number of iterations after the transient.

In general the sampling probability T can be arbitrary but in practice the choice of T determines the length of the transient after which the sampled distribution is π. Moreover, if for example T is a Gaussian distribution of the variable $(x-y)$, then a small variance of it will cause high acceptance ratio, but high correlation between the moves, while a big variance will cause a small correlation of the moves, but a small acceptance ratio. A good compromise is obtained with an acceptance ratio around $40\% \div 60\%$. The issue of the correlation between the moves reflects itself in a high correlation between subsequent values $\bar{f}_{iter}$, so that the central limit theorem cannot immediately used to estimate the variance of $\bar{f}$. One then divides the calculation in nb blocks such that iterations from different blocks are not correlated anymore; this is true if the length lb of a single block is longer than the correlation time of the estimated quantity f. Therefore one can sum the contributions to $\bar{f}$ coming from the iterations within a block

$\bar{f}_{ib} = \frac{1}{lb}\sum_{iter\in ib} \bar{f}_{iter}$, and use their variance to estimate the variance of $\bar{f} = \frac{1}{nb}\sum_{ib} \bar{f}_{ib}$:

$$\sigma_{\bar{f}}^2 \approx s_{\bar{f}}^2 = \frac{1}{nb}\left(\frac{1}{nb-1}\sum_{ib}(\bar{f}_{ib} - \bar{f})^2\right) \tag{2.13}$$

Obviously a longer correlation time forces to use longer blocks and this causes having less independent contributions for calculating the observable, thus increasing the variance.

See Appendix A for details about the estimate of the correlation time needed for this accurate estimate of the error.

2.3 Variational Monte Carlo

When studying such quantum many-body systems as those introduced in Chapter 1, Quantum Monte Carlo methods prove very useful, since they allow the calculation of the expectation values of observables which require integration over many variables, for example the energy or the correlation functions. Usually these quantities need to be calculated in the ground state or at thermal equilibrium. There have been many attempts of studying also dynamical properties with Quantum Monte Carlo (for example [BC96]), but they are not going to be discussed in this Thesis.

Let us now introduce the Variational Monte Carlo method (VMC); see [McM65, CCK77] for studies of many bosons and fermions with VMC and [Cep03] for a historical-pedagogical review.

The system under study is composed of N particles with same mass m in dimension d, whose dynamics is governed by the Hamiltonian operator $\hat{H}$, which is the sum of kinetic energy and potential energy:

$$\hat{H} = \hat{K} + \hat{V} = -D\sum_i \Delta_i + \sum_{i<j} \hat{V}(i,j) \tag{2.14}$$

where $D = \frac{\hbar^2}{2m}$, whereas in coordinate representation $\Delta_i = \sum_\alpha^d \partial_{\alpha_i}^2$ is the Laplacian for each particle and for simplicity we consider a system with translational invariance, without an external potential. In this model the many-body interacting potential is the sum of two-body potentials $\hat{V}(i,j)$.

A possible way of approximately solving this many-body problem at zero temperature, in the sense of finding the ground state, is to restrict the Hilbert space of the wavefunctions to some subset which can be parametrized in terms of (hopefully few) variational parameters a. Then one looks for the minimum of the expectation energy by varying the parameters:

$$E_V = \min_a \left.\frac{\langle\psi \mid \hat{H} \mid \psi\rangle}{\langle\psi \mid \psi\rangle}\right|_a , \tag{2.15}$$

so that $E_V \geq E_0$ is an upper bound for the ground state energy and the corresponding ψ_{a_m} can be considered an approximation of the ground state. The larger the space of parameters, the more accurate will be the upper bound on energy and the ground state wavefunction. Evidently one has to restrict the functional form of the wavefunctions so that this variational search is computationally feasible: in the literature many different variational wavefunctions have been proposed which proved accurate for specific problems and which are the basis for more refined methods.

A necessary step for applying Monte Carlo methods to many-body systems is to write the expectation values of the observables as mean values of some functions weighted with a *pdf*, so that the techniques introduced in Sec. 2.2 can be used. Eq. (2.15) can be rewritten, in first quantized form, in the following way:

$$E_V = \min_a \frac{\int \psi_a(\boldsymbol{R}) \langle \boldsymbol{R} \mid \hat{H} \mid \psi \rangle_a d\boldsymbol{R}}{\int \psi_a(\boldsymbol{R})^2 d\boldsymbol{R}} = \min_a \int \frac{\psi_a(\boldsymbol{R})^2}{\int \psi_a(\boldsymbol{R'})^2 d\boldsymbol{R'}} E_L^a(\boldsymbol{R}) d\boldsymbol{R} \,, \tag{2.16}$$

where $\boldsymbol{R}$ is a collective variable representing a point in the configuration space, $E_L^a(\boldsymbol{R}) = \langle \boldsymbol{R} \mid \hat{H} \mid \psi \rangle_a / \psi_a(\boldsymbol{R})$ is called the local energy and for simplicity we have considered only real-valued wavefunctions (which is not a limitation when considering the ground state of time-invariant hamiltonians). Now the energy expectation value appearing in the previous equation is in the form $\mathbb{E}[E_L^a(\boldsymbol{R})]|_{p^a}$, where the probability distribution function to be sampled is $p^a(\boldsymbol{R}) = \frac{\psi_a(\boldsymbol{R})^2}{\int \psi_a(\boldsymbol{R})^2 d\boldsymbol{R}}$. Notice that this probability distribution is well defined (in the sense that it is positive and normalized) even if the variational wavefunction is negative for some regions in configuration space, due to the appearance of the square of the wavefunction. This is the case for example of Fermi systems, which can be treated as well as Bose systems with VMC.

Let us now specify how the Markov Chain Monte Carlo method is implemented in VMC. The probability distribution to be sampled is essentially the square of the variational wavefunction. A transition matrix which converges to that probability distribution can be deduced accordingly to Eq. (2.11), with the obvious extension to the continuum case. The transition matrix of the proposed moves can be a Gaussian in configuration space, that is

$$T(\boldsymbol{R} \to \boldsymbol{R'}) = \frac{1}{(2\pi\alpha)^{dN/2}} \exp\left[-\frac{\mid \boldsymbol{R} - \boldsymbol{R'} \mid^2}{2\alpha} \right], \tag{2.17}$$

where α is the variance. The acceptance probability has the form (2.12), but, due to the symmetry of the transition matrix, it reduces to

$$A(\boldsymbol{R} \to \boldsymbol{R'}) = \min\left(1, \frac{\psi_a(\boldsymbol{R'})^2}{\psi_a(\boldsymbol{R})^2}\right). \tag{2.18}$$

This algorithm requires the calculation of the square of the wavefunction at each iteration, in order to perform the acceptance-rejection step. It is useful to count the ratio of the accepted moves with respect to all the proposed moves, which should be kept around 50% by tuning the parameter α. It is worth emphasizing, however, that the correct sampling is obtained for any α, its value influencing only the efficiency of the algorithm.

The optimization of the parameters is performed with standard methods [PTVF92]. In case of one single parameter we have used a simple grid method, and a more refined version of the steepest descent method (introduced by Sorella [Sor05]) in case of two parameters. The optimization of more parameters at a time was beyond our capabilities, so that we simply scanned a grid of points in the space of parameters.

There is a second way of estimating the energy, by using the force estimator, which provides also a check for the stationarity of the distribution to be sampled. This second estimator can be introduced by integrating by parts the expectation value of the kinetic energy:

$$\begin{aligned}
&\int \psi(\boldsymbol{R}) \left(-D \sum_i \Delta_i + \hat{V} \right) \psi(\boldsymbol{R}) d\boldsymbol{R} = \\
&- D \int_{\partial\Omega} \psi(\boldsymbol{R}) \sum_i \nabla_i \psi(\boldsymbol{R}) d\boldsymbol{R} + \int \left(D \sum_i (\nabla_i \psi(\boldsymbol{R}))^2 + V(\boldsymbol{R}) \psi(\boldsymbol{R})^2 \right) d\boldsymbol{R} = \\
&\int \psi(\boldsymbol{R})^2 \left(D \sum_i \left(\frac{\nabla_i \psi(\boldsymbol{R})}{\psi(\boldsymbol{R})} \right)^2 + V(\boldsymbol{R}) \right) d\boldsymbol{R} = \int \psi(\boldsymbol{R})^2 E_F(\boldsymbol{R}) d\boldsymbol{R} \, ,
\end{aligned} \tag{2.19}$$

where the surface term $\int_{\partial\Omega} \cdots$ vanishes due to the decay of the wavefunction and its derivatives at large interparticle distances (see also Sec.2.9 concerning the boundary conditions). The force estimator of the energy contains two contributions, the force term and the potential term: $E_F(\boldsymbol{R}) = \frac{D}{4} \sum_i \boldsymbol{F}_i(\boldsymbol{R})^2 + V(\boldsymbol{R})$, where the so called quantum forces are defined as

$$F_i^\alpha(\boldsymbol{R}) = 2 \frac{\partial_{\alpha_i} \psi(\boldsymbol{R})}{\psi(\boldsymbol{R})} = \partial_{\alpha_i} \log |\psi(\boldsymbol{R})|^2 \, . \tag{2.20}$$

In general the force estimator of energy has a higher variance than the estimator which involves the local energy. It is useful to accumulate both the estimators in order to check the correctness of the implementation of the VMC algorithm.

The calculation of other observables, such as the correlation functions, will be discussed in Sec. 2.8.

2.3.1 Smart Monte Carlo

An improved transition matrix of the proposed moves can be introduced by considering the analogy between VMC and Monte Carlo sampling in classical statistical mechanics. In VMC the distribution to be sampled, neglecting the normalization, is $p = |\psi|^2$, while in statistical mechanics the distribution is the Boltzmann weight $p = e^{-\beta\mathcal{F}}$, where β is the inverse temperature and $\mathcal{F}$ is the free energy. The equilibrium macro-state in statistical mechanics is the one that minimizes $\mathcal{F}$, and the Metropolis algorithm with probability distribution $e^{-\beta\mathcal{F}}$ indeed favors configurations with small $\mathcal{F}$. Provided detailed balance is respected, one can accelerate the reaching of the minimum by adding a force term to the moves of the walkers, proportional to the negative gradient of the free energy, that is proportional to $\nabla(\log p)$. In VMC this force term exactly corresponds to the "quantum force" introduced in Eq. (2.20), this correspondence explaining the name. The details of this derivation can be found in [RDF78, PRB78, CCK77, CKL81].

By following the analogy, one introduces the transition matrix of the proposed moves in the form of a drifted Gaussian distribution, the drift given by the quantum force calculated in the initial point $\boldsymbol{R}$:

$$T(\boldsymbol{R} \to \boldsymbol{R'}) = \frac{1}{(4\pi Dt)^{dN/2}} \exp\left[-\frac{|\ \boldsymbol{R} + tD\boldsymbol{F}(\boldsymbol{R}) - \boldsymbol{R'}\ |^2}{4Dt}\right], \qquad (2.21)$$

where, for later convenience, the constant $D = \frac{\hbar^2}{2m}$ has been introduced so that the arbitrary parameter t has the dimension of inverse energy. The acceptance probability has the form (2.12), where the transition matrices T do not simplify, since they are no longer symmetric for exchange of the initial and the final position. With respect to standard VMC the acceptance is increased, so that a larger mean displacement can be used and one would expect faster convergence, but one has also to consider the computational cost of evaluating the forces for all the proposed moves, so that the preference between VMC and Smart Monte Carlo depends on the specific problem (see [CCK77]).

2.4 Diffusion Monte Carlo

Variational Monte Carlo is a very efficient and fast algorithm. It proves very useful when an accurate many-body wavefunction is known. It can be also used to produce starting configurations for more refined methods, such as Diffusion Monte Carlo (DMC). This method solves the many-body Schroedinger equation in imaginary time. Actually the imaginary time evolution projects the initial wavefunction to the ground state wavefunction times an exponentially decaying factor, provided the initial wavefunction has non-zero overlap with the ground state wavefunction, as we will show in

the following discussion. The DMC algorithm was introduced by Anderson [And76, And75] and refined by Reynolds, Ceperley and Alder [Rey82]. For general introductions see [Gua98, HLR94, Kos96, FMNR01, Bor02].

For problems in which the many-body ground state wavefunction is positive definite (for example, a system of bosons with time-reversal symmetry), DMC is able to find the ground state energy exactly. This means that, given an uncertainty ϵ, it is possible to choose a sufficiently large number of iterations M such that the energy estimated by DMC algorithm E_M and the energy of the ground state E_0 respect the inequality $|E_0 - E_M| < 2\epsilon$ with a probability of 95%.

The differential equation to solve, with the proper boundary condition, has the form

$$-\frac{\partial}{\partial\tau}\Psi(\boldsymbol{R},\tau) = (\hat{H}(\boldsymbol{R}) - E_{ref})\Psi(\boldsymbol{R},\tau)\ ; \qquad \Psi(\boldsymbol{R},\tau=0) = \Psi_i(\boldsymbol{R})\ ; \tag{2.22}$$

where $\tau = \imath t/\hbar$ is the imaginary time in units of inverse energy and E_{ref} is a reference energy which does not affect the eigenstates of the hamiltonian apart from tuning their exponential time dependence. Actually, given the eigenstates $\varphi_n(\boldsymbol{R})$, which obey the equation $\hat{H}(\boldsymbol{R})\varphi_n(\boldsymbol{R}) = E_n\varphi_n(\boldsymbol{R})$, the initial state can be decomposed as $\Psi_i(\boldsymbol{R}) = \sum_n c_n\varphi_n(\boldsymbol{R})$, so that the solution of (2.22) is

$$\Psi(\boldsymbol{R},\tau) = \sum_n c_n e^{-\tau(E_n - E_{ref})}\varphi_n(\boldsymbol{R}) \xrightarrow[\tau\to\infty]{} c_0 e^{-\tau(E_0-E_{ref})}\varphi_0(\boldsymbol{R})\ . \tag{2.23}$$

So the imaginary time evolution consists of an exponential decay of each component of the initial wavefunction (provided $E_{ref} < E_n$, $\forall n$), with the interesting property that the longest-living component is the lowest energy one, which is the ground state if the initial wavefunction has non-zero overlap c_0 with the ground state. One can estimate the transient time after which only the ground state gives a significant contribution as $\tau_t \approx \frac{1}{E_1-E_0}$, that is the inverse of the energy gap (which we assume to be different from zero).

The Monte Carlo method can be used in this case by rewriting the Schroedinger equation in the following integral form

$$c_0 e^{-\tau(E_0-E_{ref})}\varphi_0(\boldsymbol{R'}) = \int \Psi_i(\boldsymbol{R})G_0(\boldsymbol{R}\to\boldsymbol{R'},\tau)d\boldsymbol{R}\ , \quad (\tau \gg \frac{1}{E_1-E_0})\ , \tag{2.24}$$

and interpreting the wavefunction as a probability density which evolves in time according to the Green's function of the original differential equation, which is defined as

$$G_0(\boldsymbol{R}\to\boldsymbol{R'},\tau) = \langle\boldsymbol{R'}|\hat{G}_0|\boldsymbol{R}\rangle = \langle\boldsymbol{R'}|e^{-\tau(\hat{H}-E_{ref})}|\boldsymbol{R}\rangle\ , \tag{2.25}$$

where $\hat{G}_0$ is the time evolution operator (or projector).

The ground state wavefunction and the Green's function have to be positive definite for them to be interpreted as a probability density and a probability transition matrix. The reason is that now we would like to sample from $p(\boldsymbol{R}) = \varphi_0(\boldsymbol{R})$ and not from $p(\boldsymbol{R}) = |\Psi_T(\boldsymbol{R})|^2$ as in the VMC method. Therefore special methods have to be used in order to treat fermions and will be discussed in Sec. 2.6.

Even if Eq. (2.24) has some resemblance with the equation of a Markov chain (2.7), there are two important differences: the probability distribution function is not normalized the same way at different times, due to the exponential decaying factors, and also the transition matrix is not normalized in the sense of Eq. (2.5). This will be evident when performing a small-time expansion. Moreover a major difference with VMC is that in this case the evolution operator is in principle known (even if not for large time), while the distribution to be sampled is not known. In VMC the situation is the opposite, so that one introduces the detailed balance condition in order to create a useful transition matrix. In spite of these considerations many authors introduce a Metropolis accept-reject step even in DMC, in particular when importance sampling is used, see appendix B for a discussion.

It is possible to simulate Eq. (2.22) by means of stochastic processes; actually it is identical to a classical diffusion equation for a density distribution, with a typical linear dependence on the time derivative and on the Laplacian, with diffusive constant $D = \frac{\hbar^2}{2m}$ and a further source term $(V - E_{ref})\Psi$ which can be interpreted as a birth-death term for classical particles. Therefore, in the spirit of Monte Carlo sampling of integrals, one sets up a population of points in configuration space (walkers) and then moves them accordingly to the Green's function of the problem, that is performing a series of diffusion and birth-death processes. After the transient time τ_t the population of walkers will represent the stationary distribution corresponding to φ_0. The exponential dependence on time, in this perspective, corresponds to an exponential decay in the number of walkers, so that suitable renormalizations of the population have to be introduced in order to stabilize the algorithm, for example by periodically setting E_{ref} equal to the average energy of the previous block.

The energy can then be estimated by the mixed estimator

$$E_M = \frac{\langle\varphi_0|\hat{H}|\psi_T\rangle}{\langle\varphi_0|\psi_T\rangle} = \frac{\int \varphi_0(\boldsymbol{R})E_L^T(\boldsymbol{R})\psi_T(\boldsymbol{R})d\boldsymbol{R}}{\int \varphi_0(\boldsymbol{R})\psi_T(\boldsymbol{R})d\boldsymbol{R}} \approx \frac{\sum_i^M \psi_T(\boldsymbol{R_i})E_L^T(\boldsymbol{R_i})}{\sum_i^M \psi_T(\boldsymbol{R_i})}\,, \tag{2.26}$$

where ψ_T is an arbitrary known trial wavefunction (in principle it could even be $\psi_T = 1$ so that $E_L^T(\boldsymbol{R}) = V(\boldsymbol{R})$). The variance of the estimator is reduced if ψ_T is a good approximation of the ground state. Note that the sums in the last passage of Eq. (2.26) run over the whole population of walkers at all times next to the transient τ_t.

In general, an explicit expression for the Green's function (2.25) is not

known analytically, due to the presence of both a kinetic energy term and an interaction term in the Hamiltonian, which do not commute. When a short imaginary time $d\tau$ is involved, however, one can perform a perturbative expansion in terms of the small time step, so it is useful to split the evolution operator in the following way:

$$\hat{G}_0(\tau) = \lim_{n\to\infty} \left[\hat{G}_0\left(\frac{\tau}{n}\right)\right]^n . \tag{2.27}$$

One then approximates $\hat{G}_0(\tau)$ with the product on the rhs of the previous equation, keeping a fixed large n, that is considering a small time step $d\tau = \tau/n$. Each factor in the product can be expanded in the following way:

$$\hat{G}_0(d\tau) = e^{-d\tau\hat{K}} e^{-d\tau(\hat{V}-E_{ref})} + \mathcal{O}[d\tau^2] , \tag{2.28}$$

which is the Trotter formula (see [HS05]). The above approximation introduces a systematic error in the Green's function which is quadratic in the time step, so that suitable extrapolations to $d\tau \to 0$ have to be produced in order to avoid a bias in the results of the simulation.

Eq. (2.28) is very useful since the Green's functions of a pure kinetic term and a pure interaction term explicitly appear, which are analytically known in many cases. The Green's function of the kinetic part obeys the following equation

$$\begin{aligned} -\frac{\partial}{\partial\tau} G_K(\boldsymbol{R} \to \boldsymbol{R'}, \tau) &= \hat{K} G_K(\boldsymbol{R} \to \boldsymbol{R'}, \tau) ; \\ G_K(\boldsymbol{R} \to \boldsymbol{R'}, 0) &= \delta(\boldsymbol{R} - \boldsymbol{R'}) , \end{aligned} \tag{2.29}$$

and, in systems with translational invariance, it has the expression

$$G_K(\boldsymbol{R} \to \boldsymbol{R'}, d\tau) = \langle \boldsymbol{R'}|e^{-d\tau\hat{K}}|\boldsymbol{R}\rangle = \frac{1}{(4\pi D d\tau)^{dN/2}} \exp\left[-\frac{|\ \boldsymbol{R} - \boldsymbol{R'}\ |^2}{4D d\tau}\right] , \tag{2.30}$$

which, in terms of the final position $\boldsymbol{R'}$, is a Gaussian distribution centered in the initial position $\boldsymbol{R}$ and with variance $\sigma^2 = 2Dd\tau = \frac{\hbar^2 d\tau}{m}$. The interaction potential term obeys the equation

$$\begin{aligned} -\frac{\partial}{\partial\tau} G_V(\boldsymbol{R} \to \boldsymbol{R'}, \tau) &= (\hat{V} - E_{ref}) G_V(\boldsymbol{R} \to \boldsymbol{R'}, \tau) ; \\ G_V(\boldsymbol{R} \to \boldsymbol{R'}, 0) &= \delta(\boldsymbol{R} - \boldsymbol{R'}) ; \end{aligned} \tag{2.31}$$

for the simple but relevant case of an interaction potential diagonal in the space of configurations the previous equation is a rate equation, whose solution is

$$\begin{aligned} G_V(\boldsymbol{R} \to \boldsymbol{R'}, d\tau) &= \langle \boldsymbol{R'}|e^{-d\tau(\hat{V}-E_{ref})}|\boldsymbol{R}\rangle = \\ &\exp\left[-d\tau(V(\boldsymbol{R}) - E_{ref})\right]\delta(\boldsymbol{R} - \boldsymbol{R'}) = G_V(\boldsymbol{R}, d\tau)\delta(\boldsymbol{R} - \boldsymbol{R'}) . \end{aligned} \tag{2.32}$$

Therefore the approximate Green's function reduces to

$$G_0(\boldsymbol{R} \to \boldsymbol{R'}, d\tau) \xrightarrow[d\tau \to 0]{} G_K(\boldsymbol{R} \to \boldsymbol{R'}, d\tau) G_V(\boldsymbol{R}, d\tau) \; . \tag{2.33}$$

It can be shown that a Green's function with an error of order $d\tau^2$ will produce an estimated energy with a linear time-step dependence (heuristically, it is so because $E = -\partial G_0 / \partial \tau|_{\tau=0}$, see [Gua98]).

The Green's function is not normalized with respect to $\boldsymbol{R'}$ because G_V is not. Indeed this is the factor which produces the change in the normalization of the wavefunction. In the classical analogy introduced above, which allows a stochastic process solution of the equation, the term G_K is used as a conditional transition probability (similar to that introduced in VMC): given a walker at position $\boldsymbol{R}$, one draws a random number ξ from the Gaussian distribution (2.30) and moves the walker to

$$\boldsymbol{R} \to \boldsymbol{R'} = \boldsymbol{R} + \xi \; . \tag{2.34}$$

The term G_V, as told before, can be interpreted as a branching factor, that is a probability for the creation or destruction of copies of the walker at point $\boldsymbol{R}$ (or $\boldsymbol{R'}$, at this order in $d\tau$ there is no difference). Operatively the number of created walkers is taken to be

$$n_{copy} = \mathrm{Int}[G_V(\boldsymbol{R}, d\tau) + \xi'] \; , \tag{2.35}$$

where $\mathrm{Int}[x]$ gives the biggest integer number smaller than x and ξ' is a random number uniformly distributed in the interval $[0, 1]$. Another possibility for the interpretation of G_V is to use it as a weight when accumulating the observables, without changing the number of walkers. For example the mixed estimator of energy (2.26) would become

$$E_M \approx \frac{\sum_i^M \psi_T(\boldsymbol{R_i}) G_V(\boldsymbol{R_i}, d\tau) E_L^T(\boldsymbol{R_i})}{\sum_i^M \psi_T(\boldsymbol{R_i}) G_V(\boldsymbol{R_i}, d\tau)} \; . \tag{2.36}$$

It is clear that both the interpretations of G_V should produce the same result, it has however been noticed that the branching technique gives a lower variance for the observables than the weighting technique; moreover the weighting technique tends to favor the dominance of a single walker (see [ACK00] for details). Figure 2.1 pictorially represents the diffusion-branching process.

2.5 Importance sampling

When some analytical information is known about the exact or mean-field solution, it is very useful to introduce importance sampling in the DMC algorithm (see Sec. 2.1 and [KLV74, CCK77]). Suppose that the best known

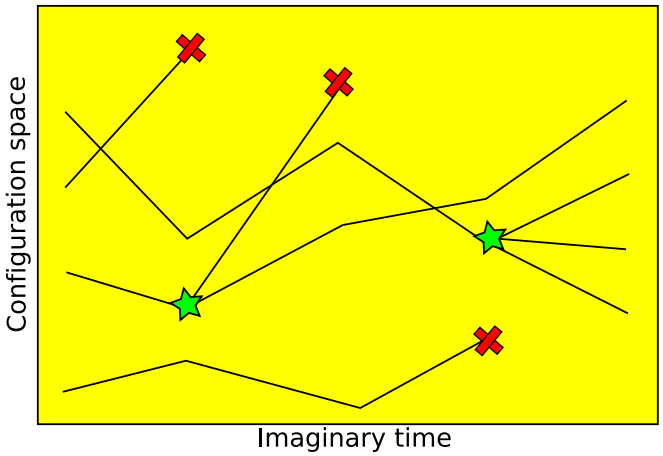

Figure 2.1: Pictorial view of the diffusion-branching process. The lines represent the diffusion process governed by G_K, the red crosses the death of a walker, the green stars the birth of new walkers, governed by G_V. The total number of walkers can change in time. For large enough time the walkers are distributed as φ_0.

approximation to the ground state wavefunction is the trial wavefunction ψ_T. Then instead of considering the wavefunction Ψ alone, we introduce the function

$$f(\boldsymbol{R}, \tau) = \psi_T(\boldsymbol{R})\Psi(\boldsymbol{R}, \tau) \; . \tag{2.37}$$

If we multiply the Schroedinger equation (2.22) by $\psi_T(\boldsymbol{R})$, we set the initial wavefunction Ψ_i equal to the trial wavefunction and rearrange all the terms, we obtain an equation for the function f, which has the following form:

$$\begin{aligned} -\frac{\partial}{\partial \tau} f &= -D \sum_i \Delta_i f + D \sum_i \nabla_i \left[F_i f\right] + \left[E_L - E_{ref}\right] f \; ; \\ f(\boldsymbol{R}, \tau = 0) &= |\psi_T(\boldsymbol{R})|^2 \; , \end{aligned} \tag{2.38}$$

where F and E_L are the quantum force and the local energy calculated from the trial wavefunction ψ_T (see Sec. (2.3)) and, as in the previous Sections, the index i represents the coordinates of all the particles. Eq.(2.38) is very similar to the original Schroedinger equation, with the formal replacement $V \rightarrow E_L$ and the addition of a "drift" term, which pushes the system along the gradient of the trial wavefunction. Without the branching term $(E_L - E_R)f$ this equation would be formally identical to the Fokker-Plank equation (see for example [CKL81]).

The corresponding integral equation is

$$f(\boldsymbol{R'}, \tau) = \int f(\boldsymbol{R}, 0) G(\boldsymbol{R} \rightarrow \boldsymbol{R'}, \tau) d\boldsymbol{R} \; , \tag{2.39}$$

where now G is the Green's function of the importance sampled differential equation. After a transient time f converges to $\psi_T \varphi_0$.

As for DMC without importance sampling, it is convenient to iterate the projector n times, with small time steps such that suitable approximations can be introduced. In this Section we introduce the first order approximation, while in the next Section we will introduce the second order approximation.

The first order approximation of the Green's function now is

$$\hat{G}(d\tau) = \hat{G}_K(d\tau)\hat{G}_D(d\tau)\hat{G}_B(d\tau) + \mathcal{O}[d\tau^2] = e^{-d\tau \hat{K}} e^{-d\tau \hat{F}} e^{-d\tau(E_L - E_{ref})} + \mathcal{O}[d\tau^2] \; , \quad (2.40)$$

where in coordinate representation one has $\hat{F} f(\boldsymbol{R}) = D \sum_i \nabla_i [F_i(\boldsymbol{R}) f(\boldsymbol{R})]$. The expression for G_K has already been introduced, while that for G_B is the same as for G_V, with the replacement $V \to E_L$. The Green's function G_D obeys the following equation:

$$-\frac{\partial}{\partial \tau} G_D(\boldsymbol{R} \to \boldsymbol{R'}, \tau) = D \sum_i \nabla_{\boldsymbol{R}'_i} [F_i(\boldsymbol{R'}) G_D(\boldsymbol{R} \to \boldsymbol{R'}, \tau)] \; ; \quad (2.41)$$

$$G_D(\boldsymbol{R} \to \boldsymbol{R'}, 0) = \delta(\boldsymbol{R} - \boldsymbol{R'}) \; ,$$

which can be rewritten as

$$G_D(\boldsymbol{R} \to \boldsymbol{R'}, d\tau) = \delta(\boldsymbol{\mathcal{R}}(d\tau) - \boldsymbol{R'}) \; ,$$

$$\frac{\partial \boldsymbol{\mathcal{R}}(\tau)}{\partial \tau} = D\boldsymbol{F}(\boldsymbol{\mathcal{R}}(\tau)) \; , \quad \boldsymbol{\mathcal{R}}(0) = \boldsymbol{R} \; . \quad (2.42)$$

If the quantum force was a constant vector F_i, then the solution would simply be the initial condition shifted with constant velocity F_i (that is why the quantum force is also called the drift velocity):

$$G_D(\boldsymbol{R} \to \boldsymbol{R'}, d\tau) = \delta(\boldsymbol{R} + d\tau D\boldsymbol{F} - \boldsymbol{R'}) \; . \quad (2.43)$$

We will retain this approximation, which is good provided $d\tau$ is very small and F_i not too large. In fact when the trial wavefunction goes to zero, so that F_i diverges, this is a very bad approximation and suitable cut-offs have to be artificially introduced, or more refined methods have to be used (see for example [UNR93] and references therein). Note that G_D is not diagonal in coordinate representation, but it is a δ-function so that the total Green's function to linear order is

$$G(\boldsymbol{R} \to \boldsymbol{R'}, d\tau) \approx \int G_V(\boldsymbol{R}, d\tau) G_D(\boldsymbol{R} \to \boldsymbol{R}_1, d\tau) G_K(\boldsymbol{R}_1 \to \boldsymbol{R'}, d\tau) d\boldsymbol{R}_1 = G_K(\boldsymbol{R} + d\tau D\boldsymbol{F} \to \boldsymbol{R'}, d\tau) G_V(\boldsymbol{R}, d\tau) \; . \quad (2.44)$$

So the importance sampled algorithm consists in a drifted Gaussian and a branching step, with the weight not given by the interacting potential anymore, but by the local energy of the trial wavefunction. If ψ_T is a good approximation of the ground state, with this algorithm one has two benefits: the drift accelerates the dynamics towards the ground state and the branching term becomes a very smooth factor. This is very useful especially when one deals with interacting potentials which are unbounded (for example the Coulomb potential). A part from the branching term, the transition matrix (2.44) is the same as the one used in the Smart Monte Carlo algorithm (2.21), with the difference that here $d\tau$ is not an adjustable parameter, but a time step. Again, the Green's function (2.44) is not normalized with respect to the final configuration $\boldsymbol{R'}$ so that the function f changes its normalization with time, unless ψ_T is the exact ground state. As already mentioned, see Appendix B for a discussion on the use of an accept-reject step in the DMC algorithm.

2.5.1 Higher order algorithm

Many efforts have been produced in order to develop higher order algorithms, which should allow the use of larger time steps, at the price of calculating more intermediate quantities. Vrbik [VR86] and Chin [Chi90] provided a set of quadratic algorithms which were used both for bosons [BC94, GBC99] and fermions [CB00, SBC02]. More recently fourth order algorithms have been proposed and applied to bosonic systems [FC01]. It is important to stress that the correct approximation of the Green's function at the desired order is obtained only if the appropriate boundary contact (cusp) conditions are enforced in the trial wavefunction, otherwise spurious terms arise, even proportional to fractional powers of the time step (see the above references).

Here we consider a possible quadratic algorithm (see [VR86, BC94]), which we used to reproduce some of the results of [GBC99].

The short time Green's function is approximated as

$$\hat{G}(d\tau) = \hat{G}_B(d\tau/2)\hat{G}_D(d\tau/2)\hat{G}_K(d\tau)\hat{G}_D(d\tau/2)\hat{G}_B(d\tau/2) + \mathcal{O}[d\tau^3] = e^{-d\tau(E_L-E_{ref})/2}e^{-d\tau\hat{F}/2}e^{-d\tau\hat{K}}e^{-d\tau\hat{F}/2}e^{-d\tau(E_L-E_{ref})/2} + \mathcal{O}[d\tau^3]\,; \quad (2.45)$$

by formal expansion of the exponentials it is easy to check that this approximation is correct to the second order.

The explicit expression of (2.45) in coordinate space requires the expansion of the factorized elementary Green's functions to the second order in $d\tau$; moreover four intermediate integrations over the configuration space have to be introduced. The branching terms G_B are again diagonal in space so that two integrations are eliminated by delta functions. The other two integrations are eliminated by the drift terms G_D (see Eq. (2.42)), which,

to second order, have the form:

$$G_D(\boldsymbol{R}_1 \to \boldsymbol{R}_2, d\tau) = \delta\left(\boldsymbol{R}_1 + d\tau D\boldsymbol{F}(\boldsymbol{R}_1) + \frac{D^2 d\tau^2}{2}\boldsymbol{F}(\boldsymbol{R}_1)\boldsymbol{\nabla}\boldsymbol{F}(\boldsymbol{R}_1) - \boldsymbol{R}_2\right), \tag{2.46}$$

where $\boldsymbol{\nabla}\boldsymbol{F}(\boldsymbol{R}_1)$ formally represents the Hessian matrix of $\log|\psi_T|^2$ calculated in the initial point $\boldsymbol{R_1}$. For avoiding the calculation of the Hessian matrix, to the same order one can write the previous equation in the form:

$$G_D(\boldsymbol{R}_1 \to \boldsymbol{R}_2, d\tau) = \delta\left(\boldsymbol{R}_1 + d\tau D\boldsymbol{F}\left[\boldsymbol{R}_1 + \frac{Dd\tau}{2}\boldsymbol{F}(\boldsymbol{R}_1)\right] - \boldsymbol{R}_2\right) , \tag{2.47}$$

that is using the first order expression with the "velocity" calculated in a position which is drifted half a time step from the initial point. Putting this expression in the expansion of the global Green's function (2.45), we obtain

$$\begin{aligned} G(\boldsymbol{R} \to \boldsymbol{R}', d\tau) = G_V(\boldsymbol{R}, d\tau/2) \int d\boldsymbol{R}_1 \times \\ G_K\left(\boldsymbol{R} + \frac{Dd\tau}{2}\boldsymbol{F}\left[\boldsymbol{R} + \frac{Dd\tau}{4}\boldsymbol{F}(\boldsymbol{R})\right] \to \boldsymbol{R}_1, d\tau\right) \times \\ \delta\left(\boldsymbol{R}_1 + \frac{Dd\tau}{2}\boldsymbol{F}\left[\boldsymbol{R}_1 + \frac{Dd\tau}{4}\boldsymbol{F}(\boldsymbol{R}_1)\right] - \boldsymbol{R}'\right) G_V(\boldsymbol{R}', d\tau/2) + \mathcal{O}[d\tau^3] , \end{aligned} \tag{2.48}$$

where one integration and delta function have been kept in order to avoid the introduction of a Jacobian in the final form of the equation. Indeed, keeping in mind the stochastic process evaluation of this Green's function, one can exploit the delta function by performing the following two-step process:

- Start from old walker at position $\boldsymbol{R}$.
- Draw a random displacement ξ from a Gaussian distribution with zero mean and with variance $\sigma^2 = 2Dd\tau$;
- Calculate the first step $\boldsymbol{R}_1 = \boldsymbol{R} + \xi + \frac{Dd\tau}{2}\boldsymbol{F}\left[\boldsymbol{R} + \frac{Dd\tau}{4}\boldsymbol{F}(\boldsymbol{R})\right]$;
- Calculate the second step $\boldsymbol{R}' = \boldsymbol{R}_1 + \frac{Dd\tau}{2}\boldsymbol{F}\left[\boldsymbol{R}_1 + \frac{Dd\tau}{4}\boldsymbol{F}(\boldsymbol{R}_1)\right]$.

This algorithm requires the calculation of the forces in four different points, so it is computationally expensive. One could then directly substitute the intermediate point $\boldsymbol{R}_1$ into the expression for the final point $\boldsymbol{R}'$ and retain terms up to order $d\tau^2$ (keeping in mind that the random displacement ξ is of order $d\tau^{1/2}$). It is then possible to formulate the following simplified process, which requires the evaluation of the forces in only two different points:

$$\begin{aligned} \boldsymbol{R}_1 &= \boldsymbol{R} + \xi + Dd\tau\boldsymbol{F}(\boldsymbol{R}) ; \\ \boldsymbol{R}' &= \boldsymbol{R}_1 + \frac{Dd\tau}{2}\left(\boldsymbol{F}(\boldsymbol{R}_1) - \boldsymbol{F}(\boldsymbol{R})\right) . \end{aligned} \tag{2.49}$$

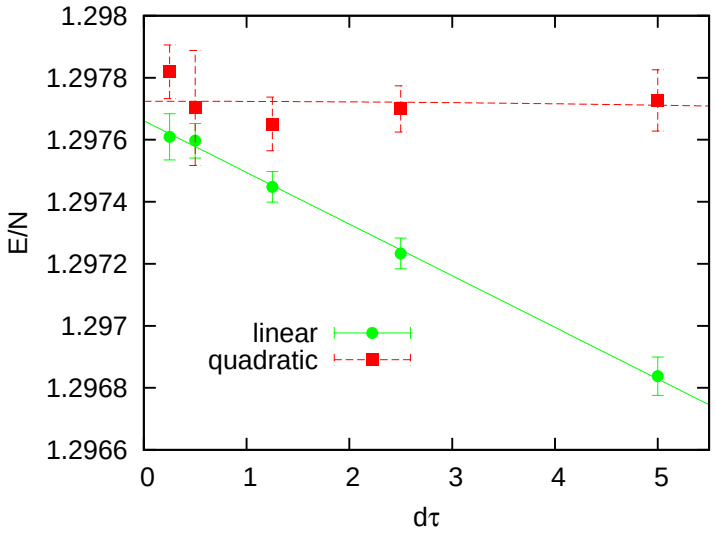

Figure 2.2: Time step dependence of the estimated energy per particle of a $3D$ gas of $N = 100$ soft core bosons with radius $R = 10a$, at the density $na^3 = 10^{-4}$. The time step is measured in units of $(\hbar^2/2ma^2)^{-1}$, while the energy in units of $10^{-3}\hbar^2/2ma^2$. The green circles have been obtained with the linear algorithm (2.44), while the red squares have been obtained with the quadratic algorithm (2.49). The corresponding lines are a linear and a quadratic fit respectively. For comparison, the corresponding value, published in [GBC99] and obtained by simulating $N = 500$ bosons, is $1.303(1) \times 10^{-3}$. The discrepancy is due to finite size effects (checked with an independent simulation with $N = 500$ bosons).

Results from the linear and the quadratic algorithm are reported in Fig. 2.2; they were obtained fixing an equal computational time. It is clear that the time step dependence is almost canceled by using the quadratic algorithm, so that one could simply retain the outcome of a simulation with a relatively large time step, without performing an extrapolation to zero. Unfortunately we were not able to obtain analogous good results in the case of Fermi systems where spurious dependences on the time step arose, probably due to the Fixed Node approximation which is described in the next Section.

2.6 Diffusion Monte Carlo for fermions and Fixed Node approximation

As already mentioned the DMC method is optimal for studying the ground state wavefunction of bosonic systems, which can be taken real and everywhere positive. In the case of fermionic systems, the antisymmetry of the wavefunction imposes the presence of positive and negative regions in

configuration space. The sign of the wavefunction has to be taken into account otherwise the DMC algorithm converges to the bosonic ground state. One possible approach is to consider the sign of the wavefunction as a factor that multiplies the contribution of the single walker to the observables. This has proven to result in a increasing fluctuation of the estimators of the observables with increasing imaginary time, reducing the signal with respect to the noise, so that a refined analysis has to be performed (see [CA80, LSKC81, CA84, CB88]). Many other approaches to the "sign problem" have been proposed, even if it has been demonstrated [TW05] that there is not a general solution, that is an algorithm both exact and convergent in a time which is polynomial in the number of degrees of freedom.

In this Section we will therefore introduce an approximate solution which has been proven to be very precise for the ground state of ultracold gases, the Fixed Node approximation. This approximation strongly relies on importance sampling and the use of a good trial function ψ_T, which can usually be constructed for dilute systems.

The "nodal surface" is the region in configuration space where a wavefunction is zero. A "nodal pocket" is instead a connected region in configuration space whose boundary is a part of the nodal surface. The problem of fermionic wavefunctions (or excited states wavefunctions) is that the sign of the wavefunction changes from a nodal pocket to the next one and the position of the nodal surface is not known a priori. However some symmetry properties of the wavefunction are known if the state under study is an eigenvector of an operator which commutes with the hamiltonian of the problem. A major example regards the antisymmetry of all fermionic wavefunctions with respect to an odd permutation of particles.

The essence of the Fixed Node approximation (FN) is to fix the nodal surface of the studied wavefunction Ψ to be equal to that of a trial wavefunction ψ_T, so that the nodal pockets of Ψ and ψ_T coincide. Then the importance sampling algorithm (Sec. 2.5) is applied to the distribution $f = \psi_T \Psi$ which turns to be everywhere positive, except on the nodal surface, so that the usual bosonic algorithm can be applied, provided that the nodal surface is never crossed. The FN constraint is equivalent to adding an infinite repulsive potential on the nodal surface. This method was introduced in [CA80, Rey82], where it was also demonstrated that it provides an upper bound for the energy of the lowest lying state with the same symmetries of the trial wavefunction. For example, if an antisymmetric trial wavefunction is used, this method is able to "purify" the initial wavefunction from the bosonic component, so that an upper bound for the ground state of the fermionic system is obtained.

Unfortunately, the Fixed Node approximation that we used prevented us for achieving a quadratic behavior in the energy dependence on the time step, even using an in principle quadratic algorithm, so that all the results in this Thesis are obtained with a linear algorithm. See a discussion on

this issue in [UNR93]. However in literature there are claims of successful quadratic algorithms for fermions [SBC02].

2.7 Wavefunctions

For dilute systems, the exact properties of the many-body wavefunction introduced in Sec. 1.4 determine the main features of the equation of state. Once embedded in the trial wavefunctions, these properties allow good VMC results and even better DMC results. For bosons in the ground state, the Jastrow wavefunction [McM65, GBC99] was able to capture the few-body correlations which dominate the dilute systems physics, while for fermions the Slater [CCK77] or BCS determinants [BGL88, CCPS03, ABCG04] proved very accurate in describing the nodal surface.

It is a good practice to enforce the cusp conditions (1.10,1.11) in the trial wavefunction. This guarantees the exactness of the wavefunction at the two-body level at short distances and results in a smoother sampling of the local energy, so that the variance is greatly reduced. In literature some major trial wavefunctions have been used which can easily respect the cusp conditions: the Jastrow wavefunction for bosons and the Jastrow-Slater and BCS wavefunction for fermions.

2.7.1 Jastrow wavefunction

The Jastrow wavefunction is a symmetrized product of few-body wavefunctions which respect the cusp conditions. The simplest form contains only the two-body terms and reads $\Psi_J(\boldsymbol{R}) = \prod_{i<j} f(r_{ij})$, where the product is extended over all the pairs of interacting particles and $r_{ij} = |r_i - r_j|$ (in literature this function is often written as $\Psi_J(\boldsymbol{R}) = e^{\sum_{i<j} u(r_{ij})}$). In case of short range interactions the function f is taken to be a solution of the two-body problem, so that the cusp conditions (1.10,1.11) are automatically implemented. In case one considers two species of particles (let us call them up, $\uparrow$, and down, $\downarrow$), the general (two-body) Jastrow function is:

$$\Psi_J(\boldsymbol{R}) = J_{\uparrow\uparrow}(\boldsymbol{R}) J_{\downarrow\downarrow}(\boldsymbol{R}) J_{\uparrow\downarrow}(\boldsymbol{R}) = \prod_{i<j} f_{\uparrow\uparrow}(r_{ij}) \prod_{a<b} f_{\downarrow\downarrow}(r_{ab}) \prod_{i,a} f_{\uparrow\downarrow}(r_{ia}) \ , \tag{2.50}$$

where the indexes i, j refer to the $\uparrow$ particles and the indexes a, b refer to the $\downarrow$ particles. The quantum forces $F^{\alpha}_{i,a}$, where the index $\alpha = x, y, z$ refer to the spatial coordinate, reduce to

$$F^{\alpha}_{\uparrow\uparrow i} = 2\frac{\partial_{\alpha_i} J_{\uparrow\uparrow}}{J_{\uparrow\uparrow}} = 2\sum_{j\neq i} \frac{\partial_{\alpha_i} f_{\uparrow\uparrow}(r_{ij})}{f_{\uparrow\uparrow}(r_{ij})} = 2\sum_{j\neq i} \frac{f'_{\uparrow\uparrow}(r_{ij})}{f_{\uparrow\uparrow}(r_{ij})} \frac{\alpha_i - \alpha_j}{r_{ij}} \ , \tag{2.51}$$

for the $\uparrow\uparrow$ case and analogously for the other cases.

The local kinetic energy of the Jastrow wavefunction is

$$K = D\left\{2\sum_{i<j}\left[e^L_{\uparrow\uparrow}(r_{ij}) + \left(\frac{f'_{\uparrow\uparrow}(r_{ij})}{f_{\uparrow\uparrow}(r_{ij})}\right)^2\right] + 2\sum_{a<b}\left[e^L_{\downarrow\downarrow}(r_{ab}) + \left(\frac{f'_{\downarrow\downarrow}(r_{ab})}{f_{\downarrow\downarrow}(r_{ab})}\right)^2\right]\right.$$
$$\left. +2\sum_{i,a}\left[e^L_{\uparrow\downarrow}(r_{ia}) + \left(\frac{f'_{\uparrow\downarrow}(r_{ia})}{f_{\uparrow\downarrow}(r_{ia})}\right)^2\right] - \frac{1}{4}\left(\boldsymbol{F}_S\cdot\boldsymbol{F}_S + \boldsymbol{F}_A\cdot\boldsymbol{F}_A + 2\boldsymbol{F}_S\cdot\boldsymbol{F}_A\right)\right\}, \tag{2.52}$$

where the global force vectors are $\boldsymbol{F}_S = \{F^\alpha_{\uparrow\uparrow i}, F^\alpha_{\downarrow\downarrow a}\}$ and $\boldsymbol{F}_A = \{F^\alpha_{\uparrow\downarrow i}, F^\alpha_{\uparrow\downarrow a}\}$ and $e^L = -(f'' + (d-1)f'/r)/f$ is the the local kinetic energy of the two-body problem in units of $2D$. Note that the last term can be written as $\frac{1}{4}\boldsymbol{F}\cdot\boldsymbol{F}$ where the scalar product is meant as a sum over the coordinates of all the particles. Note also that in the case of one single $\uparrow$ particle and one single $\downarrow$ particle the above expression is reduced to $K = 2De^L_{\uparrow\downarrow}$ as it should. See Appendix C for the details of the calculation.

2.7.2 Slater Determinant

In the study of fermionic systems the Jastrow wavefunction cannot be used alone, since it is symmetric in the exchange of particles. The simplest antisymmetric wavefunction originates adiabatically from the wavefunction of the non interacting Fermi Gas, which is a Slater determinant. As in Fermi Liquid Theory [Lan57, AK59, NP89] one assumes a one-to-one mapping between the low-energy excitations of the interacting liquid and those of the non interacting gas. When performing a VMC calculation, the optimization of the single particle orbitals appearing in the Slater determinant is crucial, so that self-consistent mean-field calculations (Hartree-Fock), or backflow correlations have been used; multi-determinant wavefunctions, which are more accurate, but also more computationally expensive, have also been considered (see [BMWS08]). Diffusion Monte Carlo instead only requires a good nodal surface. In principle one should optimize the Slater determinant orbitals in this case too, and this is necessary for high density systems [GBC02]. For dilute systems instead the non-interacting single particle orbitals proved good enough for comparing the results to experiments (see [ABCG04, PG08]), so we used plane waves for the homogeneous systems we considered.

A more refined wavefunction, which is able to account for more correlations, is the Jastrow-Slater wavefunction. In case of two species of fermions without spin-flip interactions, it can be written as a product of two different Slater determinants and a Jastrow factor, in the following way:

$$\Psi_{JS} = \Psi_J D_\uparrow D_\downarrow\,, \tag{2.53}$$

where the determinants are defined as follows:

$$D_\uparrow(\boldsymbol{R}_\uparrow) = \det S_{\uparrow pi} = \det\left[\psi_{\boldsymbol{k}_p}(\boldsymbol{r}_i)\right], \quad D_\downarrow(\boldsymbol{R}_\downarrow) = \det S_{\downarrow ra} = \det\left[\psi_{\boldsymbol{k}_r}(\boldsymbol{r}_a)\right] . \tag{2.54}$$

The $\psi_{\boldsymbol{k}_p}$ and $\psi_{\boldsymbol{k}_r}$ orbitals are single particle wavefunctions corresponding to eigenvectors of momentum in a box with periodic boundary conditions. In order to have a real wavefunction we used the $\cos(\boldsymbol{kr})$ and $\sin(\boldsymbol{kr})$ functions. For the $\boldsymbol{k}$ vectors we choose the eigenvalues of momentum starting from the zero vector up to the Fermi wavevector fixed by the number of particles and the volume of the box (in the thermodynamic limit only by the density).

In the following we will derive all the properties for $D_\uparrow$, those of $D_\downarrow$ being the same with a suitable change of indexes. It is convenient to introduce the inverse Slater matrix, whose properties are:

$$\sum_i S_{pi}\bar{S}_{iq} = \sum_i \psi_{\boldsymbol{k}_p}(\boldsymbol{r}_i)\bar{S}_{iq} = \delta_{pq} \; ; \quad \sum_p \bar{S}_{jp}\psi_{\boldsymbol{k}_p}(\boldsymbol{r}_i) = \sum_p \bar{S}_{jp}S_{pi} = \delta_{ij} \; . \tag{2.55}$$

Since the iterative calculation of the determinant involves the cofactors A_{pi} in the equation $D_\uparrow = \sum_i S_{ip}A_{pi}$, for any p, the inverse matrix is related to the cofactors in the following way: $\bar{S}_{pi} = A_{pi}/D_\uparrow$. Two useful properties can therefore be deduced, concerning the derivatives of the Slater determinant:

$$\begin{aligned} \frac{1}{D_\uparrow}\frac{\partial D_\uparrow}{\partial S_{ip}} &= \bar{S}_{pi} \; ; \\ \frac{\partial \bar{S}_{pi}}{\partial S_{jq}} &= -\bar{S}_{qi}\bar{S}_{pj} \; . \end{aligned} \tag{2.56}$$

It is now possible to derive the quantum forces for the Slater determinant:

$$F_i^\alpha = \frac{2}{D_\uparrow}\partial_{\alpha_i} D_\uparrow = \frac{2}{D_\uparrow}\sum_p \frac{\partial D_\uparrow}{\partial S_{ip}}\frac{\partial S_{ip}}{\partial \alpha_i} = 2\sum_p \bar{S}_{pi}\partial_{\alpha_i}\psi_{\boldsymbol{k}_p}(\boldsymbol{r}_i) \; . \tag{2.57}$$

The local kinetic energy is:

$$\begin{aligned} K &= -\frac{D}{D_\uparrow}\sum_i\sum_\alpha^d \partial^2_{\alpha_i} D_\uparrow = -\frac{D}{D_\uparrow}\sum_i\sum_\alpha^d \partial_{\alpha_i}\left[D_\uparrow \sum_p \bar{S}_{pi}\frac{\partial S_{ip}}{\partial \alpha_i}\right] \\ &= -D\sum_i\sum_\alpha^d \left[\left(\sum_{pq}\bar{S}_{qi}\frac{\partial S_{iq}}{\partial \alpha_i}\bar{S}_{pi}\frac{\partial S_{ip}}{\partial \alpha_i}\right) - \left(\sum_{pq}\bar{S}_{qi}\frac{\partial S_{iq}}{\partial \alpha_i}\bar{S}_{pi}\frac{\partial S_{ip}}{\partial \alpha_i}\right)\right. \\ &\quad \left. + \sum_p \bar{S}_{pi}\partial^2_{\alpha_i}\psi_{\boldsymbol{k}_p}(\boldsymbol{r}_i)\right] = -D\sum_{i,p}\sum_\alpha^d \bar{S}_{pi}\partial^2_{\alpha_i}\psi_{\boldsymbol{k}_p}(\boldsymbol{r}_i) \; . \end{aligned} \tag{2.58}$$

In the homogeneous system which we consider, the last expression simply turns into $K = D\sum_p k_p^2$, where k_p is the modulus of the $p-th$ eigenvector

of momentum. Let us now consider the wavefunction (2.53) and use the superscript S, J for indicating the quantum forces and the kinetic energy of the Slater determinants or the Jastrow factor respectively. The total quantum forces are simply $\boldsymbol{F} = \boldsymbol{F}^J + \boldsymbol{F}^S_\downarrow + \boldsymbol{F}^S_\uparrow$ (where again the indexes of these vectors correspond to the ordered coordinates of all the particles). The total local kinetic energy results in:

$$K^{JS} = \\ -\frac{D}{\Psi_{JS}}\left(\sum_{i,\alpha}\partial_{\alpha_i}\Psi_{JS} + \sum_{a,\alpha}\partial_{\alpha_a}\Psi_{JS}\right) = K^J + K^S_\uparrow + K^S_\downarrow - \frac{D}{2}(\boldsymbol{F}^J \cdot \boldsymbol{F}^S)\ . \tag{2.59}$$

Due to the calculation of a determinant, each update of the wavefunction requires $\propto dof^3$ steps.

2.7.3 BCS wavefunction

The nodal surface of a Slater determinant wavefunction is not able to account for pairing effects, unless one performs a sum over many different determinants, which is computationally very heavy. In this case a better nodal surface is provided by the BCS wavefunction. The latter was introduced by Bardeen, Cooper and Schrieffer [BCS57] within the grand-canonical ensemble, for a variational study of superconductivity in the weak coupling regime. Later, Leggett [Leg80] extended it to the canonical ensemble and to the intermediate and strong coupling regimes (BCS-BEC crossover). This kind of wavefunction was proposed then for the study of ^3He and further studied in [BGL88]. It has finally been used in the study of ultracold gases in the BCS-BEC crossover [CCPS03, ABCG04].

In its canonical ensemble form, the BCS wavefunction in the singlet channel reads:

$$\Psi_{BCS} = \det\left[\varphi(\boldsymbol{r}_i - \boldsymbol{r}_a)\right]\ , \tag{2.60}$$

where φ is a pair orbital. See [BMWS08] for extensions of this kind of wavefunction, such as Geminal or Pfaffian wavefunctions. The pair orbital can be any function of the coordinates of one $\uparrow$ particle and one $\downarrow$ particle, provided it fulfills the boundary conditions, for example the bound state of the two-body problem φ_b. It has been demonstrated [BGL88] that if the pair orbital is the sum of products of single particle plane waves up to the Fermi surface, then the BCS wavefunction reduces to the product of two Slater determinants as in (2.53). In literature [CCPS03, ABCG04] a combination of the spherical and the single-particle originated orbitals have been used:

$$\varphi(\boldsymbol{r}_i - \boldsymbol{r}_a) = \beta_s\varphi_b(|\boldsymbol{r}_i - \boldsymbol{r}_a|) + \sum_p^{p_{max}} \beta_p \exp\left[i\boldsymbol{k}_p(\boldsymbol{r}_i - \boldsymbol{r}_a)\right]\ , \tag{2.61}$$

where the parameters β_s, β_p, p_{max} have to be optimized. In the problem considered in Chap. 4 we used the previous orbital with the assumption $\beta_p = \beta$, $\beta_s = \sqrt{1-\beta^2}$ and p_{max} on the Fermi surface, but we found that setting either $\beta = 0$ or $\beta = 1$ gave lower energy than $0 < \beta < 1$.

Profiting of the properties of the determinants introduced in the previous Section, we can now calculate the quantum forces and the kinetic energy of the BCS wavefunction, considering the case of a spherically symmetric orbital ($\beta = 0$). Let us call the elements of the BCS matrix B_{ia}, and those of the inverse BCS matrix $\bar{B}_{ai}$. The quantum forces are:

$$\begin{aligned} F_i^\alpha &= \frac{2}{\Psi_{BCS}} \partial_{\alpha_i} \Psi_{BCS} = \frac{2}{\Psi_{BCS}} \sum_a \frac{\partial \Psi_{BCS}}{\partial B_{ia}} \partial_{\alpha_i} B_{ia} \\ &= 2 \sum_a \bar{B}_{ai} \varphi'(|\boldsymbol{r}_i - \boldsymbol{r}_a|) \frac{\alpha_i - \alpha_a}{|\boldsymbol{r}_i - \boldsymbol{r}_a|} \\ F_a^\alpha &= -2 \sum_i \bar{B}_{ai} \varphi'(|\boldsymbol{r}_i - \boldsymbol{r}_a|) \frac{\alpha_i - \alpha_a}{|\boldsymbol{r}_i - \boldsymbol{r}_a|} \ . \end{aligned} \tag{2.62}$$

The kinetic energy is

$$\begin{aligned} K &= -\frac{D}{\Psi_{BCS}} \left(\sum_i \sum_\alpha^d \partial_{\alpha_i}^2 \Psi_{BCS} + \sum_a \sum_\alpha^d \partial_{\alpha_a}^2 \Psi_{BCS} \right) \\ &= -\frac{D}{\Psi_{BCS}} \left[\sum_i \sum_\alpha^d \partial_{\alpha_i} \left(\Psi_{BCS} \sum_a \bar{B}_{ai} \partial_{\alpha_i} B_{ia} \right) \right. \\ &\left. - \sum_a \sum_\alpha^d \partial_{\alpha_a} \left(\Psi_{BCS} \sum_a \bar{B}_{ai} \partial_{\alpha_a} B_{ia} \right) \right] \\ &= -D \sum_{ia} \sum_\alpha^d \left(\bar{B}_{ai} \partial_{\alpha_i}^2 B_{ia} + \bar{B}_{ai} \partial_{\alpha_a}^2 B_{ia} \right) = 2D \sum_{ia} \bar{B}_{ai} \varepsilon^L(|\boldsymbol{r}_i - \boldsymbol{r}_a|) \ , \end{aligned} \tag{2.63}$$

where we have used the fact $\partial_{\alpha_i}^2 B_{ia} = \partial_{\alpha_a}^2 B_{ia}$ and we have introduced $\varepsilon^L(r) = -\varphi''(r) - \frac{d-1}{r}\varphi'(r)$.

It can also be useful to use a more general wavefunction, containing both the BCS determinant and a Jastrow factor $\Psi_J \Psi_{BCS}$, in order to introduce correlations within $\uparrow\uparrow$ and $\downarrow\downarrow$ pairs. The calculations of the forces and the kinetic energy proceed in a similar way as in the previous Section.

2.7.4 Wavefunctions for the polarized case

When studying the case of two species of fermions, with $N_\uparrow > N_\downarrow$, the wavefunctions described in the previous Sections have to be generalized. The Jastrow wavefunction is already capable of handling the polarized case, the same is true for the product of two Slater determinants.

For the BCS pairing determinant a generalization has been proposed in the context of liquid ^3He [BGL88], and it has been successfully used for studying ultracold gases [CCPS03, PG08]. This wavefunction has the form of an antisymmetrized product of $N_\downarrow$ two-particle orbitals and $A = N_\uparrow - N_\downarrow$ single particle orbitals, for the excess $\uparrow$ particles:

$$\Psi_{PBCS} = \det \begin{pmatrix} \varphi(11) & \varphi(12) & \cdots & \varphi(1N_\downarrow) & \psi_1(1) & \cdots & \psi_A(1) \\ \varphi(21) & \varphi(22) & \cdots & \varphi(2N_\downarrow) & \psi_1(2) & \cdots & \psi_A(2) \\ \vdots & \ddots & \ddots & \vdots & \vdots & \ddots & \vdots \\ \varphi(N_\uparrow 1) & \cdots & \cdots & \varphi(N_\uparrow N_\downarrow) & \psi_1(N_\uparrow) & \cdots & \psi_A(N_\uparrow) \end{pmatrix} \tag{2.64}$$

The calculation of the forces and the kinetic energy is similar to that for the previously introduced wavefunctions.

An even more general form, which we did not use, includes $M < N_\downarrow$ two-particle orbitals, $N_\uparrow - M$ single particle orbitals for the $\uparrow$ excess particles, $N_\downarrow - M$ single particle orbitals for the $\downarrow$ excess particles.

2.8 Observables

In this Section we discuss about the calculation of correlation functions within VMC and DMC. One can consider one- or many-body correlation functions; in the case of dilute gases an important role is played by the one- and two-body ones, since the probability of having three close particles is very small. See Sec. 1.2 for the definition of the one-body density matrix (OBDM), the pair distribution functions and the off-diagonal two-body density matrix (TBDM).

The estimators of the observables calculated with VMC are called variational estimators:

$$\langle \hat{O} \rangle_V = \frac{\langle \psi_T | \hat{O} | \psi_T \rangle}{\langle \psi_T | \psi_T \rangle} , \tag{2.65}$$

while those calculated with DMC are called mixed estimators:

$$\langle \hat{O} \rangle_M = \frac{\langle \psi_T | \hat{O} | \varphi_0 \rangle}{\langle \psi_T | \varphi_0 \rangle} . \tag{2.66}$$

Only in the case of $[\hat{O}, \hat{H}] = 0$ the corresponding mixed estimator can be exact (for example in the case $\hat{O} = \hat{H}$). In general the mixed estimator is an approximation of the pure one (see [SBC02] for the direct calculation of pure estimators in DMC). One can write $\varphi_0 = \psi_T + \delta\psi$ and the pure estimator can be approximated with the extrapolated estimator:

$$\langle \hat{O} \rangle_P = \frac{\langle \varphi_0 | \hat{O} | \varphi_0 \rangle}{\langle \varphi_0 | \varphi_0 \rangle} = \frac{\langle \psi_T + \delta\psi | \hat{O} | \psi_T + \delta\psi \rangle}{\langle \psi_T + \delta\psi | \psi_T + \delta\psi \rangle} \approx 2\langle \hat{O} \rangle_M - \langle \hat{O} \rangle_V = \langle \hat{O} \rangle_E , \tag{2.67}$$

provided $\delta\psi \ll \psi$.

In order to estimate the previously introduced correlation functions, it is necessary to rewrite them in the first quantization form. Let us directly consider the mixed estimators; the variational ones are simply obtained by substituting $\varphi_0 \to \psi_T$. Let us indicate all the coordinates with the symbol $\boldsymbol{R}$ and all the coordinates except some, which are evident from the context, with $\bar{\boldsymbol{R}}$.

For the OBDM one has:

$$n_\sigma(r) = \frac{1}{n_\sigma \Omega_d} \sum_i^{N_\sigma} \int d\hat{\boldsymbol{r}} \frac{\int \psi_T(\boldsymbol{r}_{\sigma i} + \boldsymbol{r}, \bar{\boldsymbol{R}}) \varphi_0(\boldsymbol{r}_{\sigma i}, \bar{\boldsymbol{R}}) d\bar{\boldsymbol{R}}}{\langle \psi_T | \varphi_0 \rangle} , \tag{2.68}$$

where an average over the σ particles and over the solid angle corresponding to $\boldsymbol{r}$ is taken; n_σ is the particle density of the n_σ particles and Ω_d is the total solid angle in dimension d. Profiting of the homogeneity of the system and introducing the DMC sampling probability one obtains

$$n_\sigma(r) = \frac{1}{N_\sigma} \sum_i^{N_\sigma} \frac{1}{\Omega_d} \int d\hat{\boldsymbol{r}} \frac{\int \frac{\psi_T(\boldsymbol{r}_{\sigma i} + \boldsymbol{r}, \bar{\boldsymbol{R}})}{\psi_T(\boldsymbol{r}_{\sigma i}, \bar{\boldsymbol{R}})} f(\boldsymbol{r}_{\sigma i}, \bar{\boldsymbol{R}}) d\boldsymbol{R}}{\int f(\boldsymbol{R}) d\boldsymbol{R}} . \tag{2.69}$$

The quantity to accumulate is therefore $\frac{\psi_T(\boldsymbol{r}_{\sigma i} + \boldsymbol{r}, \bar{\boldsymbol{R}})}{\psi_T(\boldsymbol{r}_{\sigma i}, \bar{\boldsymbol{R}})}$, which is easy to calculate with the wavefunctions described in the previous Section, since the change of only one particle is involved. The average on the solid angle is done by sampling M times the vector $\boldsymbol{r}$ in a uniform random way (so that $\frac{1}{\Omega_d} \int d\hat{\boldsymbol{r}} \to \frac{1}{M} \sum^M$). Then an histogram is produced which accumulates the observable for bins with support $[r_n, r_n + \Delta r)$, where Δr sets up the finest scale that one wants to probe (the smaller Δr, the longer the computation will have to be in order to get enough statistics). The use of a bin of width Δr requires a further normalization $1/\Delta r$.

The calculation of the two-particle distribution functions is easier, since in a sense they are "diagonal", that is they do not involve the change of a particle position, since they measure the relative frequency of distances between particles in the original state. The two-particle parallel spin distribution function can be written as:

$$g^{(2)}_{\sigma\sigma}(r) = \frac{2}{n_\sigma^2 \Omega_d} \times$$
$$\sum_{i<j}^{N_\sigma} \int d\hat{\boldsymbol{r}} \frac{\int \psi_T(\boldsymbol{r}_{\sigma i}, \boldsymbol{r}_{\sigma j} = \boldsymbol{r}_{\sigma i} + \boldsymbol{r}, \bar{\boldsymbol{R}}) \varphi_0(\boldsymbol{r}_{\sigma i}, \boldsymbol{r}_{\sigma j} = \boldsymbol{r}_{\sigma i} + \boldsymbol{r}, \bar{\boldsymbol{R}}) d\bar{\boldsymbol{R}}}{\langle \psi_T | \varphi_0 \rangle} , \tag{2.70}$$

where the sum comes from acting with the field operators on the original state and the factor 2 is inserted in order to count all the pairs. Again, using the homogeneity one can integrate also over $\boldsymbol{r}_i$ and $\boldsymbol{r}_j$ keeping track of

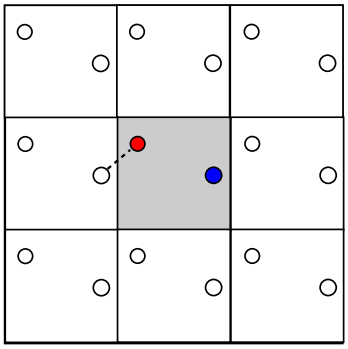

Figure 2.3: Periodic boundary conditions and closest replica.

their relation with a delta function $\delta(\boldsymbol{r}_{\sigma j} - \boldsymbol{r}_{\sigma i} - \boldsymbol{r}) = \delta(r - |\boldsymbol{r}_{\sigma j} - \boldsymbol{r}_{\sigma i}|)\delta(\hat{\boldsymbol{r}} - \hat{(\boldsymbol{r}_{\sigma j} - \boldsymbol{r}_{\sigma i})})/r^d$, which eliminates the integration over the solid angle, but introduces a factor r^{-d}:

$$g^{(2)}_{\sigma\sigma}(r) = \frac{2}{n_\sigma N_\sigma \Omega_d r^d} \sum_{i<j}^{N_\sigma} \frac{\int \delta(r - |\boldsymbol{r}_{\sigma j} - \boldsymbol{r}_{\sigma i}|) f(\boldsymbol{r}_{\sigma i}, \boldsymbol{r}_{\sigma j}, \bar{\boldsymbol{R}}) d\boldsymbol{R}}{\int f(\boldsymbol{R}) d\boldsymbol{R}} \,. \tag{2.71}$$

Differently from the OBDM here the factor Ω_d is explicit, since there is no need to sample the displacement $\boldsymbol{r}$.

In case of antiparallel spins, with similar reasoning, one has:

$$g^{(2)}_{\uparrow\downarrow}(r) = \frac{1}{n_\uparrow N_\downarrow \Omega_d r^d} \sum_{i,a} \frac{\int \delta(r - |\boldsymbol{r}_{\downarrow a} - \boldsymbol{r}_{\uparrow i}|) f(\boldsymbol{r}_{\uparrow i}, \boldsymbol{r}_{\downarrow a}, \bar{\boldsymbol{R}}) d\boldsymbol{R}}{\int f(\boldsymbol{R}) d\boldsymbol{R}} \,. \tag{2.72}$$

Also in this case the results need to be presented in the form of an histogram.

The estimator of the off-diagonal TBDM can be deduced in the same way as for the OBDM, and one obtains

$$g^{II}(r) = \frac{1}{N_\uparrow N_\downarrow} \sum_{i,a} \frac{1}{\Omega_d} \int d\hat{\boldsymbol{r}} \frac{\int \frac{\psi_T(\boldsymbol{r}_{\uparrow i} + \boldsymbol{r},\, \boldsymbol{r}_{\downarrow a} + \boldsymbol{r},\, \bar{\boldsymbol{R}})}{\psi_T(\boldsymbol{r}_{\uparrow i},\, \boldsymbol{r}_{\downarrow a},\, \bar{\boldsymbol{R}})} f(\boldsymbol{r}_{\sigma i},\ \bar{\boldsymbol{R}}) d\boldsymbol{R}}{\int f(\boldsymbol{R}) d\boldsymbol{R}} \,. \tag{2.73}$$

2.9 Boundary conditions, finite size scaling and dependence on the number of walkers

Being interested in bulk properties, suitable and usual periodic boundary conditions (PBC) can be used. The simulation cell is a $dN-$ dimensional hypercube with size L. The volume of the elementary $d-$ dimensional cell is fixed by the density and the number of particles so that $L^d = N/n$. The implementation of PBC requires a regular behavior of the trial wavefunctions

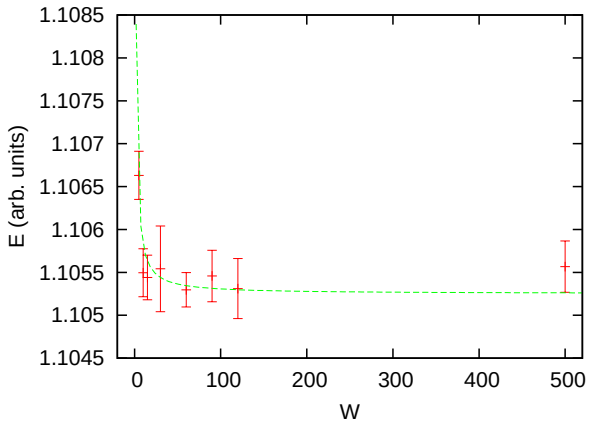

Figure 2.4: Example of the dependence of energy on the number of walkers W.

at the boundary of the simulation box: in the case of Slater determinants, the single particle orbitals must have a period for which L is an integer multiple; in the case of the Jastrow factors or the BCS spherical orbitals, which are pair functions, one requires that at the distance $r = L/2$ the function goes to a constant, its derivative going to zero. In the Monte Carlo moves, every time a particle exits the elementary box, it is moved inside the box subtracting or adding an integer number of times the length L. Moreover, when calculating properties involving a pair of particles, one has to consider the closest replica of the particles (see Fig. 2.3).

Since our simulations are done in the canonical ensemble, the fixed and limited number of particles introduces finite size errors if the aim is calculating the properties of the system in the thermodynamic limit. In general one expects a ϵ/N^ν dependence on the number of particles, for large N, with the exponent ν and the coefficient ϵ depending on the observable [LZC01]. We have observed a different finite-size scaling of the various wavefunctions we used. In the case of the BCS wavefunction, there was no significant dependence on N, within the statistical errors. For the JS wavefunction we observed a dependence which is explainable in the framework of Fermi liquid theory (See [LZC01]). Actually one can assume that the kinetic energy difference between the thermodynamic limit system and the finite size system, in the interacting case, is proportional to the same difference calculated for the non-interacting system, due to the correspondence between the excitations of a Fermi liquid and a Fermi gas. One then has $E_\infty \approx E_N + \frac{m}{m^*}(K_\infty - K_N)$; for the accuracy that we needed, we approximated the effective mass $m^* \approx m$ in the previous formula and this provided a consistency of the results with different numbers of particles, within the statistical uncertainty.

Another source of systematic errors is the finite number W of walkers. Due to the central limit theorem, for large W the deviation from the correct result scales as $1/\sqrt{W}$. So one has to increase the number of walkers in order to keep this error within the statistical uncertainty. In our simulations, due to the dilute nature of the systems under consideration, $W = 100$ was sufficient (see Fig. 2.4 for an example).

Chapter 3

Itinerant ferromagnetism in a three dimensional repulsive Fermi gas

In this Chapter we apply the VMC and DMC techniques to the problem of itinerant ferromagnetism in repulsive or effectively repulsive ultracold Fermi gases. In condensed matter physics ferromagnetic phenomena have been studied within lattice or continuum models and the role of the lattice is still not completely clear. In this Chapter, which is based on the published paper [PBGT10], we show evidence of a ferromagnetic quantum phase transition even without a lattice, in the context of repulsive dilute Fermi gases.

3.1 Introduction

Over the past decade there has been substantial progress in the experimental realization of quantum degenerate atomic Fermi gases. A major part of the activity carried out so far was devoted to the investigation of the role of *attractive* interactions, with special emphasis on the onset of pairing and superfluidity in the vicinity of a Feshbach resonance as well as in the presence of spin imbalance [GPS08]. More recently attention was drawn to *repulsive* interactions and the onset of magnetic behavior. This topic is particularly important in optical lattices because of its connection with the repulsive Hubbard model, a fundamental paradigm of condensed matter physics with still many unanswered questions [Geo07], but also for continuous systems where a major recent achievement has been the observation of itinerant ferromagnetism induced by repulsive forces in a two-component Fermi gas [JLC$^+$09]. This experiment realizes the Stoner model, a textbook Hamiltonian that aims to describe itinerant ferromagnetism in an electron gas with screened Coulomb interaction [Sto33].

On the theoretical side there have been a number of papers addressing the problem of stability of a repulsive two-component Fermi gas [HFS$^+$97] and of phase separation in harmonic trapped configurations within the local density approximation [AMMT00, SPPR00, LTBP09, SY02]. These studies are based on a simple mean-field description of interaction effects that is valid to linear order in the scattering length. In homogeneous systems at $T = 0$ they predict a second order phase transition to a magnetized state if the interaction strength is larger than the critical value $k_F a > \pi/2$, where a is the s-wave scattering length and $k_F = (3\pi^2 n)^{1/3}$ is the Fermi wave vector in terms of the total particle density of the gas $n = n_\uparrow + n_\downarrow$. An extension of this approach that includes next order corrections to the interaction energy was developed in Ref. [DM05] and predicts a smaller value of the critical density ($k_F a > 1.054$), as well as a discontinuous jump in the magnetization. Low-energy theories of itinerant fermions also predict a first-order transition [BKV99]. A recent non-perturbative quantum Monte Carlo calculation, instead, suggests the existence of a textured magnetic phase at the border of the ferromagnetic transition and yields the value $k_F a \simeq 0.8$ for the critical density [CGS09]. On the other hand, the existence of a ferromagnetic transition has been questioned in Ref. [Zha09] by arguing that nonmagnetic states with strong short-ranged repulsive correlations could be energetically favorable compared to ferromagnetic ones.

Various important issues concerning the regime of strong repulsion are still open. In this Chapter we provide answer to some of them, in particular:

i) we calculate the equation of state of the Fermi gas using different potentials to determine the regime of interaction strength $k_F a$ where universality in terms of just the s-wave scattering length a is lost and other parameters of the interatomic potential become relevant;

ii) we study population imbalanced configurations and show that the equation of state of the highly polarized gas can be described in terms of a Fermi liquid of polarons, similarly to the well-established case of attractive interactions [LRGS06, SZS$^+$06, PS08, SWSZ09, NNJ$^+$10];

iii) we investigate the onset of ferromagnetism and show how the physics of polarons is related to the stability of the ferromagnetic states;

iv we establish the phase diagram in the polarization/interaction plane where we determine the borders of three phases: a uniformly polarized phase and mixed phases consisting of partially or fully polarized domains, as shown in Fig. 3.1. Our analysis of the pure phases has been limited to uniform magnetic orders.

3.2 Method

To address these issues we perform quantum Monte Carlo (QMC) simulations of Fermi systems characterized by a positive scattering length $a > 0$, interacting through either purely repulsive or purely attractive forces. The Hamiltonian of the Fermi gas is

$$H = -\frac{\hbar^2}{2m}\left(\sum_{i=1}^{N_\uparrow}\nabla_i^2 + \sum_{i'=1}^{N_\downarrow}\nabla_{i'}^2\right) + \sum_{i,i'}V(r_{ii'})\ , \tag{3.1}$$

where m denotes the mass of the atoms, $i, j, ...$ and $i', j', ...$ label, respectively, spin-up and spin-down fermions with $N_\uparrow + N_\downarrow = N$, N being the total number of atoms. We model the interspecies interatomic interactions using three different potentials:

i) a *hard sphere* (HS) potential, $V(r) = +\infty$ if $r < a$ and zero otherwise,

ii) a repulsive *soft sphere* (SS) potential, $V(r) = V_0$ if $r < R_0$ and zero otherwise,

iii) an attractive *square well* (SW) potential, $V(r) = -V_0$ if $r < R_0$ and zero otherwise ($V_0 > 0$).

The s-wave scattering length a coincides with the range of the potential in the HS case and can readily be determined from the range R_0 and the strength V_0 in the other two cases. For the SS potential a is always smaller than the range R_0 and we fix the height V_0 such that $a = R_0/2$. In the case of the SW potential instead, the scattering length diverges to $\pm\infty$ every time a new bound state enters the well: we fix the range such that $nR_0^3 = 10^{-6}$ in terms of the particle density n and the depth V_0 takes values corresponding to the positive branch of a with a single bound state. The short-range SW potential provides a realistic description of interatomic forces in ultracold atoms.

In the case of purely repulsive interactions we use the fixed-node diffusion Monte Carlo (FN-DMC) method (see Sec. 2.6). This variational method yields an upper bound for the ground-state energy of the gas, sampling the lowest-energy wave function whose many-body nodal surface is the same as that of a trial wave function ψ_T. FN-DMC can give the exact ground-state energy, provided one knows the exact nodal surface, and in general the energies have been found to be highly accurate even if nodes are only approximate (for more details see *e.g.* [Rey82]). Our trial wave function is of the Jastrow-Slater form

$$\psi_T(\mathbf{R}) = \prod_{i,i'} f(r_{ii'})D_\uparrow(N_\uparrow)D_\downarrow(N_\downarrow)\ , \tag{3.2}$$

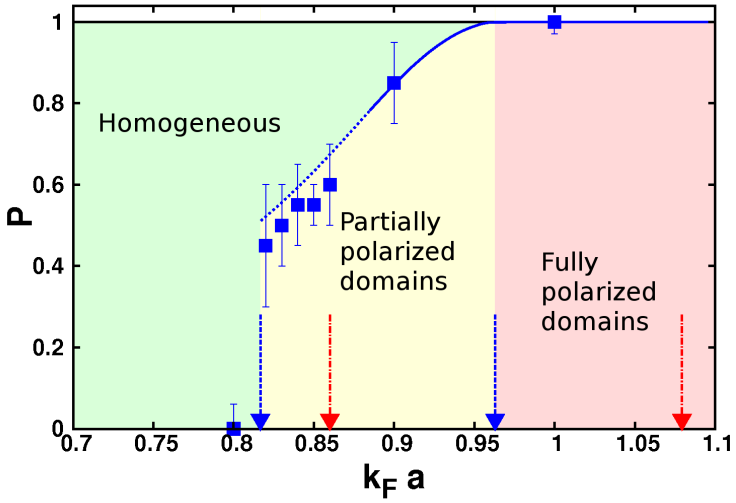

Figure 3.1: Phase diagram of the HS gas in the interaction/polarization plane. The green region corresponds to the homogeneous phase. The other regions correspond to phase separated states with partially polarized domains (yellow) and fully ferromagnetic domains (pink). The (blue) symbols correspond to the minimum of the curve $E(P)$ and the solid/dashed line is the phase boundary determined from the equilibrium condition for pressure and chemical potentials. The blue and red arrows indicate the critical densities where χ diverges and full ferromagnetism sets in, respectively for the HS and SW potential.

where $\mathbf{R} = (\mathbf{r}_1, ..., \mathbf{r}_N)$ is the spatial configuration vector of the N particles and $D_{\uparrow(\downarrow)}$ denotes the Slater determinant of plane waves in a cubic box of size L with periodic boundary conditions, accommodating the $N_{\uparrow(\downarrow)}$ particles with up (down) spin. The Jastrow correlation term $f(r)$ is obtained from the solution of the two-body scattering problem with the potential $V(r)$, satisfying the boundary condition on its derivative $f'(r = L/2) = 0$. Since $f(r) > 0$, the many-body nodal surface results only from the antisymmetric character of ψ_T and coincides with that of a non interacting gas, thus correctly reproducing this limit. Another advantage is that the trial function (3.2) can be used to simulate both unpolarized ($N_\uparrow = N_\downarrow$) and polarized ($N_\uparrow > N_\downarrow$) configurations.

Attractive interactions, as modeled by the SW potential, are more delicate, because of the presence of bound states (molecules) in the true ground state. The atomic Fermi gas of interest here is a meta-stable state consisting of unbound fermionic atoms and no dimers or other bound molecules. Since we are interested in a metastable excited state we cannot use the FN-DMC method and resort to the variational Monte Carlo (VMC) calculation that provides a stable estimate of the energy $E_{\mathrm{VMC}} = \langle\psi_T|H|\psi_T\rangle/\langle\psi_T|\psi_T\rangle$ (see Sec. 2.3). The absence of molecular bound states can be readily im-

plemented for two particles by choosing the Jastrow correlation term $f(r)$ to be the scattering solution of the SW potential corresponding to positive energy, which by construction is orthogonal to the bound molecule. A many-body wave function is then constructed using Eq. (3.2) with this choice of $f(r)$, while $f'(r = L/2) = 0$ takes care of periodic boundary conditions similarly to the purely repulsive case. For small scattering energies, corresponding to large values of L, the Jastrow term f changes sign at $r = a$. The larger the size of the simulation box the smaller is the overlap between f and the bound-state wave function, and ψ_T provides an accurate description of the gas-like state in the very dilute regime, but in general exhibits a non-zero overlap with the state where dimers are formed. The overlap with states where three or more-body bound states are formed is suppressed if the range R_0 of the SW potential is small enough.

It is important to note that the repulsive HS and SS potential and the attractive SW potential, even though they correspond to the same value of a and consequently share a similar long-range behavior of the correlation functions, exhibit completely different short-range correlations as explicitly shown in the inset of Fig. 3.2 where we report results on the anti-parallel spin pair correlation function.

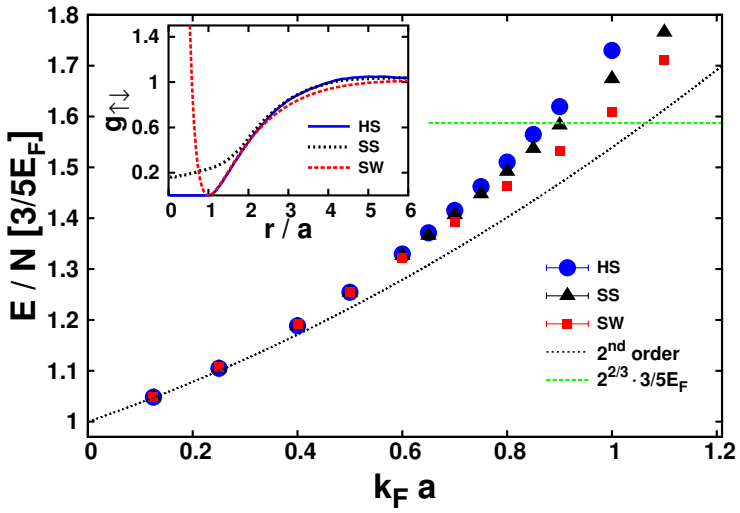

Figure 3.2: Equation of state of the unpolarized gas. We show FN-DMC results for the repulsive HS and SS potentials and VMC results for the attractive SW potential. VMC results for the HS gas are also shown for comparison. The perturbation expansion Eq. (3.3) is shown with the (black) dashed line, while the (green) horizontal line corresponds to the energy of the fully ferromagnetic state. Inset: Pair correlation function $g_{\uparrow\downarrow}(r)$ at $k_F a = 0.5$. The range of the SS and SW potential is respectively $R_0 = 2a$ and $R_0 = 0.06a$. The minimum at $r = a$ for the SW potential corresponds to the node in the Jastrow correlation term $f(r)$. VMC and DMC results of $g_{\uparrow\downarrow}(r)$ practically coincide for the HS and SS potential.

Simulations are performed with a maximum number of atoms in a single spin component $N_{\uparrow(\downarrow)} = 33$, corresponding to a closed shell in momentum space. For most results we checked the influence of finite-size effects by repeating the calculations with $N_{\uparrow(\downarrow)} = 81$. For the results of the SW potential, no appreciable change is found by reducing the potential range parameter nR_0^3.

The equation of state of the balanced, $N_\uparrow = N_\downarrow$, gas of weakly repulsive fermions was calculated using perturbation theory to second order in a [HY57, LY57]:

$$\frac{E}{N} = \frac{3}{5}E_F\left[1 + \frac{10}{9\pi}k_F a + \frac{4(11-2\log 2)}{21\pi^2}(k_F a)^2\right] , \tag{3.3}$$

where $E_F = \hbar^2 k_F^2/2m$ is the Fermi energy. One should notice that higher order terms in the above equation will depend not only on the scattering length a, but also on other details of the interatomic potential. As can be seen in Fig. 3.2. agreement between the QMC results and Eq. (3.3) is found for $k_F a \lesssim 0.4$, but significant deviations and a gradual loss of universality become evident for larger values of the interaction strength. In the figure we also show the energy of the fully ferromagnetic (FF) state $E_{\rm FF} = 3/5E_F 2^{2/3}(N_\uparrow + N_\downarrow)$ consisting of two spatially separated regions of non-interacting spin-up and spin-down fermions. Any uniform mixture of the two spin species whose energy exceeds the value $E_{\rm FF}$ is clearly unstable against phase separation.

In order to better characterize the critical behavior at the onset of ferromagnetic behavior, we calculate the equation of state of the gas as a function of the system polarization $P = (N_\uparrow - N_\downarrow)/(N_\uparrow + N_\downarrow)$ and then show that for $P \lesssim 1$ it can be well described in terms of weakly interacting polarons. Results for the HS potential are shown in Fig. 3.3. An analogous study is performed using the SW potential (not shown). Finite size effects are reduced by subtracting from the QMC results, the finite size corrections to the ground state energy $E_0(N_\uparrow, N_\downarrow) - E_0^{\rm TL}(P)$ of non-interacting fermions with the same number of particles and the same polarization P (TL refers here to the thermodynamic limit). The validity of this method, that relies on Fermi liquid theory, is discussed in Ref. [LZC01] where it is compared with twist-averaged boundary conditions (see also Sec. 2.9).

3.3 Results

From the results at small polarization we extract the inverse magnetic susceptibility $1/\chi$ using a quadratic fit: $E(P) = E(P=0) + NE_F\frac{\chi_0}{\chi}\frac{P^2}{3}$, where $\chi_0 = 3n/2E_F$ is the susceptibility of the non-interacting gas. The results for both the HS and SW potential are shown in the inset of Fig. 3.4. For $k_F a > 0.6$ we find a linear decrease of the inverse magnetic susceptibility

with increasing interaction strength, showing that χ diverges at the critical densities $k_F a \simeq 0.82$ and $k_F a \simeq 0.86$, respectively for the HS and the SW potential. As seen in Fig. 3.3 a minimum in $E(P)$ at finite polarization $\bar{P}$ appears when $k_F a > 0.82$. This minimum corresponds to a thermodynamically stable mixed state with partially polarized domains (see Fig. 3.1). For $P < \bar{P}$ the system follows the coexistence line where, in the thermodynamic limit, $E(P)$ is the sum of energies of domains with polarization $\bar{P}$ and $-\bar{P}$ whose relative volume changes with P. For $P > \bar{P}$, on the other hand, a uniform mixture of spin components can still survive.

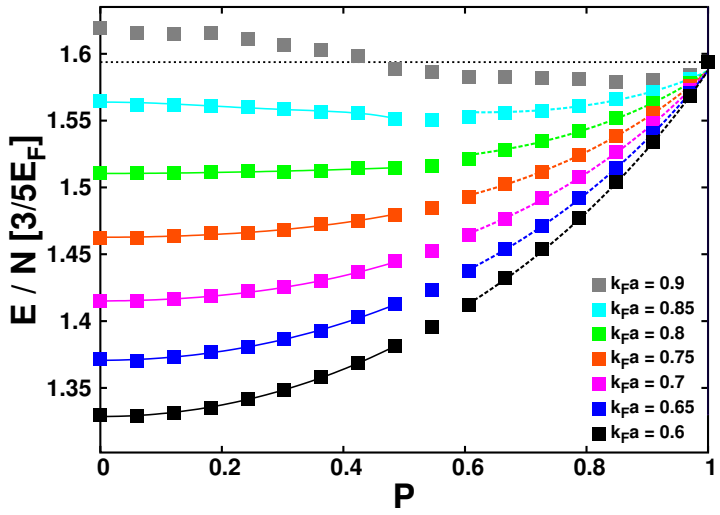

Figure 3.3: Energy of the HS gas as a function of polarization for different values of $k_F a$. The symbols correspond to FN-DMC results, while the lines at small and large P correspond, respectively, to the fitted quadratic law and polaron energy functional of Eq. (3.4). The horizontal dotted line is the threshold energy E_{FF} of the fully ferromagnetic state.

For large values of P the QMC results are well fitted by the energy functional of weakly interacting polarons

$$E(x) = \frac{3}{5} N_\uparrow E_{F\uparrow} \left(1 + Ax + \frac{m}{m^*} x^{5/3} + Fx^2\right) , \tag{3.4}$$

which results from an expansion in the small concentration $x = N_\downarrow / N_\uparrow$ of spin-down impurities in a Fermi sea of spin-up particles. Here $E_{F\uparrow} = \hbar^2 k_{F\uparrow}^2 / 2m$ is the Fermi energy of the spin-up particles in terms of the corresponding wave vector $k_{F\uparrow} = (6\pi^2 n_\uparrow)^{1/3}$. Furthermore, the quantities A, m^* and F, which are all functions of $k_{F\uparrow} a$, denote respectively the chemical potential at zero concentration, the effective mass and the interaction parameter of the polaronic quasiparticles (see Ref. [LRGS06] for the similar treatment of attractive polarons).

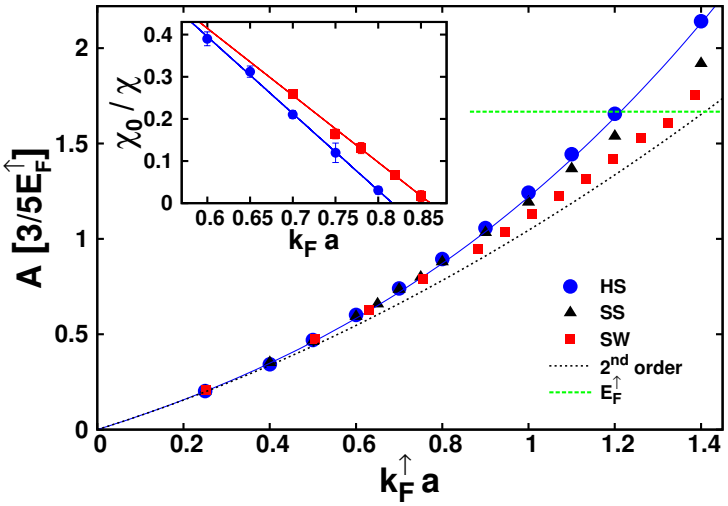

Figure 3.4: Chemical potential at zero concentration of the repulsive polaron. We show FN-DMC results for the repulsive HS and SS potentials and VMC results for the attractive SW potential. VMC results for the HS gas are also shown for comparison. The (blue) solid line is a fit to the HS results. The second-order perturbation expansion is shown with the (black) dashed line, while the (green) horizontal line corresponds to $E_{F\uparrow}$. Inset: Inverse magnetic susceptibility $1/\chi$ for the HS (blue circles) and SW (red squares) potential. The lines are linear fits to the data.

The results for A as a function of the interaction strength are shown in Fig. 3.4. The weak coupling result $A = \frac{5}{3}[4k_{F\uparrow}a/3\pi + 2(k_{F\uparrow}a)^2/\pi^2]$, calculated to second order in the scattering length [MC10, CZ10], is also shown (A. Recati, private communication). This quantity is important in order to understand the stability of the fully ferromagnetic phase: in fact, if $A < E_{F\uparrow}$, the fully polarized domain is unstable against mixing of spin-up and spin-down particles resulting in a partially polarized state. This problem was investigated using a single particle-hole wave function in Ref. [CZ10]. We estimate that the FF state becomes unstable at $k_{F\uparrow}a = 1.2$ and $k_{F\uparrow}a = 1.4$, respectively for the HS and SW potential. By imposing pressure and chemical potential equilibrium between highly polarized states described by the energy functional (3.4), we determine the critical polarization boundaries, shown in the phase diagram of Fig. 3.1, separating the homogeneous unbalanced mixture from the partially ferromagnetic state comprised of domains with opposite critical polarization $\pm\bar{P}$. This determination of the phase boundaries is reliable at large total polarization P, where the energy functional (3.4) is valid, but becomes less accurate at intermediate values of P (dashed line in Fig. 3.1) and can not be applied at small polarization.

Good agreement is found with the critical polarization as determined from the minimum of the $E(P)$ curve. The critical polarization has a sharp drop to $P = 0$ close to the density where χ diverges, not allowing for a clear distinction of the order of the phase transition. The possible emergence of new phases, such as the spin textured phase proposed in Ref. [CGS09], also requires more detailed investigations.

3.4 Conclusion

In conclusion we calculate the equation of state of a repulsive gas of fermions as a function of interaction strength and spin polarization. We determine the critical density for the onset of ferromagnetic behavior and we investigate the stability of the fully ferromagnetic state. While the qualitative features of the phase diagram are well described by just the long-range repulsive correlations induced by the positive s-wave scattering length, the quantitative determination of the phase boundaries depends on the details of the interaction potential.

We acknowledge discussions with A. Recati. This work was supported by the Swiss National Science Foundation and by a grant from the Army Research Office with funding from the DARPA OLE program. As part of the European Science Foundation EUROCORES Program "EuroQUAM-FerMix" it was supported by funds from the CNR and the EC Sixth Framework Programmer.

A related work appeared [CRT10], with similar results as ours.

Chapter 4

BCS-BEC crossover in a $2D$ Fermi gas

In this Chapter we apply the DMC technique to the problem of the crossover from Bardeen-Cooper-Schrieffer superfluidity to Bose Einstein condensation in a Fermi gas with purely attractive interactions in two dimensions. We show the analogies and the differences with respect to the three dimensional case. Due to the confined geometry, the role of two-body physics is much increased. Many different experimental groups are going to study this kind of problem in the context of ultracold gases. This Chapter shares the main results with the preprint [BG10].

4.1 Introduction

Ultracold atomic Fermi gases have become an active and rich field of research [GPS08]. Important areas of investigation include the BCS-BEC crossover in a superfluid gas with resonantly enhanced interactions, the Chandrasekhar-Clogston instability of the superfluid state when spin polarization is increased, the possible onset of itinerant ferromagnetism in a gas with repulsive interactions [JLC$^+$09] and the realization of the Hubbard model for fermions loaded in optical lattices [BDZ08].

Low dimensional configurations of degenerate Fermi gases have also been the object of experimental and theoretical studies [GPS08, BDZ08]. In particular, a two-dimensional (2D) ultracold Fermi gas has been recently realized using a highly anisotropic pancake-shaped potential and the density profile of the cloud has been measured using *in situ* imaging [MMT10]. On the theoretical side, the evolution from a superfluid state with large Cooper pairs to one with tight molecules in a 2D system of attractive fermions was first investigated by Miyake [Miy83] and later by Randeria and coworkers [RDS89, RDS90] aiming to describe high-T_c superconductors. More recent studies address the problem of the superfluid transi-

tion [PBS03, ZLD08b], of harmonic trapping [ZLD08a, MT05] and of population and mass imbalance [CCS08, HZ08]. These studies are in general based on perturbative or mean-field approaches that are suitable in the regime of weak coupling, but are bound to break down when interactions become stronger.

In this Chapter we provide the first determination using quantum Monte Carlo methods of the equation of state at $T = 0$ of a homogeneous 2D Fermi gas in the BCS-BEC crossover. We also obtain results for the pairing gap and the contact parameter as a function of the interaction strength. In the strong coupling regime all quantities exhibit large deviations compared to mean-field predictions. A similar study carried out in 3D [ABCG04] has provided an important benchmark against which experimental determination of the equation of state, using measurements of the dispersion of collective modes [ARK$^+$07] or of *in situ* density profiles [NNCS10], have been successfully compared. Hopefully, the results reported in this work will stimulate more experimental efforts towards the realization of a 2D Fermi gas in the strong-coupling regime by means, for example, of a Feshbach resonance to increase the interaction parameter [MMT10]. In Sec. 4.2 we will introduce the microscopic model, starting from the two-body physics. In Sec. 4.3 we will review the mean-field and perturbative results for the many-body problem, both for the weakly interacting limit and the strongly interacting one. In Sec. 4.4 we will discuss the QMC method we used and in Sec. 4.5 we will show our results, comparing them to the mean-field solution.

4.2 Model hamiltonian and two-body physics

We consider a homogeneous two-component Fermi gas described by the Hamiltonian

$$H = -\frac{\hbar^2}{2m}\left(\sum_{i=1}^{N_\uparrow}\nabla_i^2 + \sum_{i'=1}^{N_\downarrow}\nabla_{i'}^2\right) + \sum_{i,i'}V(r_{ii'})\,, \tag{4.1}$$

where m denotes the mass of the particles, $i, j, ...$ and $i', j', ...$ label, respectively, spin-up and spin-down particles and $N_\uparrow = N_\downarrow = N/2$, N being the total number of atoms. We model the interspecies interatomic interactions using an attractive square-well (SW) potential: $V(r) = -V_0$ for $r < R$ ($V_0 > 0$), and $V(r) = 0$ otherwise. In order to ensure that the mean interparticle distance is much larger than the range of the potential we use $nR^2 = 10^{-6}$, where n is the gas number density, or equivalently $k_F R = 0.0025$ in terms of the Fermi wave vector $k_F = \sqrt{2\pi n}$. In such a regime there is a negligible dependence of the observables on the range of the interaction, so that the SW potential can be considered universal.

We simulate a system that is strictly 2D, so we will now introduce some quantities related to scattering in two dimensions, in particular the scat-

tering length. In two dimensions the s-wave phase shift of the two-body problem scales as the logarithm of the total energy when energy goes to zero; actually it has the following asymptotic behavior:

$$\pi \cot \delta_0(\varepsilon) = \log\left(\frac{\varepsilon}{E_a}\right) + O\left(\frac{\varepsilon}{\epsilon_R}\right), \tag{4.2}$$

where $\epsilon_R = \hbar^2/mR^2$, $E_a = 4\hbar^2/(me^{2\gamma}a_{2D}^2)$, and $\gamma \simeq 0.577$ is Euler - Mascheroni's constant. E_a is a typical energy scale. Note that Eq. (4.2) and the definition of E_a unambiguously fix the value of the scattering length, once one includes all the constant terms into the logarithm of Eq. (4.2). Another definition of $a_{2\mathrm{D}}$ includes the factor $e^{\gamma}/2$, such that $E_a = \hbar^2/m\tilde{a}_{2\mathrm{D}}^2$. In the case of the SW potential one has

$$a_{2\mathrm{D}} = R\, e^{J_0(\kappa)/\kappa J_1(\kappa)}\,, \tag{4.3}$$

where $J_{0(1)}(x)$ are Bessel functions of the first kind and $\kappa = \sqrt{V_0/\epsilon_R}$. This definition of $a_{2\mathrm{D}}$ gives $a_{2\mathrm{D}} \leq R$ for a repulsive soft-disk potential (κ pure imaginary), the equality $a_{2\mathrm{D}} = R$ being reached for hard disks of diameter R. The scattering length (4.3) is non negative and diverges at $\kappa = 0$ and at the zeros of J_1, corresponding to the appearance of new two-body bound states in the well. Close to these points the shallow dimers have size $a_{2\mathrm{D}}$ and their binding energy is given by $\varepsilon_b = -E_a$. The dependence of $a_{2\mathrm{D}}$ as a function of the depth V_0 in the region where the well supports only one bound state is shown in the inset of Fig. 4.1.

Compared to the 3D case the BCS-BEC crossover in 2D exhibits important differences, mainly coming from different scattering properties:

- For a purely attractive potential a two-body bound state exists for arbitrarily weak attractions, while in $3D$ one needs a strong enough potential depth. This implies that the length $a_{2\mathrm{D}}$ diverges for a vanishingly small attraction.
- The 2D scattering amplitude of particles colliding at low energy $\varepsilon = \hbar^2k^2/m$ is given by $f(k) = 2\pi/[\log(2/ka_{2\mathrm{D}}e^{\gamma}) + i\pi/2]$ [PS01] and goes to zero for $k \to 0$, while in $3D$ one has $f(k) = 1/[-1/a_{3D} - ik]$, which goes to the constant $-a_{3D}$ for $k \to 0$.
- There is no finite value of the interaction potential strength for which $f(k)$ is independent of the scattering length. On the contrary in $3D$ it is possible to have $f(k) = 4\pi/ik$ at the threshold for the appearance of the first bound state (unitary limit).

4.3 Many-body problem

In two-dimensions the energy per particle in the non-interacting case is

$$E_{\mathrm{FG}} = \frac{1}{2}\frac{\hbar^2k_F^2}{2m} = \frac{1}{2}\varepsilon_F\,, \tag{4.4}$$

where ε_F is the Fermi energy.

Two regions are clearly identified by comparing $a_{2\mathrm{D}}$ with the mean interparticle distance $1/k_F$: i) $k_F a_{2\mathrm{D}} \gg 1$ corresponds to the BCS regime where interactions are weak and dimers are large and weakly bound, ii) $k_F a_{2\mathrm{D}} \ll 1$ corresponds instead to the BEC regime of tightly bound composite bosons. The region $k_F a_{2\mathrm{D}} \sim 1$ identifies the strong-coupling crossover region between the BCS and the BEC regime (see inset of Fig. 4.1).

4.3.1 BCS self-consistent theory

The mean-field BCS equations can be analytically solved [Miy83, RDS90] along the BCS-BEC crossover, in terms of the interaction coefficient $x = |\varepsilon_b|/2\varepsilon_F$. For the BCS order parameters one obtains $\Delta = 2\varepsilon_F\sqrt{x}$, while for the energy per particle one obtains $E/N = E_{FG}(1-2x)$ and for the chemical potential $\mu = \varepsilon_F(1-x)$. The interpretation is clear: for small binding energy one recovers the non interacting limit; when $x \approx 1$, the chemical potential becomes zero and then negative, so that the role of the dimers becomes more important; for very strong binding the chemical potential of the fermions is equivalent to half the binding energy of a molecule, so the system is made of non interacting bosons.

Although very useful for providing a global self-consistent picture and for setting a stringent variational upper bound to the energy per particle, the BCS solution fails in various aspects. In the BCS regime it neglects the Hartree-Fock contributions to energy, which are dominant, since the gap is small. In the BEC regime it misses the correct interaction energy between the bosons. In general it is not able to reproduce the logarithmic dependence of energy on the density, which is typical of 2D.

4.3.2 Perturbative results in the BCS limit

In the weak coupling regime when the gap is small, a perturbative calculation starting from the non-interacting Fermi sphere, which is equivalent to a normal Fermi liquid approach, is able to provide a better estimate of the energy that the BCS theory. When the many-body problem is approached, it is possible to introduce a mean-field coupling constant by considering the scattering amplitude, provided the energy is small with respect to the scale $E_a = |\varepsilon_b|$. This causes an intrinsic ambiguity in two dimensions, since one has to choose a reference energy to fix the coupling constant. Usually for Fermi systems, when there is a definite Fermi surface, one puts $\varepsilon = 2\mu = 2\varepsilon_F$, so that the mean-field coupling constant can be written as $g = (4\pi\hbar^2/m)/\log(E_a/2\varepsilon_F)$ with logarithmic accuracy. Note that this coupling constant becomes meaningless in the crossover region.

The equation of state of a Fermi gas with short range repulsive interaction in two dimensions has first been studied by Bloom using perturbative

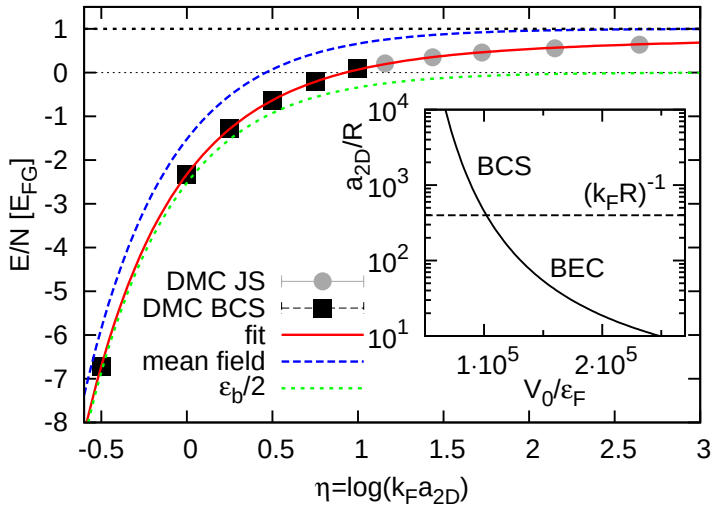

Figure 4.1: Equation of state in the BCS-BEC crossover. Squares refer to the BCS and circles to the JS wave function. The solid (red) line is a fit to the data, the dotted (green) line is half of the molecular binding energy and the dashed (blue) line is the prediction of mean-field theory. The horizontal dotted (black) line denotes the energy per particle E_{FG} of the non-interacting gas. Inset: 2D scattering length $a_{2\mathrm{D}}$ as a function of the depth V_0 for a SW potential of radius R. The BCS and BEC regimes correspond, respectively, to $k_F a_{2\mathrm{D}} \gg 1$ and $k_F a_{2\mathrm{D}} \ll 1$.

theory [Blo75] and then by Randeria and coworkers in a series of subsequent papers [ER92, ERZ92], using diagrammatic techniques in the framework of Fermi Liquid Theory. Beyond logarithmic accuracy Bloom found the expansion $E/N = E_{FG}(1 - 1/\eta + 0.28/\eta^2)$ in the interaction parameter $\eta = \log(k_F a_{2D})$, while Randeria found $E/N = E_{\mathrm{FG}}\left(1 + 2g + (3 - 4\log 2)g^2\right)$ in terms of the previously introduced coupling constant. These two expressions coincide up to the first logarithmic order. We remark here however that the E_a introduced by Randeria has a factor 2 of difference with that introduced by us; this affects the definition of g, so that the validity of the second order coefficient is questionable.

4.3.3 Perturbative results in the BEC limit

The equation of state of a two dimensional Bose gas with short range interaction has been calculated within quantum field theory in [Bea10]. Previously it was widely studied both analytically and with QMC techniques (see [ABC+09, MC09] and references therein).

Following Beane we introduce the running coupling $g_B(\lambda)$ in terms of the scattering length of the bosons a_B and the particle density of the bosons

n_B:

$$g_B(\lambda) = -\frac{1}{\log\left(n_B \lambda \pi^2 e^{2\gamma} a_B^2\right)} , \tag{4.5}$$

where λ is an arbitrary dimensionless cutoff parameter, which is present due to the truncation in the perturbative expansion. In the following m_B is the mass of the bosons.

Up to the second order in the running coupling, one can express the energy density in the following way

$$\mathcal{E} = \frac{2\pi\hbar^2 n_B^2}{m_B} g_B(\lambda)\left[1 + g_B(\lambda)\Big(\log\left(\pi g_B(\lambda)\right) - \log\lambda\pi^2 + \frac{1}{2}\Big)\right]. \tag{4.6}$$

It is evident from the above expression that fixing the scattering length a_B which appears in the definition of $g_B(\lambda)$ is not sufficient for determining the energy density if one does not declare its choice for λ, that is the form of the coupling constant. Note also that the coefficient of the second order term does depend on the choice of λ. A convenient choice for simplifying the expression is to set $\lambda = e^{-2\gamma}/\pi^2$, so that we can introduce the coupling $g_B = -1/\log\left(n_B a_B^2\right)$ and we obtain

$$\mathcal{E} = \frac{2\pi\hbar^2 n_B^2}{m_B} g_B\left[1 + g_B\Big(\log\left(\pi g_B\right) + 2\gamma + \frac{1}{2}\Big)\right]. \tag{4.7}$$

Now let us consider the case when the bosons are dimers, consisting of two paired fermions with mass $m = m_B/2$ and particle density $n = 2n_B$. There must exist a regime where the binding is so tight that the EOS of such composite bosons is the same as in the case of point-like bosons, with the simple replacement $a_B \to \alpha a_{2D}$, where a_{2D} is the scattering length of the underlying fermions. Let us therefore introduce the dimensionless coupling parameter of the fermions as $\eta = \log\left(k_F a_{2D}\right)$, where $n = k_F^2/2\pi$, so that the composite bosons coupling turns to be $g_B = -1/\log\left(n\alpha^2 a_{2D}^2/2\right) = 1/(\log 4\pi - 2\eta - 2\log\alpha)$. In such a situation the energy per fermion can be written in the following way:

$$\frac{E}{N_F} = -\frac{|\varepsilon_b|}{2} + \frac{\varepsilon_F}{2}\frac{1}{2} g_B\left[1 + g_B\Big(\log\left(\pi g_B\right) + 2\gamma + \frac{1}{2}\Big)\right], \tag{4.8}$$

where $-|\varepsilon_b|/2$ is the contribution from the binding energy of the dimers.

Note that Petrov and coworkers [PBS03] introduced a different definition of the coupling constant for the composite bosons, implying a different choice of λ. Namely the coupling constant (with dimension $Energy \times Area$) proposed by Petrov was:

$$g_m = \frac{2\pi\hbar^2}{m}\frac{1}{\log\left(\frac{2\beta^2\epsilon_b}{e^{2\gamma}\epsilon}\right)}, \tag{4.9}$$

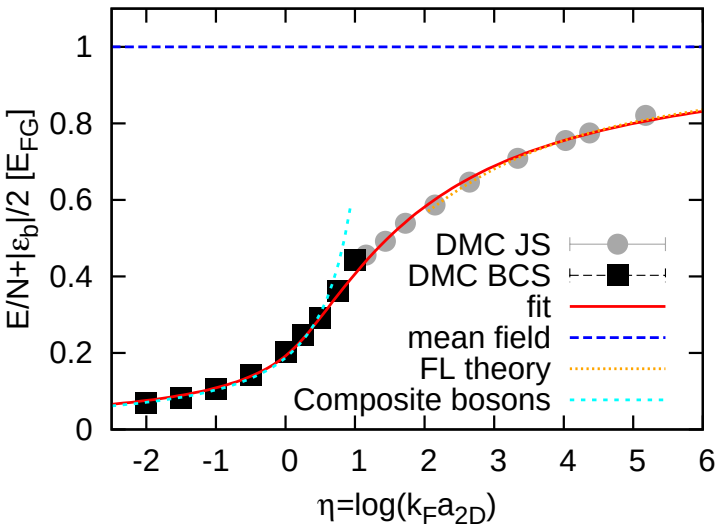

Figure 4.2: Equation of state in the BCS-BEC crossover with $\varepsilon_b/2$ subtracted from E/N. Symbols are as in Fig.4.1. The solid (red) line is a fit to the data, the other dotted lines denote the equation of state (4.11) of composite bosons and the perturbation expansion (4.12) holding in the BCS regime. The dashed (blue) line shows the result of mean-field theory.

where $\beta = 1.6$ from four-body calculations and ϵ is a reference energy of the order $\epsilon \approx 2g_m n_b \approx \frac{4\pi\hbar^2 n_B}{m}$, that is twice the chemical potential of a single boson neglecting the logarithm. In the above formula the binding energy of the dimer corresponds to $\epsilon_b = \frac{\hbar^2}{2ma_F^2}\frac{8}{e^{2\gamma}}$, but one can introduce the reference energy for two dimers as $E_b = \frac{\hbar^2}{2m_b}\frac{8}{a_B^2 e^{2\gamma}}$, which defines the scattering length for the dimers as $a_B = a_{2D}e^{\gamma}/2\beta$, once one puts $g_m = \frac{2\pi\hbar^2}{m}\frac{1}{\log(E_b/\epsilon)}$. The proportionality factor between the scattering lengths of the fermions and the bosons corresponds to $\alpha_P = e^{\gamma}/2\beta \approx 0.56$. The argument of the logarithm turns out to be $1/n_B a_B^2 2\pi e^{2\gamma}$, while with our choice of $\lambda = \lambda_C = \frac{1}{\pi^2 e^{2\gamma}}$ one would have $1/n_B a_B^2$. This implies that in their case $\lambda = \lambda_P = 2/\pi$, so that the corresponding expression for the energy per particle, up to second order, turns to be

$$\frac{E}{N_F} = -\frac{|\varepsilon_b|}{2} + \frac{\epsilon_F}{2}\frac{1}{2}g_B^P\left[1 + g_B^P\left(\log\left(g_B^P\right) - \log(2) + \frac{1}{2}\right)\right], \tag{4.10}$$

where $g_B^P = 1/(\log 2 - 2\gamma - 2\eta - 2\log\alpha_P)$. As will be shown in the following, we validate the value of the dimer scattering length provided by Petrov and coworkers, even if we obtain that retaining the second order term in the energy functional is crucial for a correct interpretation.

4.4 Method

Simulations are carried out in a square box of area $L^2 = N/n$ with periodic boundary conditions, using the fixed-node diffusion Monte Carlo (FN-DMC) method. This numerical technique yields an upper bound for the ground-state energy of the gas resulting from an ansatz for the nodal surface of the many-body wave function that is kept fixed during the calculation (see Chap. 2 for more details). The boundary condition is enforced using a trial function that we choose of the general form [CPCS04, ABCG05] $\psi_T(\mathbf{R}) = \Phi_S(\mathbf{R})\Phi_A(\mathbf{R})$, where Φ_S is a positive function of the particle coordinates $\mathbf{R} = (\mathbf{r}_1, ..., \mathbf{r}_N)$ and is symmetric in the exchange of particles with equal spin, while Φ_A satisfies the fermionic antisymmetry condition and determines the nodal surface of ψ_T. The symmetric part is chosen of the Jastrow form $\Phi_S(\mathbf{R}) = \prod_{i,i'} f_{\uparrow\downarrow}(r_{ii'})$, where two-body correlation functions of the interparticle distance have been introduced for antiparallel spins. The Φ_A component is chosen as an antisymmetrized product $\Phi_A(\mathbf{R}) = \mathcal{A}\left(\phi(r_{11'})\phi(r_{22'})...\phi(r_{N_\uparrow N_\downarrow})\right)$ of pair-wise orbitals of the form $\phi(r) = \beta_p \sum_{k_\alpha \leq k_F} e^{i\mathbf{k}_\alpha \cdot \mathbf{r}} + \beta_s \varphi_s(r)$, with $\beta_p^2 + \beta_s^2 = 1$. Here, $\mathbf{k}_\alpha = 2\pi/L(\ell_{\alpha x}\hat{x} + \ell_{\alpha y}\hat{y})$ indicate the plane wave states in the box, with integers ℓ's summed up to the maximum value of the k-shell accommodating $N/2$ particles, and β_p is a variational parameter controlling the relative weight of the plane-wave sum to the spherical symmetric component $\varphi(r)$.

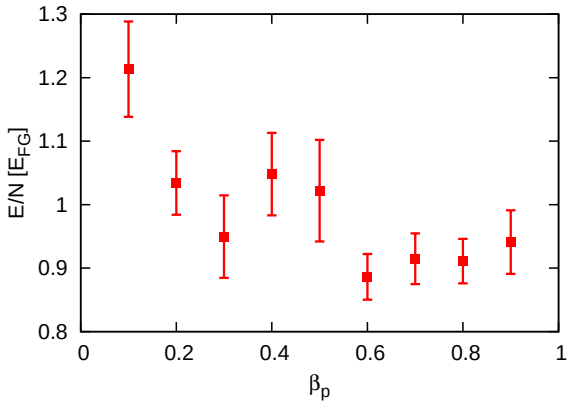

Figure 4.3: Optimization of the parameter β_p at $\eta = \log(k_F a_{2D}) = 2.64$, with VMC. The optimal value is chosen to be $\beta_p = 0.6$. A similar optimization was performed for points in the range $0.5 < \eta < 4$ and the resulting pair orbitals were used for DMC simulations. In all the cases, due to large error bars, the obtained energies were not better than those obtained with the $\beta_p = 0$ or $\beta_p = 1$ pair orbitals, which we therefore report in Tab. 4.1.

Two important regimes are described by the above trial wave function:

i) if $f_{\uparrow\downarrow} = 1$, $\beta_p = 0$ and $\varphi_s(r) = f_b(r)$ is the molecular solution of the two-body problem with the potential $V(r)$, the wave function $\psi_T(\mathbf{R})$ describes a BCS state of bound molecules that is expected to be appropriate in the deep BEC regime; ii) if instead $\beta_p = 1$ and $f_{\uparrow\downarrow}(r) = f_b(r)$, the antisymmetric component in the trial function coincides with the product of the plane-wave Slater determinants for spin-up and spin-down particles $\Phi_A(\mathbf{R}) = D_\uparrow(N_\uparrow)D_\downarrow(N_\downarrow)$ [BGL88] and ψ_T is a typical Jastrow-Slater function of a normal Fermi liquid. This description is expected to hold in the BCS regime of a weakly interacting gas where the effect of pairing on the ground-state energy is negligible. The more general form of the trial wave function written above provides a smooth interpolation between these two regimes (see Fig. 4.3 for more details). Note that all radially symmetric two-body functions have zero derivative at $r = L/2$, to be consistent with periodic boundary conditions.

4.5 Results

In Figs. 4.1-4.2 and in Tab. 4.1 we report the FN-DMC results for the equation of state as a function of the interaction parameter in units of the energy per particle of the non interacting gas E_{FG}. Calculations are carried out using ψ_T of the BCS and JS form as described above. The BCS function provides a lower energy for $\log(k_F a_{2D}) \lesssim 1$, while the JS function is more favorable for larger values of the interaction parameter. More sophisticated forms of ψ_T, interpolating between the BCS and JS function, have been used in the region $\log(k_F a_{2D}) \sim 1$, but without a significant improvement of the ground-state energy (see Fig. 4.3). The role of finite-size effects has been investigated by carrying out calculations with $N = 26$ and $N = 98$. No significant change is seen when using the BCS trial function and for the JS function a large suppression of these effects is obtained by compensating for the finite-size correction of noninteracting fermions with the same number of particles (see Sec.2.9).

The result $E/N = E_{\rm FG} + \varepsilon_b/2$ obtained from mean-field theory [Miy83, RDS89, RDS90] is shown in Figs. 4.1-4.2 for comparison. The inadequacy of the mean-field approach is best shown in Fig. 4.2, where the molecular contribution is subtracted from the energy per particle. In the BEC regime the FN-DMC results are fitted with the equation of state of a gas of composite bosons corresponding to hard disks of diameter a_d

$$\frac{E}{N_d} + |\varepsilon_b| = \frac{2\pi\hbar^2 n_d}{m_d}\frac{1}{\log(1/n_d a_d^2)}\left[1 - \frac{\log\log(1/n_d a_d^2)}{\log(1/n_d a_d^2)} + \frac{\log\pi + 2\gamma + 1/2}{\log(1/n_d a_d^2)}\right], \quad (4.11)$$

where $m_d = 2m$ is the mass of the dimer, while the number of dimers, and

Table 4.1: Energy per particle and molecular binding energy in the BEC-BCS crossover (energies are in units of $E_{\rm FG}$).

$\log(k_F a_{\rm 2D})$	E/N	$\varepsilon_b/2$	$E/N - \varepsilon_b/2$
-2.00	-137.761(7)	-137.832	0.070(7)
-1.50	-50.593(4)	-50.675	0.082(4)
-1.00	-18.532(4)	-18.637	0.105(4)
-0.50	-6.714(4)	-6.856	0.142(4)
0.00	-2.318(2)	-2.522	0.204(2)
0.25	-1.283(12)	-1.530	0.247(12)
0.50	-0.638(10)	-0.928	0.290(10)
0.75	-0.201(12)	-0.563	0.361(12)
1.44	0.349(6)	-0.143	0.492(6)
1.72	0.459(16)	-0.080	0.539(16)
2.15	0.552(2)	-0.034	0.587(2)
2.64	0.634(4)	-0.013	0.647(4)
3.34	0.706(2)	-0.003	0.709(2)
4.03	0.755(4)	0.000	0.755(4)
4.37	0.775(1)	0.000	0.775(1)
5.18	0.821(7)	0.000	0.821(7)

correspondingly their density n_d, is half of the total number of fermions $N_d = N/2$. The above expression, which is equivalent to Eq. (4.8), includes beyond mean-field terms [ABC$^+$09, MC09, Bea10] and allows for a precise determination of the dimer-dimer scattering length a_d. We obtain $a_d = 0.55(4)a_{2D}$, in agreement with the four-body calculation in Ref. [PBS03] (see Sec. 4.3.3).

In the opposite BCS regime, where the contribution of the pairing gap can be neglected, the fermionic equation of state can be described in terms of an attractive normal Fermi liquid (FL), as we mentioned in Sec. 4.3.2. If we set the beyond logarithmic accuracy expression

$$\frac{E}{N} = E_{\rm FG}\left(1 - \frac{1}{\eta} + \frac{A}{\eta^2}\right) , \tag{4.12}$$

we find the result $A = 0.06(2)$ for the coefficient of the second order term (See Fig. 4.4). Our value for A is not compatible with Bloom's result $A = 0.28$ while it is compatible with the result $A = 3/4 - \log 2$ for the coefficient of the second order term reported in Ref. [ERZ92]. However, we disagree with Ref. [ERZ92] on the value of the constant in the definition of η.

In Fig. 4.5 we show the results for the pairing gap $\Delta_{\rm gap}$ in the strong-coupling regime. This quantity is defined from the difference of ground-state

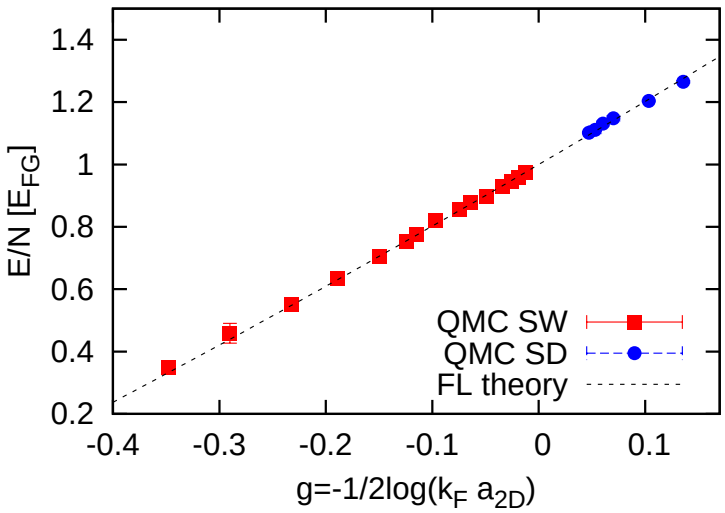

Figure 4.4: Energy per particle for a weakly attractive gas and a weakly interacting gas in $2D$. The red squares are DMC results with square well interaction and the blue circles are obtained with soft disk interaction, with interaction range $R = 2a_{2D}$. The black dashed line is the energy functional introduced in the text (4.12).

energy $E(N_\uparrow, N_\downarrow)$ of systems with one and two more (less) particles $\Delta_{\rm gap} = 1/2[2E(N/2 \pm 1, N/2) - E(N/2 \pm 1, N/2 \pm 1) - E(N/2, N/2)]$ [CCPS03]. At the level of mean-field theory [Miy83, RDS89, RDS90] the pairing gap coincides with the result for the order parameter $\Delta_{\rm gap} = \Delta = \sqrt{2\varepsilon_F|\varepsilon_b|}$ if $|\varepsilon_b| < 2\varepsilon_F$, and is given by $\Delta_{\rm gap} = \varepsilon_F + |\varepsilon_b|/2$ for larger values of $|\varepsilon_b|$. In the BEC regime the quantity $\Delta_{\rm gap} - |\varepsilon_b|/2$ shown in the inset of Fig. 4.5 is determined by the repulsive interaction between unpaired fermionic atoms and bosonic dimers. In fact, the energy of the system with one extra spin-up particle can be written as the sum of the contribution (4.11) of $N/2$ dimers and the Fermi-Bose interaction energy: $E(N/2+1, N/2) = E(N/2, N/2) + g_{BF} n_d$, where $g_{BF} = 3\pi\hbar^2/[m \log(1/n_d a_{ad}^2)]$ is the coupling constant fixed by the atom-dimer reduced mass $2m/3$ and the effective scattering length a_{ad}. By using the definition of $\Delta_{\rm gap}$ and the value $a_d = 0.55 a_{2D}$ for the dimer-dimer scattering length in the energy functional (4.11), we find $a_{ad} = 1.7(1) a_{2D}$ from the best fit shown in the inset of Fig. 4.5. Unfortunately to our knowledge there are no analytical results for the Bose-Fermi mixture in $2D$ up to second order, so that we are forced to use only the first order contribution: that is why we call a_{ad} an effective scattering length. However we can suppose that higher order contributions are very small, like in the $3D$ case (see [PG08]).

Finally, we calculate the contact parameter C [Tan08a, Tan08b] defined

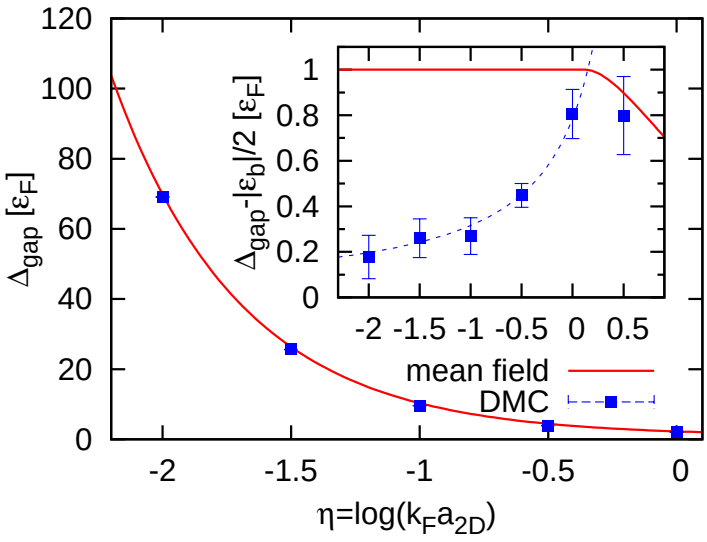

Figure 4.5: Excitation gap in the BCS-BEC crossover. The solid (red) line is the result of mean-field theory. Inset: excitation gap with $|\varepsilon_b|/2$ subtracted from $\Delta_{\rm gap}$. The dashed (blue) line is a fit using the energy functional of a Bose-Fermi mixture.

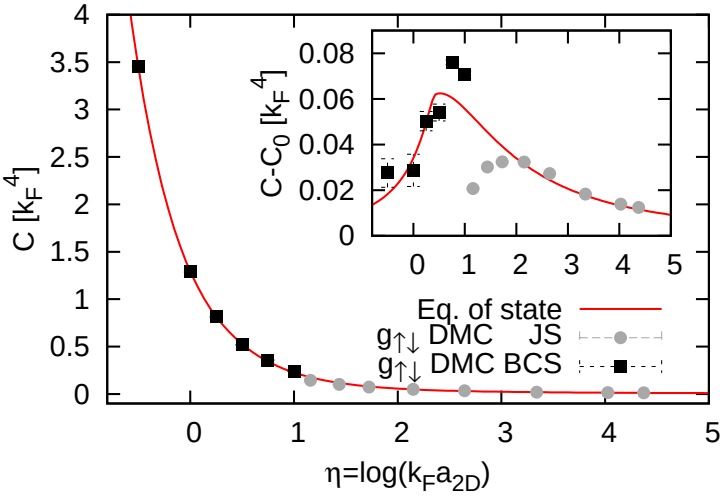

Figure 4.6: Contact parameter in the BCS-BEC crossover. The solid (red) line corresponds to the calculation from the derivative of the equation of state reported in Fig.4.1. Inset: Contact parameter with the two-body contribution C_0 subtracted.

from the short-range behavior of the antiparallel pair distribution function $\lim_{r\to 0} g_{\uparrow\downarrow}(r) = 4C/k_F^4 \log^2(r/a_{2D})$ [WC10]. The limit $r \to 0$ is intended here as $R < r \ll k_F^{-1}$ (see Sec. 1.4). The contact parameter is also related to the derivative of the equation of state with respect to the interaction parameter $C = (2\pi m/\hbar^2) d(nE/N)/d(\log k_F a_{2D})$ [WC10]. The results are shown in Fig. 4.6. In the inset we show the quantity $C - C_0$, where $C_0 = (\pi m/\hbar^2) d(n\varepsilon_b)/d(\log k_F a_{2D})$ is the contribution to the contact C from the molecular state. The comparison between the two determinations of C is a stringent consistency check of the theoretical approach. We find a good agreement with Tan's relation, apart from the region $\log(k_F a_{2D}) \sim 1$ where small deviations are visible, both with the JS and BCS-type wave function, showing the need of a better optimization of ψ_T.

4.6 Quasi-$2D$ configuration

An important question relates to the relevance of these results for systems in harmonic traps. 2D configurations are realized if the transverse confinement is strong enough to reduce the kinematics to the xy-plane: $\hbar\omega_z \gg \varepsilon_F = \hbar\omega_\perp \sqrt{N}$, where we assumed isotropic trapping in the radial direction $\omega_x = \omega_y = \omega_\perp$. In these conditions the effective 2D scattering length can be expressed in terms of a_{3D} and the transverse harmonic oscillator length $a_z = \sqrt{\hbar/m\omega_z}$ being given by $a_{2D} = a_z(2\sqrt{\pi/B}/e^\gamma) \exp(-\sqrt{\pi/2}\, a_z/a_{3D})$, where $B \simeq 0.915$ [PS01]. For small, negative values of the 3D scattering length a_{3D} the system is found in the BCS regime corresponding to an exponentially large a_{2D}. The BEC regime is reached if the absolute value of a_{3D} is increased such that $|a_{3D}| \gg a_z/\log(1/k_F a_z)$. An additional requirement concerns the dimer state, which is well described by the 2D expression only if $|\varepsilon_b| \ll \hbar\omega_z$ [PS01], or equivalently $a_{2D} \gg a_z$. We believe that this latter condition can be relaxed if, in the comparison with the results reported in this work, one considers quantities where the molecular contribution has been subtracted out.

This work, as part of the European Science Foundation EUROCORES Program "EuroQUAM-FerMix", was supported by funds from the CNR and the EC Sixth Framework Programme.

Chapter 5

Density profiles of a three dimensional trapped imbalanced Fermi gas

In this Chapter we use Local Density Approximation and QMC based equations of state to study the density profiles of mixtures of Fermi gases in harmonic traps in three dimensions. We also compare our results with experiments, finding good agreement. The experimental and theoretical studies of spin imbalanced Fermi gases are relevant for addressing the issue of the polarization driven superfluid transition at zero temperature. This Chapter is based on the published paper [BG09].

5.1 Introduction

The field of ultracold two-component Fermi gases with population imbalance is a very active area of research which in recent years has attracted a great deal of interest both experimentally and theoretically [GPS08]. The experiments are carried out with clouds of atoms confined in harmonic traps and the analysis of the measured density profiles is a key diagnostic tool to investigate issues such as shell structures and the phase transition from a superfluid to a normal state of the gas. Important achievements of this technique have been the observation of phase separation between a superfluid core and a normal external shell driven by the degree of polarization [ZSSK06a, PLK$^+$06], by the interaction strength tuned across a Feshbach resonance [SZS$^+$06, SSSK08a] and by the temperature of the gas [ZSSK06b, PLL$^+$06, SSSK08b].

In the unitary limit, corresponding to a diverging scattering length between the spin-up and spin-down components of the fermionic mixture, the density profiles of the polarized gas have been investigated in details in Ref. [LRGS06, RLS08]. This theoretical study is based on an accurate de-

termination of the equation of state of the strongly-interacting normal gas as a function of imbalance obtained using quantum Monte Carlo methods. It provides predictions for the shape of the profiles, for the density jump at the boundary of the superfluid core and for the critical polarization when the system turns fully normal, which are in excellent agreement with the experimental findings of the MIT group [SSSK08b]. In the Bose-Einstein condensate (BEC) limit of small and positive scattering lengths, the polarized gas is predicted to behave like a mixture of composite bosons (the bound dimer molecules) and fermions (the unpaired atoms) [PS06, TGO07, IS08]. The density profiles in this regime have been investigated theoretically in Refs. [PS06, IS08] and experimentally in the recent study by the MIT group [SSSK08a], where the Bose-Fermi mixture model is quantitatively tested at the level of mean-field theory, including also higher order corrections. At finite temperature, the density profiles of a trapped polarized Fermi gas have also been the object of theoretical investigations based on self-consistent approaches both at unitarity [CCHL07] and in the BEC regime [IS08].

The phase diagram of the uniform gas at zero temperature as a function of polarization and interaction strength has been calculated using quantum Monte Carlo (QMC) techniques in Ref. [PG08]. This study provides a precise determination of the equation of state of four different phases competing for the ground state of the system: (a) the unpolarized and (b) polarized superfluid gas and (c) the fully and (d) partially polarized normal gas. The quantum phase transition from the normal to the superfluid state is first order and is accompanied by a region of phase separation where the two phases coexist in equilibrium. Only in the deep BEC regime, where the Bose-Fermi mixture model applies, the transition from a fully polarized Fermi gas to a miscible mixture of few superfluid bosons in a Fermi sea becomes second order.

In this Chapter we use the knowledge of the energy functionals of the uniform phases (a)-(d) as a function of polarization and interaction strength and using the local density approximation we calculate the phase diagram of a trapped gas and the density profiles of both spin components. We determine the conditions for the appearance of a superfluid unpolarized core and of a jump in the density profile signaling the occurrence of the first order quantum phase transition from superfluid to normal. The calculated density profiles are compared with the experimental ones of Ref. [SSSK08a] for different values of the interaction strength, from the unitary to the BEC limit, and for different values of the polarization. In Sec. 5.2 we introduce the equations of state of the four uniform phases (a)-(d) and in Sec. 5.3 we discuss the equations of mechanical and chemical equilibrium when the harmonic external potential is present. In Sec. 5.4 we present the results for the phase diagram, the density profiles and for the radii of the various shells present in the cloud. Conclusions are drawn in Sec. 5.5.

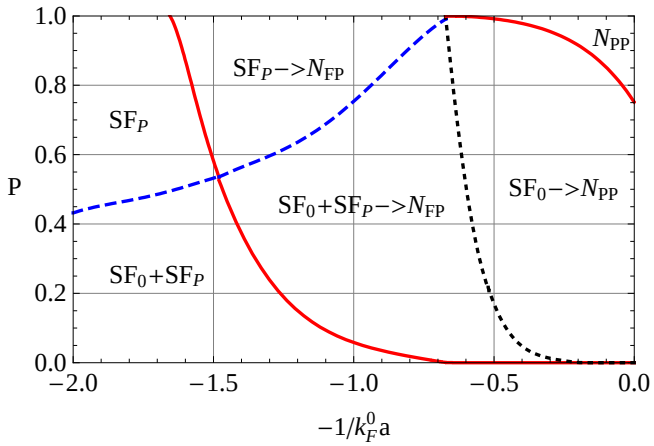

Figure 5.1: Phase diagram for trapped atoms at zero temperature as a function of polarization and interaction strength. The regions correspond to different shell structures (see text). Inside the two (red) solid lines a jump in the density profile marks the superfluid-normal first order phase transition. Above the (blue) dashed line the unpolarized SF_0 superfluid inner core is absent. On the right of the dotted line the polarized SF_P superfluid phase is absent, while on the left the partially polarized N_{PP} normal phase is absent.

5.2 Uniform phases

In this Section we introduce the uniform phases considered in Ref. [PG08] and we discuss their energy densities as a function of the concentration of spin-down particles (the minority species) and of the interaction strength. The natural unit of energy is provided by the Fermi energy of the spin-up majority component

$$E_{F\uparrow} = \frac{\hbar^2 k_{F\uparrow}^2}{2m} = \frac{\hbar^2 (6\pi^2 n_\uparrow)^{2/3}}{2m} \,, \tag{5.1}$$

where $k_{F\uparrow}$ is the Fermi wave vector of the spin-up particles fixed by their particle density $n_\uparrow$. For trapped systems, where the density varies with position, the above equation defines the local Fermi energy.

(a) *Unpolarized superfluid gas* (SF_0). In this phase the spin-up and spin-down particle densities are equal $n_\uparrow = n_\downarrow = n/2$. For positive values of the s-wave scattering length ($a > 0$) the energy density can be written in the form

$$\mathcal{E}_{SF_0}(n/2) = \frac{n}{2}\varepsilon_b + \left(\frac{3}{5} n_\uparrow E_{F\uparrow}\right) 2G(1/k_{F\uparrow}a) \,. \tag{5.2}$$

In the above equation ε_b denotes the binding energy of the molecule ($\varepsilon_b = -\hbar^2/ma^2$ for a zero-range potential) and $G(1/k_{F\uparrow}a)$ is a dimensionless function of the interaction parameter $\eta = 1/k_{F\uparrow}a$. A suitable parametrization of

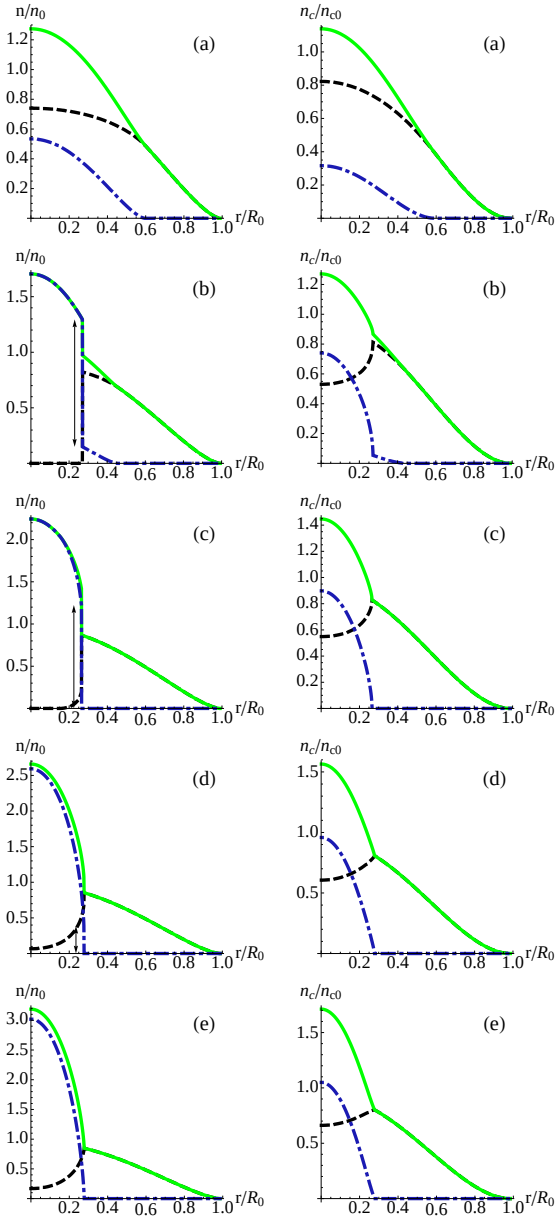

Figure 5.2: Density (left column) and column density (right column) profiles at $P = 0.8$ for different values of the interaction strength. Row (a) corresponds to unitarity ($1/k^0_{F\uparrow}a = 0$), row (b) to $1/k^0_{F\uparrow}a = 0.4$, row (c) to $1/k^0_{F\uparrow}a = 0.8$, row (d) to $1/k^0_{F\uparrow}a = 1.2$ and row (e) to $1/k^0_{F\uparrow}a = 1.7$. The solid (green) lines refer to the majority spin-up component, the dot-dashed (blue) lines to the minority spin-down component and the dashed (black) lines to the density difference $n_\uparrow - n_\downarrow$. The jump in the density $n_\uparrow$ of the minority component is shown with a vertical double arrow. The reference density n_0, column density n_{c0} and radius R_0 all refer to a non-interacting Fermi gas with $N_\uparrow$ particles.

$G(\eta)$, which well reproduces the QMC results from the BEC to the unitary limit (see Ref. [PG08]), is provided by the following formula

$$G(\eta) = \begin{cases} \alpha_0 + \alpha_1 \arctan(\alpha_2 \eta) & (\eta < 0.699) \,, \\ \epsilon(\eta) + \frac{\alpha_3}{\eta^3} + \frac{\alpha_4}{\eta^4} & (\eta > 0.699) \,, \end{cases} \tag{5.3}$$

where we defined the function

$$\epsilon(\eta) = 5(0.60/\eta)/(18\pi)[1 + 128(0.60/\eta)^{3/2}/(15\sqrt{6}\pi^{3/2})] \,, \tag{5.4}$$

while the constants α_{0-4} have the following values: $\alpha_0 = 0.434$, $\alpha_1 = -0.292$, $\alpha_2 = 2.90$, $\alpha_3 = 0.0129$ and $\alpha_4 = -0.0100$. The function G as defined above is continuous at $\eta = 0.699$ with continuous first derivative. For $k_{F\uparrow}a \ll 1$ it reduces to the function $\epsilon(\eta)$, which corresponds to the energy, including the Lee-Huang-Yang (LHY) beyond mean-field correction, of a gas of composite bosons interacting with the dimer-dimer scattering length $a_{dd} = 0.60a$.

(b) *Polarized superfluid gas* ($\mathrm{SF_P}$). This phase is characterized by a density $n_P = n_\downarrow$ of pairs and a density $n_A = n_\uparrow - n_\downarrow$ of unpaired atoms, such that $n = 2n_P + n_A$. The concentration of the minority atoms is denoted by $y = n_\downarrow/n_\uparrow$. For $1/k_{F\uparrow}a \geq 0.5$ an accurate parametrization of the equation of state is provided by the following energy functional

$$\mathcal{E}_{\mathrm{SF_P}} = \mathcal{E}_{\mathrm{SF_0}}(n_P) + \frac{3}{5} n_\uparrow E_{F\uparrow} \left[(1-y)^{5/3} + \frac{5 k_{F\uparrow} a_{ad}}{3\pi} y(1-y) \right] \,. \tag{5.5}$$

The first term on the right hand side is the energy density (5.2) of an unpolarized superfluid with density $2n_P$. The other two terms correspond to the kinetic energy of a gas with density n_A of unpaired fermions and to the interaction energy, treated at the level of mean field, between unpaired and paired atoms parametrized by the atom-dimer scattering length $a_{ad} = 1.18a$. With the above energy functional one recovers the Bose-Fermi mixture model in the deep BEC limit corresponding to $1/k_{F\uparrow}a \gg 1$.

(c) *Fully polarized normal gas* ($\mathrm{N_{FP}}$). In this phase the density of spin-down particles vanishes ($n_\downarrow = 0$) and the energy density coincides with the one of an ideal Fermi gas

$$\mathcal{E}_{\mathrm{N_{FP}}} = \frac{3}{5} n_\uparrow E_{F\uparrow} \,. \tag{5.6}$$

(d) *Partially polarized normal gas* ($\mathrm{N_{PP}}$). This phase is characterized by the concentration $x = n_\downarrow/n_\uparrow$ of the spin-down particles. For small concentrations ($x \ll 1$) the dependence on x of the energy functional can be written in the form of the Landau-Pomeranchuk Hamiltonian of weakly interacting fermionic quasiparticles [BP91, LRGS06, RLS08, Che06, BF07, CRLC07, PG08, PS08]

$$\mathcal{E}_{\mathrm{N_{PP}}} = \frac{3}{5} n_\uparrow E_{F\uparrow} \left(1 - Ax + \frac{m}{m^*} x^{5/3} + F x^2 \right) \,, \tag{5.7}$$

where A is the binding energy of a single spin-down quasiparticle in the Fermi sea of spin-up particles, m^* is its effective mass and F represents the interaction between quasiparticles. These quantities all depend on $\eta = 1/k_{F\uparrow}a$. We used the following parametrizations, which well reproduce the QMC results when $\eta > 0$:

$$A(\eta) = -\frac{5\varepsilon_b}{3E_{F\uparrow}} + \beta_0 + \beta_1\eta + \beta_2\eta^2 + \beta_3\eta^3 \,, \tag{5.8}$$

where the first term on the right hand side is conveniently introduced in analogy with (5.2) and the constants β_{0-3} have the following values: $\beta_0 = 0.986$, $\beta_1 = 1.11$, $\beta_2 = -2.23$, $\beta_3 = 0.847$;

$$\frac{m^*(\eta)}{m} = \gamma_0 + \gamma_1\eta + \gamma_2\eta^2 + \gamma_3\eta^3 + \gamma_4\eta^4 \,, \tag{5.9}$$

where the constants γ_{0-4} are given by $\gamma_0 = 1.11$, $\gamma_1 = 0.255$, $\gamma_2 = 0.337$, $\gamma_3 = 0.0579$, $\gamma_4 = -0.128$; and finally

$$F(\eta) = \delta_0 e^{-(\eta-\delta_1)^2/\delta_2} \,, \tag{5.10}$$

where the constants δ_{0-2} have the values: $\delta_0 = 0.279$, $\delta_1 = 0.438$, $\delta_2 = 0.277$. The equation of state (5.7) only holds for values of the interaction parameter $\eta \leq 0.73$, since for larger values the normal gas becomes fully polarized with $x = 0$ (see Ref. [PG08]). We also notice that the values of the effective mass m^* are smaller than the exact diagrammatic Monte Carlo results of Ref. [PS08] (see comment in Ref. [PG08]). This inaccuracy is compensated in Eq. (5.7) by the coefficient F of the x^2 term, which finally provides a very accurate fit to the QMC results at finite concentration. However, the reported value of F in Eq. (5.10) underestimates the interaction effects between quasiparticles.

5.3 Local Density Approximation

In the presence of the harmonic confinement

$$V_{ho}(\mathbf{r}) = \frac{1}{2}m\omega_x^2x^2 + \frac{1}{2}m\omega_y^2y^2 + \frac{1}{2}m\omega_z^2z^2 \,, \tag{5.11}$$

the particle density depends on position and the concentration $n_\downarrow/n_\uparrow$ varies locally. The most useful parameters for the phase diagram are expressed in this case in terms of the total number $N_\uparrow$ ($N_\downarrow$) of spin-up (spin-down) particles. These are the overall polarization

$$P = \frac{N_\uparrow - N_\downarrow}{N_\uparrow + N_\downarrow} \,, \tag{5.12}$$

and the interaction parameter

$$\frac{1}{k^0_{F\uparrow}a} = \frac{1}{(6\pi^2 n^0)^{1/3}a} = \frac{a_{ho}/a}{(48N_\uparrow)^{1/6}} \,, \tag{5.13}$$

where $a_{ho} = \sqrt{\hbar/m(\omega_x\omega_y\omega_z)^{1/3}}$ is the harmonic oscillator length and $k^0_{F\uparrow}$ and $n^0 = n^0_\uparrow(0)$ are, respectively, the Fermi wave vector and the central trap density of a non-interacting Fermi gas with $N_\uparrow$ particles.

In the local density approximation (LDA) the energy density of the inhomogeneous system is approximated at each spatial position by the one corresponding to a uniform gas at the local value of the density. This approximation becomes exact in the limit of large particle numbers, when the density changes slowly on the typical length scale associated with the external potential. We construct the grand-canonical potential Ω at zero temperature as the integral over space of the ground-state energy density $\mathcal{E}$, which depends on the local interaction parameter $\eta(\mathbf{r}) = [n_\uparrow(\mathbf{r})/n^0]^{-1/3}/(k^0_{F\uparrow}a)$ and the local polarization $P(\mathbf{r}) = [n_\uparrow(\mathbf{r}) - n_\downarrow(\mathbf{r})]/[n_\uparrow(\mathbf{r}) + n_\downarrow(\mathbf{r})]$, that is

$$\Omega = \int d\mathbf{r}\, \{\mathcal{E}\,[\eta(\mathbf{r}), P(\mathbf{r})] + [n_\uparrow(\mathbf{r}) + n_\downarrow(\mathbf{r})]V_{ho}(\mathbf{r}) - n_\uparrow(\mathbf{r})\mu_\uparrow - n_\downarrow(\mathbf{r})\mu_\downarrow\} \,. \tag{5.14}$$

Here $\mathcal{E}$ corresponds to the uniform phase present at position $\mathbf{r}$, with the densities of the fermionic species replaced by the local densities, while $\mu_\uparrow$ and $\mu_\downarrow$ are the chemical potentials of the spin-up and spin-down particles, introduced as Lagrange multipliers. When studying the superfluid phase we introduce the chemical potential μ_S of the pairs and the chemical potential μ_A of the excess spin-up fermions; chemical equilibrium at the interface between the superfluid region and the normal region is imposed by setting $\mu_S = \mu_\uparrow + \mu_\downarrow$ and $\mu_A = \mu_\uparrow$.

The density profiles are obtained by minimizing the grand-canonical potential (5.14) with respect to the densities $n_\uparrow(\mathbf{r})$ and $n_\downarrow(\mathbf{r})$ of the two spin components. The condition of stationarity gives the LDA equations for the superfluid phase:

$$\begin{cases} \mu_S = & \partial\mathcal{E}_{\mathrm{SF_P}}/\partial n_P + 2V_{ho}(\mathbf{r}) \,, \\ \mu_A = & \partial\mathcal{E}_{\mathrm{SF_P}}/\partial n_A + V_{ho}(\mathbf{r}) \,, \end{cases} \tag{5.15}$$

and for the normal phase:

$$\begin{cases} \mu_\uparrow = & \partial\mathcal{E}_{\mathrm{N_{PP}}}/\partial n_\uparrow + V_{ho}(\mathbf{r}) \,, \\ \mu_\downarrow = & \partial\mathcal{E}_{\mathrm{N_{PP}}}/\partial n_\downarrow + V_{ho}(\mathbf{r}) \,. \end{cases} \tag{5.16}$$

Notice that mechanical equilibrium is enforced by the continuity requirement of the grand-canonical potential density along the cloud profile. For

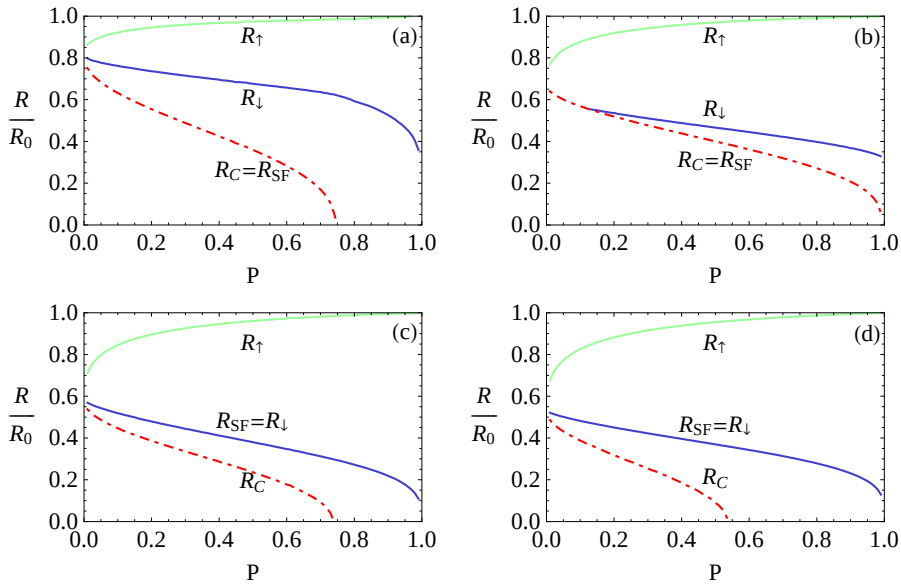

Figure 5.3: Radii of the spin-up ($R_\uparrow$) and spin-down ($R_\downarrow$) components and of the unpolarized superfluid core R_c as well as of the superfluid shell $R_{\rm SF}$ as a function of polarization for different values of the interaction strength. Panel: (a) $1/k^0_{F\uparrow}a = 0$, (b) $1/k^0_{F\uparrow}a = 0.5$, (c) $1/k^0_{F\uparrow}a = 1$, (d) $1/k^0_{F\uparrow}a = 1.5$. All the radii are divided by the radius R_0, which refers to a non-interacting Fermi gas with $N_\uparrow$ particles.

each point in the harmonic trap we solve the two set of coupled equations, choosing the phase that minimizes the local grand-canonical potential and checking that the compressibility is positive. As usual, the integral of density over space allows us to fix the chemical potentials once we know the number of particles, or in our case, the total polarization and the interaction parameter.

5.4 Results

The shell structure of the atomic cloud for a given value of the polarization P and interaction strength $1/k^0_{F\uparrow}a$ is schematically described by the phase diagram shown in Fig. 5.1. The various regions denote different sequences of phases starting from the center of the trap. The most external shell is always composed by the majority spin-up atoms only ($\rm N_{FP}$ phase). Outside the region delimited by the two (red) solid lines the sequence of phases corresponds to a continuous density profile, while inside it corresponds to a density profile which exhibits a jump marking the first order phase transition from the superfluid to the normal state.

For large values of P and close to the regime of resonant interaction, the system is normal and displays an internal shell of the $\rm N_{PP}$ phase. The cor-

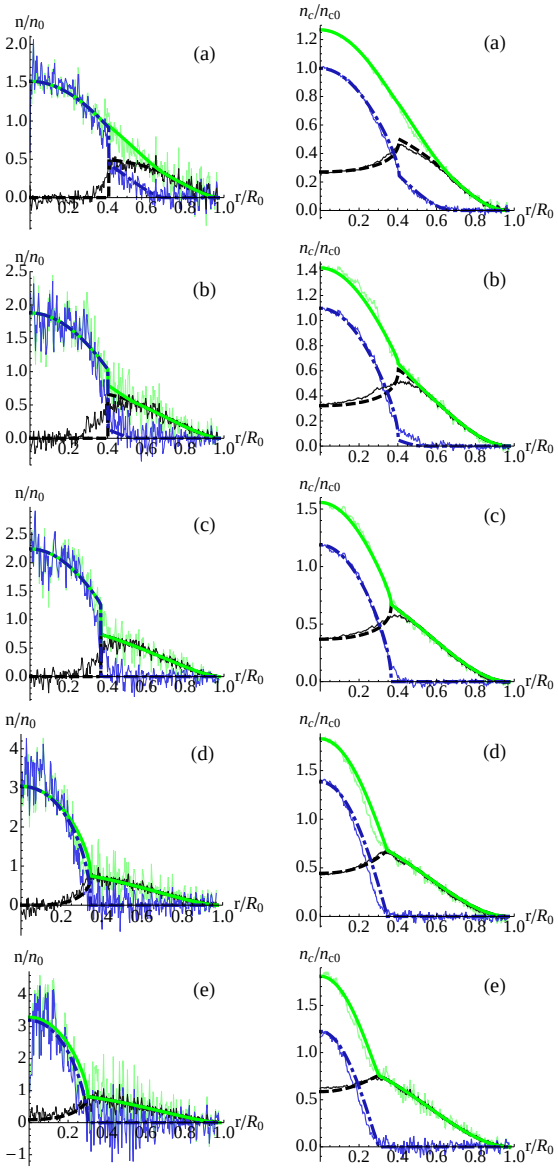

Figure 5.4: Comparison between calculated and experimental density (left column) and column density (right column) profiles for different values of polarization and interaction strength. Row (a) corresponds to $P = 0.43$ at unitarity ($1/k^0_{F\uparrow}a = 0$), row (b) to $P = 0.52$ and $1/k^0_{F\uparrow}a = 0.35$, row (c) to $P = 0.57$ and $1/k^0_{F\uparrow}a = 0.61$, row (d) to $P = 0.61$ and $1/k^0_{F\uparrow}a = 1.2$ and row (e) to $P = 0.73$ and $1/k^0_{F\uparrow}a = 1.6$. The theoretical profiles are plotted as in Fig. 5.2. The corresponding experimental profiles are shown with thin lines. The reference density n_0, column density n_{c0} and radius R_0 all refer to a non-interacting Fermi gas with $N_\uparrow$ particles. The experimental profiles are from Refs. [SSSK08b, SSSK08a].

responding profile for both the spin-up and spin-down component is shown in column (a) of Fig. 5.2. For the largest values of the interaction parameter $1/k^0_{F\uparrow}a$, corresponding to the leftmost region of Fig. 5.1, the central part of the cloud is either a polarized SF_P superfluid (see column (e) in Fig. 5.2) or, for smaller polarizations, an unpolarized SF_0 superfluid surrounded by the SF_P phase. In both cases the transition from the superfluid core to the N_{FP} normal external shell is continuous and, within the picture of Bose-Fermi mixtures, corresponds to a vanishing density of composite bosons. The superfluid-normal transition is instead first order in the case of the other three shell sequences shown in Fig. 5.1. These are: the $SF_0 \rightarrow N_{PP}$ structure shown in column (b) of Fig. 5.2, the SF_0+$SF_P \rightarrow N_{FP}$ shown in column (c) and the $SF_P \rightarrow N_{FP}$ shown in column (d). The jump occurring at the transition in the density profile of the minority spin component is shown in Fig. 5.2 with a vertical double arrow.

The (blue) dashed line in Fig. 5.1 separates the region where an inner core of unpolarized SF_0 superfluid is present (below the line), from the region where the polarized SF_P phase survives at the center of the cloud. The dotted line, instead, separates the region where the first order phase transition is from an unpolarized superfluid to a partially polarized normal gas (right of the line), from the region where it is from a polarized superfluid to a fully polarized normal gas (left of the line). The values of P and $1/k^0_{F\uparrow}a$ for which a first order phase transition directly between the SF_P and the N_{PP} phase is predicted, would correspond to a very tiny region around the dotted line in Fig. 5.1, smaller than in the homogeneous case (see Fig. 4 of Ref. [PG08]) and involving such small densities of the minority component to be experimentally irrelevant.

The structure of the cloud as a function of polarization and interaction strength can also be analyzed in terms of the radii of the various shells as shown in Fig. 5.3. The radii of the spin-up and spin-down components, respectively $R_\uparrow$ and $R_\downarrow$, as well as the radii of the unpolarized superfluid core R_c and of the superfluid component R_{SF} are presented as a function of the polarization P for different values of the interaction strength. Panel (a) of Fig. 5.3 shows the behavior of the radii at unitarity ($1/k^0_{F\uparrow}a = 0$): the superfluid core exists here only if $P < 0.77$, while for larger values of P a partially polarized N_{PP} gas is present for $R < R_\downarrow$. At $1/k^0_{F\uparrow}a = 0.5$ [panel (b)] the inner part of the cloud is always superfluid and a N_{PP} normal shell still survives surrounding the SF_0 superfluid core. For larger values of $1/k^0_{F\uparrow}a$ [panels (c) and (d)] the superfluid core is directly surrounded by the fully polarized N_{FP} gas, but the radii R_{SF} and R_c are now different corresponding to the structure of an unpolarized SF_0 inner core surrounded by a polarized SF_P external shell.

Finally in Fig. 5.4 we report the results of the comparison between the calculated density profiles and the ones measured in the recent experiment of Refs. [SSSK08b, SSSK08a]. We compare both density and column density

profiles for different values of polarization and interaction strength. It is worth stressing that there are no free parameters in this comparison, once the values of P and $1/k^0_{F\uparrow}a$ are extracted from the experimental data. The agreement is remarkable for all values of the interaction parameter from the unitary limit to the deep BEC regime, where it supports the picture of an interacting Bose-Fermi mixture [SSSK08a]. Small discrepancies, mainly visible as a broader density difference profile, are found close to the unitary limit [see panel (b) of Fig. 5.4] and might be attributed to temperature effects. Notice that the experimental profiles shown in columns (b)-(e) of Fig. 5.4 are taken from Ref. [SSSK08a] and could correspond to a slightly higher temperature compared to the ones of column (a) which are taken from Ref. [SSSK08b]. See also the comparison in Fig. 4 of Ref. [SSSK08b].

5.5 Conclusions

We have investigated the density profiles of trapped polarized Fermi mixtures at zero temperature. The starting point is the reliable determination of the phase diagram of uniform systems obtained in Ref. [PG08] using QMC methods, whose implications for trapped systems are derived by applying the local density approximation. The comparison with the profiles measured in experiments shows a good agreement from the unitary limit to the BEC regime, providing new physical insights into the strongly interacting polarized normal and superfluid phases recently realized with ultracold atoms.

Chapter 6

First and second sound in cylindrically trapped Fermi gases

In this Chapter we discuss the problem of sound propagation in a strongly interacting Fermi gas in a cylindrically trapped configuration. We find that there are important differences with respect to homogeneous systems, depending on geometry and dissipative effects. This analysis could be useful for the detection of second sound in superfluid Fermi gases. This Chapter is based on the published paper [BPS10].

6.1 Introduction

Superfluids are known to exhibit, in addition to usual sound, an additional mode, called second sound, where the superfluid and normal components move with opposite phase [Lan41]. In a weakly compressible fluid, like superfluid helium, second sound reduces to a temperature wave, leaving the total density practically unaffected. In helium its velocity was systematically measured as a function of temperature, providing a high precision determination of the superfluid density. First measurements of second sound were recently reported also in dilute Bose-Einstein condensed gases confined in elongated traps [MKv09]. In this Chapter we show that the propagation of sound in a nonuniform trapped gas exhibits new interesting features both in the superfluid and in the normal phase. We will focus on highly elongated configurations where the radial harmonic trapping provides the relevant nonuniformity. These configurations are well suited for the experimental excitation and detection of sound waves [AKM$^+$97, JCL$^+$07, HNUM10]. We will consider the usual hydrodynamic regime $l \ll \lambda$ where l is the mean free path and λ is the wavelength of the sound wave. We will also consider the condition of strong radial confinement $R_\perp \ll \lambda$, where $R_\perp$ is the radial

size of the sample, provided that the Thomas Fermi regime is reached at equilibrium (therefore we do not consider a pure $1D$ problem).

The above conditions are compatible with two different regimes, depending on the ratio between the viscous penetration depth $\delta = \sqrt{\eta/\rho_n\omega}$ and the radius $R_\perp$, where η is the shear viscosity coefficient, ρ_n is the normal density and ω is the frequency of the sound wave. The penetration depth is the typical distance from a surface at which an oscillation of the fluid along the same surface becomes attenuated due to shear viscosity [LL87].

Let us first consider the case of a uniform fluid confined by the hard walls of a tube. If $\delta \ll R_\perp$ viscosity plays an unimportant role and sound propagates similarly to the case of bulk matter. If instead $\delta \gg R_\perp$, the viscosity imposes the uniformity of the normal velocity field as a function of the radial coordinate. Since friction between the normal part of the fluid and the walls further requires that the normal velocity be zero on the walls, the normal part cannot move at all along the tube and only the superfluid can. This mode is known as 4-th sound [Atk59]. In the case of a harmonically trapped gas the two regimes exhibit new features whose investigation is the object of the present Chapter.

Our analysis is based on the two-fluid hydrodynamic equations (HD) [Kha65] which reduce, above T_C, to the classical equations of hydrodynamics. They represent local conservation laws for mass, momentum and entropy, including dissipative terms; they are valid only if the fluid can always be considered at local thermal and mechanical equilibrium. Therefore only sufficiently smooth and slow perturbations of the density and entropy can be considered, so that $l \ll \lambda$, as noted before, or equivalently $\omega\tau \ll 1$, where τ is a typical collisional time. This allows to consider the density, momentum, temperature, pressure, chemical potential and entropy density as smooth fields. Moreover, an equation for the superfluid velocity, which is irrotational, is included. The HD equations are:

$$\partial_t \rho + \boldsymbol{\nabla} \cdot \mathbf{j} = 0, \tag{6.1}$$

$$\partial_t j_i + \partial_i P + \rho \partial_i U/m = \partial_k(\eta \Gamma_{ik}), \tag{6.2}$$

$$\partial_t s + \boldsymbol{\nabla} \cdot (s\mathbf{v}_n) = \nabla \cdot (\kappa \nabla T/T)\,., \tag{6.3}$$

$$m\partial_t \mathbf{v}_s = -\boldsymbol{\nabla}\,(\mu + U)\,. \tag{6.4}$$

In the above equations $\mathbf{j} = \rho_s \mathbf{v}_s + \rho_n \mathbf{v}_n$ is the current density, ρ_s and ρ_n are the superfluid and normal mass densities for a fluid with total mass density $\rho = \rho_s + \rho_n$, $\mathbf{v}_s$ and $\mathbf{v}_n$ are the corresponding velocity fields, $\Gamma_{ik} = (\partial_k v_{ni} + \partial_i v_{nk} - 2\delta_{ik}\partial_j v_{nj}/3)$, s is the entropy density, while P and μ are, respectively, the local pressure and chemical potential. U is the external trapping potential which will be assumed of axial harmonic form: $U = m(\omega_\perp^2 r_\perp^2 + \omega_z^2 z^2)/2$ with $r_\perp^2 = x^2 + y^2$ and $\omega_z \ll \omega_\perp$. Since we are interested only in the linear solutions, in the above equations we have omitted terms quadratic in the velocity. Finally η and κ are, respectively, the

shear viscosity and the thermal conductivity (we have not considered bulk viscosities terms which give smaller contributions).

In a uniform fluid the effect of viscosity and thermal conductivity is irrelevant in the long wave length limit, providing only higher order corrections to the dispersion law. In the presence of confinement their effect is instead crucial. This opens new perspectives to explore the behavior of viscosity and thermal conductivity in interacting trapped gases. The two-fluid hydrodynamic equations, in the dissipationless regime ($\eta = \kappa = 0$), have been already the object of numerical investigations [TG05, THL$^+$09, HCCL07] in the presence of harmonic confinement. These works, so far limited to isotropic trapping, have provided predictions for the discretized frequencies in the superfluid phase with special emphasis to the hybridization effects between the first and second sound solutions.

In this Chapter we are interested in the solutions of the hydrodynamic equations satisfying the condition $\omega \ll \omega_\perp$. As a consequence of the tight radial confinement, Eq. (6.2) for the current implies the important condition

$$\nabla_\perp P + \rho \nabla_\perp U = 0 \tag{6.5}$$

of mechanical equilibrium along the radial direction. Violation of this condition would in fact result in frequencies of the order of $\omega_\perp$. The tight radial confinement also implies that the radial component of the velocity field must be much smaller than the longitudinal one.

6.2 Low frequency dissipative regime

In the presence of harmonic trapping the condition $\delta \gg R_\perp$ of large viscous penetration depth is equivalent to requiring the low frequency condition $\omega \ll \omega_\perp^2 \tau$. This can be obtained by estimating, as usual, $\eta \approx \tau \bar{v} \rho$, where $\bar{v}$ is the average velocity of the particles, of the order of the Fermi velocity $\sim v_F$.

Excluding $\mathbf{v}_s$ from Eqs. (6.2) and (6.4) and using the thermodynamic identity $dP = sdT + \rho d\mu/m$ one can write the equation for the relevant z component of the velocity field of the normal component in the form

$$m\rho_n \partial_t v_n^z + \rho_n \partial_z (\delta\mu) + ms\partial_z(\delta T) = m\boldsymbol{\nabla} \cdot (\eta \boldsymbol{\nabla} v_n^z) \,, \tag{6.6}$$

where we have ignored terms containing the small radial components of the velocity field.

The presence of viscosity in Eq. (6.6) results in the independence of v_n^z on the radial coordinate $r_\perp$. In fact violation of such a behavior would be incompatible with the low frequency condition $\omega \ll \omega_\perp^2 \tau$. It is worth noticing that, differently from the case of the tube with hard walls discussed in the introduction, for harmonic trapping the uniformity of the velocity

field does not stop the motion of the normal component. Here we assume that the collisional times responsible for viscosity and thermal conductivity are comparable so, analogously, the presence of thermal conductivity in Eq. (6.3) for the entropy results in the independence of the temperature fluctuations on $r_\perp$ in the same low frequency limit. This in turns implies that also the fluctuations of the chemical potential will be independent of the radial coordinate. This follows from the radial mechanical equilibrium condition and the use of the thermodynamic identity $dP = sdT + \rho d\mu/m$. Thus in the low frequency limit both the fluctuations δT and $\delta\mu$ are independent of the radial coordinates.

It is now convenient to integrate radially both the equations of continuity for the density and for the entropy (6.1, 6.3) as well as Eq. (6.6) for v_n^z, profiting of the fact that the large terms containing the derivatives with respect to $\mathbf{r}_\perp$ vanish due to Gauss theorem, and that those containing the second derivative with respect to z can be ignored since they give rise to higher order corrections in the dispersion law. Integration of Eq.(6.6) then gives

$$-m\langle\rho_n\rangle\partial_t v_n^z = m\langle s\rangle\partial_z\delta T + \langle\rho_n\rangle\partial_z\delta\mu, \tag{6.7}$$

where the symbol $\langle\dots\rangle \equiv \int\dots dxdy$ stands for the integral on the transverse variable $\mathbf{r}_\perp$. The above equation for v_n^z and the analog equation $m\partial_t v_s^z = -\partial_z\delta\mu$ for the superfluid component can be used to derive the following coupled equations for the averaged density and entropy fluctuations:

$$-\partial_t^2\delta\langle\rho\rangle + \partial_z\left(\langle s\rangle\partial_z\delta T\right) + \partial_z\left(\langle\rho\rangle\partial_z\delta\mu\right)/m = 0, \tag{6.8}$$

$$-\partial_t^2\delta\langle s\rangle + \partial_z\left(\langle s\rangle^2/\langle\rho_n\rangle\partial_z\delta T\right) + \partial_z\left(\langle s\rangle\partial_z\delta\mu\right)/m = 0. \tag{6.9}$$

One can further write $\delta\langle\rho\rangle = \partial_\mu\langle\rho\rangle\delta\mu + \partial_T\langle\rho\rangle\delta T$ and $\delta\langle s\rangle = \partial_\mu\langle s\rangle\delta\mu + \partial_T\langle s\rangle\delta T$. The spatial dependence of the thermodynamic quantities entering the above equations is fixed by the trapping potential U through the local density approximation equilibrium condition $\mu(\rho, T) + U = \mu_0$, with μ_0 fixed by the normalization condition for ρ. In the presence of axial trapping ($\omega_z \neq 0$), Eqs. (6.8,6.9) allow for the calculation of the low frequency discretized states of the system. In the following we will assume $\omega_z = 0$ (cylindrical geometry) in order to calculate the velocity of the sound waves propagating along the axial direction. Since we use linearized equations we can assume the t and z dependence $\propto e^{i(qz-\omega t)}$ for the solutions for $\delta\mu$ and δT, with $\omega = cq$, yielding the most relevant equation

$$\begin{aligned} &c^4[m\partial_\mu\langle\rho\rangle\partial_T\langle s\rangle - (\partial_T\langle\rho\rangle)^2] + c^2[2\partial_T\langle\rho\rangle\langle s\rangle - \\ &\langle\rho\rangle\partial_T\langle s\rangle - m\partial_\mu\langle\rho\rangle\langle s\rangle^2/\langle\rho_n\rangle] + \langle\rho_s\rangle\langle s\rangle^2/\langle\rho_n\rangle = 0, \end{aligned} \tag{6.10}$$

which generalizes the well known Landau equation [Lan41, Kha65] for the first and second sound velocities to the case of a cylindrically trapped gas.

Above T_C, where the superfluid density vanishes, Eq.(6.10) admits only one solution with velocity different from zero. In this case the value of c can be more conveniently calculated by direct radial integration of the HD Eqs. (6.1-6.3). In the low frequency limit the equations of continuity for the density and the entropy yield the 1D isoentropic condition $\partial_t(\langle s\rangle/\langle\rho\rangle) = 0$ and one immediately finds the result

$$c^2 = \left(\frac{\partial\langle P\rangle}{\partial\langle\rho\rangle}\right)_{\frac{\langle s\rangle}{\langle\rho\rangle}} , \tag{6.11}$$

which generalizes the most famous expression for the adiabatic sound velocity of uniform matter as well as the zero temperature result $mc^2 = (\partial_\mu\langle\rho\rangle/\langle\rho\rangle)^{-1}$ derived in [CVFT06]. At unitarity, as well as for the ideal gas, where s/ρ depends on the combination $\rho T^{-3/2}$, the new adiabaticity condition takes the form $\langle\rho\rangle T^{-5/2} = const.$ A non trivial implication concerns the sound velocity in the ideal classical limit where one finds $c^2 = (7/5)(T/m)$ rather than the value $(5/3)(T/m)$ holding in uniform gases. See Fig. 6.1 Here and in the following we put the Boltzmann constant $k_B = 1$.

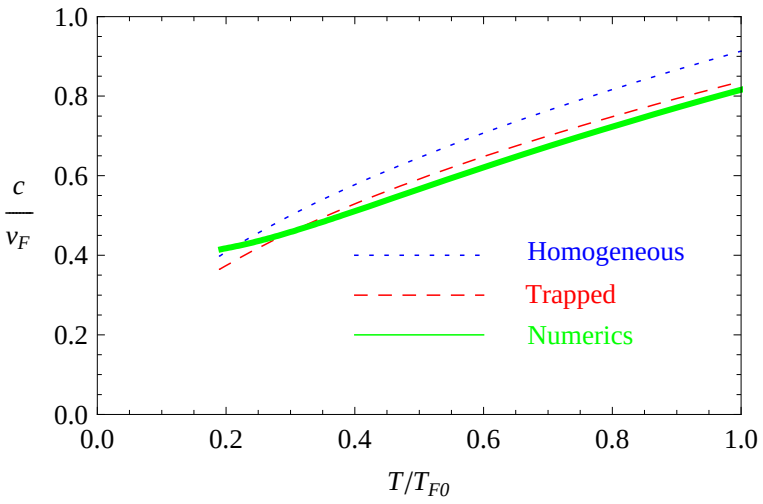

Figure 6.1: Sound velocity, normalized to the Fermi velocity $v_F = \sqrt{2T_F/m}$, above T_C in the homogeneous case (short-dashed line), in the cylindrical case with the approximation $c^2 = (7/5)(T/m)$ (long-dashed line), and calculated numerically (solid line) as described in Sec. 6.3.

Before discussing the solutions of Eq. (6.10) in the presence of harmonic trapping, it is useful to calculate the dynamic response function of the system to an external potential of the form $\lambda e^{i(qz-\omega t)}$. The response function is determined by the density fluctuations induced by the external potential according to $\delta\langle\rho\rangle = \lambda\chi(q,\omega)e^{i(qz-\omega t)}$. Its calculation is important because it provides information on the actual possibility of exciting the two sound

waves using a density probe. The inclusion of the external perturbation affects both the equation for the current and the equation for $\mathbf{v}_s$. Calculations yield the following result for the imaginary part of the response function

$$\mathrm{Im}\chi(\mathrm{q},\omega) = -\langle\rho\rangle\frac{\pi}{2}\{\mathrm{W}_1\omega[\delta(\omega-\mathrm{c}_1\mathrm{q})+\delta(\omega+\mathrm{c}_1\mathrm{q})] + W_2\omega[\delta(\omega-c_2q)+\delta(\omega+c_2q)]\}, \quad (6.12)$$

where the weights W_1 and W_2 obey the relationships $mc_1^2W_1 + mc_2^2W_2 = 1$ and $W_1 + W_2 = (\partial_\mu\langle\rho\rangle/\langle\rho\rangle)_T$ determined, respectively, by the f- and the isothermal compressibility sum rules. The knowledge of $\mathrm{Im}\chi$ is relevant for experiments based on the propagation of density pulses and can be measured directly in Bragg scattering experiments [HTL$^+$10, AN09].

6.3 Calculation of the sound velocities

We are now ready to calculate the values for the two sound velocities and the relative weights in the density response. We will specialize to the case of the unitary Fermi gas [GPS08] since in this case the collisional regime, needed to apply hydrodynamic theory, is more easily achieved due to the large value of the scattering length. At unitarity the effects of the interactions in the thermodynamic functions can be expressed in a universal way [Ho04] in terms of the dimensionless parameter $u \equiv \mu/T$. Thus the pressure can be written as $P(\mu,T) = T^{5/2}H(u)$ where the function $H(u)$ can be determined through microscopic many-body calculations [BDM06, CSL05, HLD10] or, in some ranges of temperature, directly extracted from experiment [NNJ$^+$10]. All the thermodynamic functions can be expressed in terms of the function H. For example the density takes the form $\rho(\mu,T) = mT^{3/2}\nu(u)$ with $\nu(u) = H'(u)$, the entropy density is given by $s = 5P/2T - u\rho/m$ etc. Only the superfluid mass density $\rho_s = mT^{3/2}\nu_s(u)$ requires the knowledge of another independent function for which we use the regularized form introduced in [FOTG07, THLG08].

The radially integrated quantities entering the dispersion relation (6.10) can also be easily calculated. Since in the presence of radial trapping the chemical potential has the radial dependence $\mu(\mathbf{r}) = \mu_0 - m\omega_\perp^2 r_\perp^2/2$ the integration over $dxdy$ can be usefully transformed into integrals over u. For example, we find

$$\langle\rho\rangle(\mu_0,T) = (2\pi T^{5/2}/\omega_\perp^2)\int_{-\infty}^{\mu_0/T}\nu(u)du \quad (6.13)$$

and analogously for the other quantities. In conclusion all the coefficients of the dispersion relation (6.10) can be calculated as a function of T and of the dimensionless variable $u_0 = \mu_0/T$. In practice, in order to determine the function $H(u)$ we have used a fit to the experimental data of [NNJ$^+$10] above

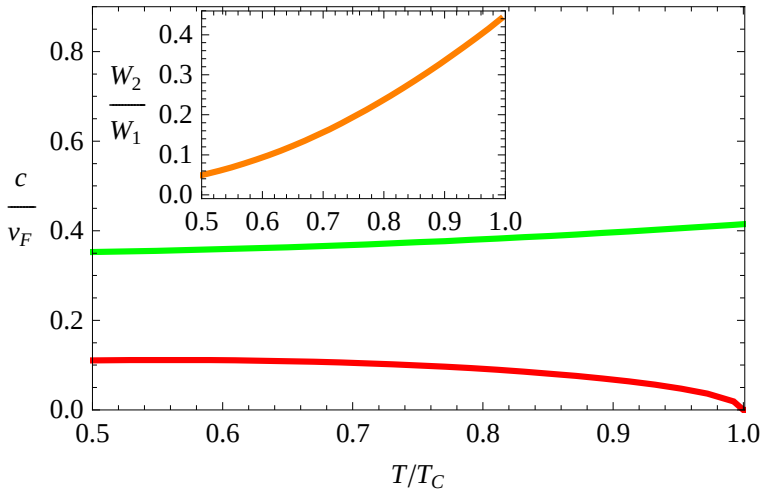

Figure 6.2: First (green) and second (red) sound calculated using Eq.(6.10), as a function of T/T_C, normalized to the Fermi velocity. The inset reports the ratio W_2/W_1 between the weights of the two sounds modes in Imχ [see Eq. (6.12)].

the critical temperature T_C and assumed that, below T_C, the pressure is constant as a function of T, following the analysis in the same reference. The results for the sound velocities c_1 and c_2 and for the relative weights W_2/W_1 [see (6.12)] are reported in Fig. 6.2 for the unitary Fermi gas as a function of T/T_C in the relevant interval $0.5T_C < T < T_C$, where $T_C \approx 0.19T_F$, having defined the Fermi temperature for our cylindrical geometry as

$$T_F = \left(\frac{15\pi}{4} \left(\frac{\hbar^2}{2m} \right)^{3/2} \omega_\perp^2 \langle \rho \rangle \right)^{2/5} . \tag{6.14}$$

Notice that, in the Local Density Approximation regime where $T_F \gg \hbar\omega_\perp$, the ratio T_C/T_F does not depend on the value of the radial confinement.

In Fig. 6.3 we show the ratio between the relative density $(\delta\langle\rho\rangle/\langle\rho\rangle)$ and temperature $(\delta T/T)$ fluctuations in the two modes. The ratio provides a physical insight on the nature of the modes. In the first sound solution (high velocity mode) the relative variations of density are larger than the ones of temperature and have the same sign. The opposite happens for second sound. The value of the ratio W_2/W_1 is smaller than the value found for a uniform fluid [HTL+10] and this is due to the reduction of the superfluid component as one moves from the symmetry axis of the trap. We have also checked that our predictions are not very sensitive to the fitting procedure used to calculate the thermodynamic functions.

In usual harmonic trap configurations, the finite size of the atomic cloud along the z direction poses a major limitation for observing the predicted sound waves. The following inequalities have to be fulfilled: $R_\perp \ll \delta \ll$

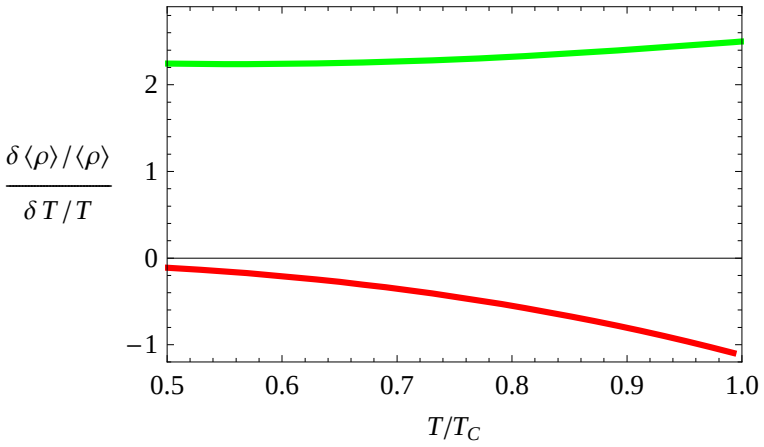

Figure 6.3: Ratio between the relative temperature ($\delta T/T$) and density ($\delta\langle\rho\rangle/\langle\rho\rangle$) fluctuations in the two sounds as a function of T/T_C (see Fig. 6.2 for the notation).

$\lambda \ll R_z$. A typical aspect ratio for highly anisotropic traps is $R_z/R_\perp \sim 70$ [HNUM10].

6.4 High frequency dissipationless regime

We have so far discussed the solutions of the hydrodynamic equations in the low frequency limit. In the opposite limit $\omega \gg \omega_\perp^2 \tau$ of large frequencies viscosity and thermal conductivity can be ignored. Note that for isotropic trapping the hydrodynamic equations always reduce to the dissipationless regime if $\omega\tau \ll 1$. In this limit, still compatible with the condition $\omega \ll \omega_\perp$, the solutions are also affected by the presence of the radial confinement, but in a different way. In particular the fluctuations of the temperature and of the chemical potential are no longer independent of the radial coordinate, except in the superfluid region. Indeed in superfluids the fluctuations δT and $\delta\mu$ are independent of the radial coordinate as a consequence of the equations for $\mathbf{v}_s$ and for the radial mechanical equilibrium. This limit is still compatible with the usual hydrodynamical condition $\omega\tau \ll 1$ only if $\omega_\perp\tau \ll 1$, a condition which is rather severe from the experimental point of view.

An explicit and instructive solution in the dissipationless regime is available above T_C where the superfluid component is absent. We will consider the extreme regime of the ideal gas where all the thermodynamic quantities are known explicitly. In this limit the classical equations of hydrodynamics can be recast in the form of an equation for the velocity field [GWS97]:

$$-m\omega^2\mathbf{v} = \frac{5}{3}T\nabla[\nabla\cdot\mathbf{v}] - \nabla[\mathbf{v}\cdot\nabla U] - \frac{2}{3}[\nabla\cdot\mathbf{v}]\nabla U\ . \qquad (6.15)$$

Solutions of this equation for 3D harmonic traps were considered in [BC99] and [CG01]. The advantage of using 1D cylindrical configurations is due to the availability of plane wave solutions along the z direction, providing new physical insight on the effects of trapping on sound propagation. It was found in [NG98] that an exact solution of this equation in the presence of cylindrical radial trapping ($U = m\omega_\perp^2 r_\perp^2/2$) is given by $v_z \propto e^{\xi^2/5} e^{iqz}, v_\perp = 0$, where $\xi^2 = m\omega_\perp^2 r_\perp^2/T$, and is characterized by the adiabatic velocity of sound $mc_a^2 = 5T/3$. This solution is quite different from the one holding in the low frequency regime discussed in the first part of this Chapter where v_z does not depend on the radial coordinate. Also the temperature and the chemical potential fluctuations exhibit a strong radial dependence as a consequence of the radial trapping and the absence of thermal conductivity and viscosity. From the explicit knowledge of the velocity field and the orthogonality condition

$$\int \rho \mathbf{v}_{(i)}^* \cdot \mathbf{v}_{(j)} dxdy = 0 \ , \omega_i \neq \omega_j \ , \tag{6.16}$$

for the solutions of the HD equations [THL$^+$09], it is possible to calculate the contribution of the adiabatic sound to the dynamic response function. Using the expression $\rho \propto e^{-\xi^2/2}$ for the density distribution at equilibrium one obtains, after straightforward algebra, the result

$$\chi_a(q,\omega) = \frac{5}{9}\frac{\langle\rho\rangle}{m}\frac{q^2}{q^2c_a^2 - \omega^2} \ , \tag{6.17}$$

showing that the adiabatic mode does not exhaust the f-sum rule $\chi(\omega \to \infty) = -q^2\langle\rho\rangle/m\omega^2$, differently from the case of a uniform gas, and hence revealing that additional solutions of the hydrodynamic Eq. (6.15) should exist. This equation actually admits an additional class of low frequency solutions lying in the continuum and consequently exhibiting damping. On the $\omega - q$ plane these solutions occupy the region $\omega/q < \sqrt{24/25}c_a \equiv c_0$. The velocity field is given by the expressions

$$v_z = Ae^{\xi^2/4}\left[\sigma\cos(\sigma\xi^2) - \sin(\sigma\xi^2)/20\right]e^{iqz} \ , \tag{6.18}$$

where $\sigma = \sqrt{c_0^2q^2/\omega^2 - 1}/4$ is a continuous parameter, and

$$v_\perp = Be^{\xi^2/4}\sin(\sigma\xi^2)e^{iqz}/\xi \ , \tag{6.19}$$

with $B = -iA\sqrt{3/20}\left[(c_a^2q^2 - \omega^2)/qc_a\omega_\perp\right]$. We present here the result for the imaginary part of the dynamic response function in the region of the continuum

$$\mathrm{Im}\chi_c(q,\omega) = \frac{4}{3}\frac{\langle\rho\rangle}{mc_0^2}\frac{\omega\sqrt{c_0^2q^2 - \omega^2}}{c_a^2q^2 - \omega^2} \ . \tag{6.20}$$

It is easy to show that inclusion of the continuum allows for a complete fulfillment of both the compressibility and the f-sum rules. The function $\mathrm{Im}\chi_c$

exhibits a sharp maximum at $\omega/q \approx 0.98 c_0$. Thus the new excitation can be considered as the analog of second sound above T_C. It is worth emphasizing that the damping associated with the continuum is not a consequence of dissipative effects as happens in uniform fluids above T_C, but a result of the energy leakage from the gas due to the increase of the velocity field on large distances. The existence of a continuous spectrum of excitations and the value of the limiting velocity c_0 are universal properties holding also at lower temperatures, being fixed by the asymptotic behavior at large $r_\perp$ where the gas is classical and ideal.

We thank our collaborators H. Hu, E. Taylor and A. Griffin for important suggestions that led to our work, and P. Hohenberg, C. Salomon, H. Stoof and P. van der Straten for useful discussions. We also thank the authors of [BDM06, HLD10, NNJ$^+$10, THLG08] for providing us with tables of their results. Financial support from the EuroQUAM Fermix program and from MIUR PRIN is acknowledged.

Chapter 7

Conclusion

In conclusion we have applied quantum Monte Carlo methods, Density Functional Theory in the local density approximation and the Hydrodynamic theory of superfluids to the study of various physical problems related to the BCS-BEC crossover.

We have studied the problem of itinerant ferromagnetism in $3D$ Fermi gases near a Feshbach resonance, finding strong evidence of a quantum phase transition. Future perspectives include an analogous study of the two dimensional problem and a better characterization and optimization of the upper branch of the BCS-BEC crossover.

We have studied the problem of the $2D$ BCS-BEC crossover, paving the way for even more accurate studies of the strongly interacting regime. An interesting further study will consider the polarized system, where the roles of the normal phase, the homogeneous polarized superfluid phase and the Fulde-Ferrel-Larkin-Ovchinnikov phase are still under debate.

We have studied the density profiles of polarized Fermi gases in the $3D$ BCS-BEC crossover, assuming local density approximation. An analogous study in two dimensions will require more precise equations of state and an accurate study of the quasi-$2D$ realistic conditions.

Finally, we have studied sound propagation in a cylindrically trapped Fermi gas at unitarity, with particular emphasis on the role of viscosity. Further work will consider more realistic harmonically trapped configurations.

Appendix A

Estimation of the correlation length and the variance

Let us consider N iterations of a stochastic process that produces a series of random values for the observable of interest Y_x, where x is the index of the iteration, distributed according to some unknown probability distribution, with mean $E[Y]$ and variance σ^2. After a transient time, we can estimate the mean with $E[Y] \approx \langle\langle Y_x \rangle\rangle = \frac{1}{N}\sum_x Y_x$, where $\langle\langle \cdots \rangle\rangle$ indicates the average over all the iterations. Thanks to the central limit theorem is is also possible to estimate the error of the estimator of the mean. Actually one can divide the series into n blocks with $M = N/n$ iterations each and calculate the estimator of the mean for each block i, $E[Y]_i \approx \langle Y_x \rangle_i = \frac{1}{M}\sum_{x\in i} Y_x$, where $\langle \cdots \rangle_i$ indicates the average over the iterations in the block i: if M is sufficiently large and the Y_x are independent, whatever their distribution, then the $\langle Y_x \rangle_i$ are distributed with a Gaussian, with mean $E[Y]$ and variance $\sigma^2_{\langle Y\rangle} = \sigma^2_Y/M = n\sigma^2_Y/N$. We are interested to find the highest accuracy, so we want to estimate σ^2_Y/N which would correspond to the maximum length block. Then one obtains the simple relation $\sigma^2_Y/N = \sigma^2_{\langle Y\rangle}/n$; the right-hand-side can be estimated using $\sigma^2_{\langle Y\rangle} \approx \frac{1}{n-1}\sum_i^n (\langle Y\rangle_i - \langle\langle Y\rangle\rangle)^2$. By plotting $\sigma^2_{\langle Y\rangle}/n$ with varying length of the blocks, one should reach a constant value which provides our estimate of the (square) error. Notice that this is not the same as using $\sigma^2_Y/N \approx \frac{1}{N(N-1)}\sum_x^N (Y_x - \langle\langle Y\rangle\rangle)^2$, since this relation is not valid if the Y_x are correlated, and it underestimates the variance. So one expects that $\sigma^2_{\langle Y\rangle}/n$ goes to the previous wrong estimate for $M \to 0$, then increases up to a steady value, after $M \approx M_C$, then possibly decreases again if M is too large and there are too few blocks (See Fig. A.1). The value M_C indicates the correlation length, after which both the correlation effects have disappeared and the central limit theorem starts to be valid.

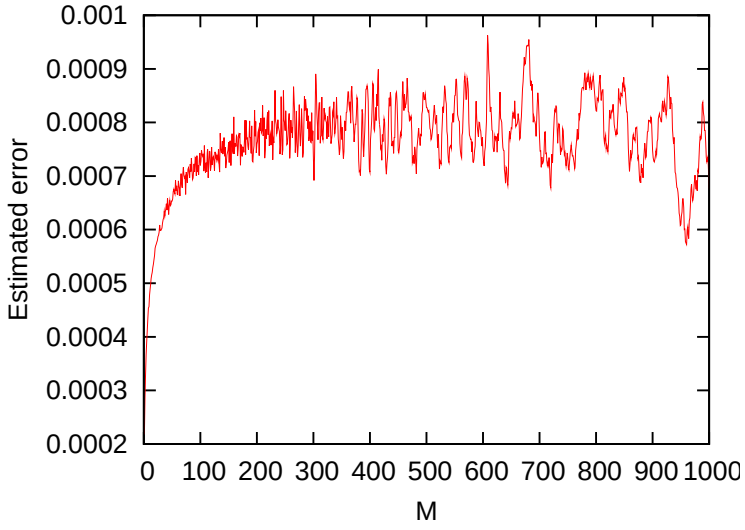

Figure A.1: Example of error estimated with the standard deviation of the block averages as explained in the text (arb. units). M is the length of the blocks. In this case we would set $Error = 0.001$, and we would notice that the correlation length is $M \approx 200$.

Appendix B

Metropolis accept-reject step in the DMC algorithm

In this Appendix we discuss the role of the accept-reject step (ARS) in the Diffusion Monte Carlo algorithm with importance sampling (Sec. 2.5). An interesting methodological and historical introduction to Markov processes in Monte Carlo simulations, including DMC, can be found in [Cep03]. The ARS in DMC has been used and discussed by many authors, see for example [Rey82, UNR93, FMNR01]. A comparison between DMC algorithms with the ARS and higher order algorithms without the ARS can be found in [FC01, SBC02].

Let us recall the Green's functions G_0 and G for the original and for the importance sampled imaginary time Schroedinger equations respectively:

$$G_0(\boldsymbol{R} \to \boldsymbol{R'}, d\tau) = \langle \boldsymbol{R'}|e^{-d\tau \hat{H}}|\boldsymbol{R}\rangle \tag{B.1}$$

$$G(\boldsymbol{R} \to \boldsymbol{R'}, d\tau) = \langle \boldsymbol{R'}|e^{-d\tau (\hat{K}+\hat{F}+E_L(\boldsymbol{R}))}|\boldsymbol{R}\rangle \ . \tag{B.2}$$

See Sec. 2.5 for the definitions of the operators, which are not essential here. For clearness we have set the reference energy $E_{ref} = 0$. By considering the corresponding integral equations (Eqs. (2.24) and (2.39)) it is easy to show that the relation between the two Green's functions is

$$G(\boldsymbol{R} \to \boldsymbol{R'}, d\tau) = G_0(\boldsymbol{R} \to \boldsymbol{R'}, d\tau)\frac{\psi_T(\boldsymbol{R'})}{\psi_T(\boldsymbol{R})} \ . \tag{B.3}$$

Since $G_0(\boldsymbol{R'} \to \boldsymbol{R}, d\tau) = G_0(\boldsymbol{R} \to \boldsymbol{R'}, d\tau)$ due to the hermiticity of the hamiltonian, from the previous equation it is immediate to derive

$$|\psi_T(\boldsymbol{R'})|^2 G(\boldsymbol{R'} \to \boldsymbol{R}, d\tau) = |\psi_T(\boldsymbol{R})|^2 G(\boldsymbol{R} \to \boldsymbol{R'}, d\tau) \tag{B.4}$$

which can be interpreted as a sort of detailed balance for DMC, analogous to condition (2.10) holding for reversible Markov chains. We remark however

that ψ_T is not the distribution that we want to sample and that G is not the transition matrix of a Markov chain since it is not normalized.

However, since Eq. (B.4) is exact for any $d\tau$, one could try to enforce it in the algorithm, in order to improve the time step dependence of energy. Given an approximation T for the Green's function, for example the linear one (2.44), one can introduce a new (not normalized) transition matrix $\tilde{G} = T \cdot A$ where A is an accept-reject probability such that condition (B.4) is fulfilled. Since the detailed balance condition can thus be written as

$$A(\boldsymbol{R} \to \boldsymbol{R'}, d\tau) = \frac{|\psi_T(\boldsymbol{R'})|^2 T(\boldsymbol{R'} \to \boldsymbol{R}, d\tau)}{|\psi_T(\boldsymbol{R})|^2 T(\boldsymbol{R} \to \boldsymbol{R'}, d\tau)} A(\boldsymbol{R'} \to \boldsymbol{R}, d\tau) \ , \tag{B.5}$$

then the acceptance probability is a function of the expression $\chi(\boldsymbol{R} \to \boldsymbol{R'}, d\tau) = \frac{|\psi_T(\boldsymbol{R'})|^2 T(\boldsymbol{R'} \to \boldsymbol{R}, d\tau)}{|\psi_T(\boldsymbol{R})|^2 T(\boldsymbol{R} \to \boldsymbol{R'}, d\tau)}$ only, such that the former equality turns into

$$\frac{1}{\chi} A(\chi) = A\left(\frac{1}{\chi}\right) \ . \tag{B.6}$$

A possible choice for A is the one of the Metropolis algorithm, that is

$$A(\boldsymbol{R} \to \boldsymbol{R'}, d\tau) = \min\left(1, \frac{|\psi_T(\boldsymbol{R'})|^2 T(\boldsymbol{R'} \to \boldsymbol{R}, d\tau)}{|\psi_T(\boldsymbol{R})|^2 T(\boldsymbol{R} \to \boldsymbol{R'}, d\tau)}\right) . \tag{B.7}$$

If the acceptance probability is 1, then the approximate T is used, which is correct up to first order in $d\tau$. If it less than one then the accept-reject step changes $\tilde{G}$ with respect to T so that it is no more a correct approximation of G at first order. In the end, adding the ARS results in changing the dependence of the estimated energy and observables on the time step, in a not completely predictable way. However two limiting cases are correctly preserved, that is the $d\tau \to 0$ limit, when one has unity acceptance, and the $\psi_T \to \varphi_0$ limit, when the algorithm turns into Smart Monte Carlo (Sec. 2.3.1), with constant population since the trial wavefunction is exact.

In general, provided the trial wavefunction is good, one could expect a less steep dependence of energy on the time step, so that higher time steps can be used, thus reducing the convergence time. However, to our knowledge, there is no systematic way of predicting the time step behavior once the ARS is used. An advantage with respect to the DMC algorithm without ARS is that moves towards regions with small wavefunction are rejected, thus forcing the avoidance of regions where the drift term is not correctly treated (see Sec. 2.5). Actually in the standard DMC one usually introduces a cutoff in the drift term in order to avoid divergences near the nodal surfaces.

In conclusion the choice between the two methods depends on the specific problem.

Appendix C

Calculation of Forces and Kinetic energy for the Jastrow function

The general (two-body) Jastrow function is:

$$\Psi_J(\boldsymbol{R}) = J_{\uparrow\uparrow}(\boldsymbol{R})J_{\downarrow\downarrow}(\boldsymbol{R})J_{\uparrow\downarrow}(\boldsymbol{R}) = \prod_{i<j} f_{\uparrow\uparrow}(r_{ij}) \prod_{a<b} f_{\downarrow\downarrow}(r_{ab}) \prod_{i,a} f_{\uparrow\downarrow}(r_{ia}) \,, \tag{C.1}$$

where the indexes i, j refer to the $\uparrow$ particles and the indexes a, b refer to the $\downarrow$ particles. The quantum forces $F^{\alpha}_{i,a}$, where the index $\alpha = x, y, z$ refer to the spatial coordinate, reduce to:

$$\begin{aligned}
F^{\alpha}_{i} &= 2\frac{\partial_{\alpha_i}\Psi_J}{\Psi_J} = F^{\alpha}_{\uparrow\uparrow i} + F^{\alpha}_{\uparrow\downarrow i} \,; \\
F^{\alpha}_{a} &= 2\frac{\partial_{\alpha_a}\Psi_J}{\Psi_J} = F^{\alpha}_{\downarrow\downarrow a} + F^{\alpha}_{\uparrow\downarrow a} \,; \\
F^{\alpha}_{\uparrow\uparrow i} &= 2\frac{\partial_{\alpha_i}J_{\uparrow\uparrow}}{J_{\uparrow\uparrow}} = 2\sum_{j\neq i}\frac{\partial_{\alpha_i}f_{\uparrow\uparrow}(r_{ij})}{f_{\uparrow\uparrow}(r_{ij})} = 2\sum_{j\neq i}\frac{f'_{\uparrow\uparrow}(r_{ij})}{f_{\uparrow\uparrow}(r_{ij})}\frac{\alpha_i-\alpha_j}{r_{ij}} \,; \\
F^{\alpha}_{\downarrow\downarrow a} &= 2\frac{\partial_{\alpha_a}J_{\downarrow\downarrow}}{J_{\downarrow\downarrow}} = 2\sum_{b\neq a}\frac{\partial_{\alpha_a}f_{\downarrow\downarrow}(r_{ab})}{f_{\downarrow\downarrow}(r_{ab})} = 2\sum_{b\neq a}\frac{f'_{\downarrow\downarrow}(r_{ab})}{f_{\downarrow\downarrow}(r_{ab})}\frac{\alpha_a-\alpha_b}{r_{ab}} \,; \\
F^{\alpha}_{\uparrow\downarrow i} &= 2\frac{\partial_{\alpha_i}J_{\uparrow\downarrow}}{J_{\uparrow\downarrow}} = 2\sum_{a}\frac{\partial_{\alpha_i}f_{\uparrow\downarrow}(r_{ia})}{f_{\uparrow\downarrow}(r_{ia})} = 2\sum_{a}\frac{f'_{\uparrow\downarrow}(r_{ia})}{f_{\uparrow\downarrow}(r_{ia})}\frac{\alpha_i-\alpha_a}{r_{ia}} \,; \\
F^{\alpha}_{\uparrow\downarrow a} &= 2\frac{\partial_{\alpha_a}J_{\uparrow\downarrow}}{J_{\uparrow\downarrow}} = 2\sum_{i}\frac{\partial_{\alpha_a}f_{\uparrow\downarrow}(r_{ia})}{f_{\uparrow\downarrow}(r_{ia})} = -2\sum_{i}\frac{f'_{\uparrow\downarrow}(r_{ia})}{f_{\uparrow\downarrow}(r_{ia})}\frac{\alpha_i-\alpha_a}{r_{ia}} \,.
\end{aligned} \tag{C.2}$$

Let us now calculate the kinetic energy:

$$\begin{aligned}
K =& -\frac{D}{\Psi_J}\left\{\sum_i\sum_\alpha^d \partial^2_{\alpha_i}\Psi_J + \sum_a\sum_\alpha^d \partial^2_{\alpha_a}\Psi_J\right\} \\
=& -D\left\{\sum_i\sum_\alpha^d\left[\frac{\partial^2_{\alpha_i}J_{\uparrow\uparrow}}{J_{\uparrow\uparrow}} + \frac{\partial^2_{\alpha_i}J_{\uparrow\downarrow}}{J_{\uparrow\downarrow}} + 2\frac{\partial_{\alpha_i}J_{\uparrow\uparrow}}{J_{\uparrow\uparrow}}\frac{\partial_{\alpha_i}J_{\uparrow\downarrow}}{J_{\uparrow\downarrow}}\right]\right. \\
&\left. + \sum_a\sum_\alpha^d\left[\frac{\partial^2_{\alpha_a}J_{\downarrow\downarrow}}{J_{\downarrow\downarrow}} + \frac{\partial^2_{\alpha_a}J_{\uparrow\downarrow}}{J_{\uparrow\downarrow}} + 2\frac{\partial_{\alpha_a}J_{\downarrow\downarrow}}{J_{\downarrow\downarrow}}\frac{\partial_{\alpha_a}J_{\uparrow\downarrow}}{J_{\uparrow\downarrow}}\right]\right\} \\
=& K_{\uparrow\uparrow} + K_{\downarrow\downarrow} + K_{\uparrow\downarrow} - \frac{D}{2}\boldsymbol{F}_S\cdot\boldsymbol{F}_A\,, \qquad \text{(C.3)}
\end{aligned}$$

where we have defined the global force vectors as $\boldsymbol{F}_S = \{F^\alpha_{\uparrow\uparrow i}, F^\alpha_{\downarrow\downarrow a}\}$ and $\boldsymbol{F}_A = \{F^\alpha_{\uparrow\downarrow i}, F^\alpha_{\uparrow\downarrow a}\}$ and the other contributions are:

$$\begin{aligned}
K_{\uparrow\uparrow} =& -D\sum_i\sum_\alpha^d \frac{\partial^2_{\alpha_i}J_{\uparrow\uparrow}}{J_{\uparrow\uparrow}} = -D\sum_i\sum_\alpha^d \frac{\partial_{\alpha_i}\left(J_{\uparrow\uparrow}\sum_{j\neq i}\frac{f'_{\uparrow\uparrow}(r_{ij})}{f_{\uparrow\uparrow}(r_{ij})}\frac{\alpha_i-\alpha_j}{r_{ij}}\right)}{J_{\uparrow\uparrow}} \\
=& -\frac{D}{4}\sum_i\sum_\alpha^d (F^\alpha_{\uparrow\uparrow i})^2 - D\sum_{i,j\neq i}\sum_\alpha^d\left[\left(\frac{f''_{\uparrow\uparrow}(r_{ij})}{f_{\uparrow\uparrow}(r_{ij})} - \left(\frac{f'_{\uparrow\uparrow}(r_{ij})}{f_{\uparrow\uparrow}(r_{ij})}\right)^2\right)\frac{(\alpha_i-\alpha_j)^2}{r_{ij}^2}\right. \\
&\left. + \frac{f'_{\uparrow\uparrow}(r_{ij})}{f_{\uparrow\uparrow}(r_{ij})}\left(\frac{1}{r_{ij}} - \frac{(\alpha_i-\alpha_j)^2}{r_{ij}^3}\right)\right] \\
=& -\frac{D}{4}\boldsymbol{F}_{\uparrow\uparrow}\cdot\boldsymbol{F}_{\uparrow\uparrow} - D\sum_{i,j\neq i}\left[\frac{f''_{\uparrow\uparrow}(r_{ij})}{f_{\uparrow\uparrow}(r_{ij})} - \left(\frac{f'_{\uparrow\uparrow}(r_{ij})}{f_{\uparrow\uparrow}(r_{ij})}\right)^2 + \frac{d-1}{r_{ij}}\frac{f'_{\uparrow\uparrow}(r_{ij})}{f_{\uparrow\uparrow}(r_{ij})}\right] \\
=& -\frac{D}{4}\boldsymbol{F}_{\uparrow\uparrow}\cdot\boldsymbol{F}_{\uparrow\uparrow} + D\sum_{i,j\neq i}\left[e^L_{\uparrow\uparrow}(r_{ij}) + \left(\frac{f'_{\uparrow\uparrow}(r_{ij})}{f_{\uparrow\uparrow}(r_{ij})}\right)^2\right]\,; \\
K_{\downarrow\downarrow} =& -D\sum_a\sum_\alpha^d \frac{\partial^2_{\alpha_a}J_{\downarrow\downarrow}}{J_{\downarrow\downarrow}} \\
=& -\frac{D}{4}\boldsymbol{F}_{\downarrow\downarrow}\cdot\boldsymbol{F}_{\downarrow\downarrow} + D\sum_{a,b\neq a}\left[e^L_{\downarrow\downarrow}(r_{ab}) + \left(\frac{f'_{\downarrow\downarrow}(r_{ab})}{f_{\downarrow\downarrow}(r_{ab})}\right)^2\right]\,; \\
K_{\uparrow\downarrow} =& -D\sum_i\sum_\alpha^d \frac{\partial^2_{\alpha_i}J_{\uparrow\downarrow}}{J_{\uparrow\downarrow}} - D\sum_a\sum_\alpha^d \frac{\partial^2_{\alpha_a}J_{\uparrow\downarrow}}{J_{\uparrow\downarrow}} \\
=& -\frac{D}{4}\boldsymbol{F}_A\cdot\boldsymbol{F}_A + 2D\sum_{i,a}\left[e^L_{\uparrow\downarrow}(r_{ia}) + \left(\frac{f'_{\uparrow\downarrow}(r_{ia})}{f_{\uparrow\downarrow}(r_{ia})}\right)^2\right]\,, \qquad \text{(C.4)}
\end{aligned}$$

where $e^L = -(f'' + (d-1)f'/r)/f$ is the local kinetic energy of the two-body problem in units of $2D$. In the end the local kinetic energy of a Jastrow

wavefunction is

$$K^J = 2D \sum_{i<j} \left[e^L_{\uparrow\uparrow}(r_{ij}) + \left(\frac{f'_{\uparrow\uparrow}(r_{ij})}{f_{\uparrow\uparrow}(r_{ij})} \right)^2 \right] +$$
$$2D \sum_{a<b} \left[e^L_{\downarrow\downarrow}(r_{ab}) + \left(\frac{f'_{\downarrow\downarrow}(r_{ab})}{f_{\downarrow\downarrow}(r_{ab})} \right)^2 \right] + 2D \sum_{i,a} \left[e^L_{\uparrow\downarrow}(r_{ia}) + \left(\frac{f'_{\uparrow\downarrow}(r_{ia})}{f_{\uparrow\downarrow}(r_{ia})} \right)^2 \right]$$
$$- \frac{D}{4} \left(\boldsymbol{F}_S \cdot \boldsymbol{F}_S + \boldsymbol{F}_A \cdot \boldsymbol{F}_A + 2\boldsymbol{F}_S \cdot \boldsymbol{F}_A \right) . \quad \text{(C.5)}$$

Bibliography

[ABC+09] G. Astrakharchik, J. Boronat, J Casulleras, I. Kurbakov, and Y. Lozovik. Equation of state of a weakly interacting two-dimensional Bose gas studied at zero temperature by means of quantum Monte Carlo methods. *Physical Review A*, 79(5):051602(R), May 2009. 4.3.3, 4.5

[ABCG04] G. Astrakharchik, J. Boronat, J. Casulleras, and S. Giorgini. Equation of State of a Fermi Gas in the BEC-BCS Crossover: A Quantum Monte Carlo Study. *Physical Review Letters*, 93(20):200404, November 2004. 1.3, 2.7, 2.7.2, 2.7.3, 2.7.3, 4.1

[ABCG05] G. Astrakharchik, J. Boronat, J. Casulleras, and S. Giorgini. Momentum Distribution and Condensate Fraction of a Fermion Gas in the BCS-BEC Crossover. *Physical Review Letters*, 95(23):230405, December 2005. 4.4

[ACK00] R. Assaraf, M. Caffarel, and A. Khelif. Diffusion Monte Carlo methods with a fixed number of walkers. *Physical Review E*, 61(4):4566, April 2000. 2.4

[AEM+95] M.H. Anderson, J.R. Ensher, M.R. Matthews, C.E. Wieman, and E.A. Cornell. Observation of Bose-Einstein Condensation in a Dilute Atomic Vapor. *Science (New York, N.Y.)*, 269(5221):198, July 1995. 1.1

[AK59] A.A. Abrikosov and I.M. Khalatnikov. The theory of a fermi liquid (the properties of liquid 3He at low temperatures). *Reports on Progress in Physics*, 22(1):329, January 1959. 2.7.2

[AKM+97] M.R. Andrews, D.M. Kurn, H.-J. Miesner, D.S. Durfee, C. Townsend, S. Inouye, and W. Ketterle. Propagation of Sound in a Bose-Einstein Condensate. *Physical Review Letters*, 79(4):553, July 1997. 6.1

[AMMT00] M. Amoruso, I. Meccoli, A. Minguzzi, and M.P. Tosi. Density profiles and collective excitations of a trapped two-component

Fermi vapour. *The European Physical Journal D - Atomic, Molecular, Optical and Plasma Physics*, 8(3):361, 2000. 3.1

[AN09] E. Arahata and T. Nikuni. Propagation of second sound in a superfluid Fermi gas in the unitary limit. *Physical Review A*, 80(4):043613, October 2009. 6.2

[And75] J.B. Anderson. A random-walk simulation of the Schrödinger equation: H_3^+. *The Journal of Chemical Physics*, 63(4):1499, 1975. 2, 2.4

[And76] J.B. Anderson. Quantum chemistry by random walk. $H\ ^2P$, $H_3^+\ D_{3h}\ ^1A_1'$, $H_2\ ^3\Sigma_u^+$, $H_4\ ^1\Sigma_g^+$, $Be\ ^1S$. *The Journal of Chemical Physics*, 65(10):4121, 1976. 2.4

[ARK+07] A. Altmeyer, S. Riedl, C. Kohstall, M. Wright, R. Geursen, M. Bartenstein, C. Chin, J. Denschlag, and R. Grimm. Precision Measurements of Collective Oscillations in the BEC-BCS Crossover. *Physical Review Letters*, 98(4):040401, January 2007. 4.1

[Atk59] K. Atkins. Third and Fourth Sound in Liquid Helium II. *Physical Review*, 113(4):962, February 1959. 6.1

[BAR+04] M. Bartenstein, A. Altmeyer, S. Riedl, S. Jochim, C. Chin, J. Denschlag, and R. Grimm. Crossover from a Molecular Bose-Einstein Condensate to a Degenerate Fermi Gas. *Physical Review Letters*, 92(12):120401, March 2004. 1.1

[BC94] J. Boronat and J. Casulleras. Monte Carlo analysis of an interatomic potential for He. *Physical Review B*, 49(13):8920, April 1994. 2.5.1

[BC96] M. Boninsegni and D.M. Ceperley. Density fluctuations in liquid ^4He. Path integrals and maximum entropy. *Journal of Low Temperature Physics*, 104(5-6):339, September 1996. 2.3

[BC99] G. Bruun and C. Clark. Hydrodynamic Excitations of Trapped Fermi Gases. *Physical Review Letters*, 83(26):5415, December 1999. 6.4

[BCS57] J. Bardeen, L.N. Cooper, and J.R. Schrieffer. Theory of Superconductivity. *Physical Review*, 108(5):1175, December 1957. 1.2, 2.7.3

[BDM06] A. Bulgac, J.E. Drut, and P. Magierski. Spin 1/2 Fermions in the Unitary Regime: A Superfluid of a New Type. *Physical Review Letters*, 96(9):090404, March 2006. 6.3, 6.4

[BDZ08] I. Bloch, J. Dalibard, and W. Zwerger. Many-body physics with ultracold gases. *Reviews of Modern Physics*, 80(3):885, July 2008. 1.1, 4.1

[Bea10] S.R. Beane. Ground state energy of the interacting Bose gas in two dimensions: an explicit construction. *arxiv*, 1002.3815, February 2010. 4.3.3, 4.5

[BF07] A. Bulgac and M. Forbes. Zero-temperature thermodynamics of asymmetric Fermi gases at unitarity. *Physical Review A*, 75(3):031605(R), March 2007. 5.2

[BG09] G. Bertaina and S. Giorgini. Density profiles of polarized Fermi gases confined in harmonic traps. *Physical Review A*, 79(1):013616, January 2009. 1, 5

[BG10] G. Bertaina and S. Giorgini. BCS-BEC crossover in a two-dimensional Fermi gas. *arxiv*, 1011.3737, November 2010. 1, 4

[BGL88] J.P. Bouchaud, A. Georges, and C. Lhuillier. Pair wave functions for strongly correlated fermions and their determinantal representation. *Journal de Physique*, 49(4):553, 1988. 2.7, 2.7.3, 2.7.3, 2.7.4, 4.4

[BKC+04] T. Bourdel, L. Khaykovich, J. Cubizolles, J. Zhang, F. Chevy, M. Teichmann, L. Tarruell, S. Kokkelmans, and C. Salomon. Experimental Study of the BEC-BCS Crossover Region in Lithium 6. *Physical Review Letters*, 93(5):050401, July 2004. 1.1

[BKV99] D. Belitz, T. Kirkpatrick, and T. Vojta. First Order Transitions and Multicritical Points in Weak Itinerant Ferromagnets. *Physical Review Letters*, 82(23):4707, June 1999. 3.1

[Blo75] P. Bloom. Two-dimensional Fermi gas. *Physical Review B*, 12(1):125, July 1975. 4.3.2

[BM58] G.E.P. Box and M.E. Muller. A Note on the Generation of Random Normal Deviates. *The Annals of Mathematical Statistics*, 29(2):610, 1958. 2.1

[BMWS08] M. Bajdich, L. Mitas, L. Wagner, and K. Schmidt. Pfaffian pairing and backflow wavefunctions for electronic structure quantum Monte Carlo methods. *Physical Review B*, 77(11):115112, March 2008. 2.7.2, 2.7.3

[Bor02] J. Boronat. *Monte Carlo simulations at zero temperature: Helum in one, two and three dimensions.*, chapter 2. World Scientific Publishing Co. Pte. Ltd., 2002. 2.4

[Bos24] S. Bose. Plancks Gesetz und Lichtquantenhypothese. *Z. Phys.*, 26(3):178, 1924. 1.2

[BP35] H. Bethe and R. Peierls. Quantum Theory of the Diplon. *Proceedings of the Royal Society A: Mathematical, Physical and Engineering Sciences*, 148(863):146, January 1935. 1.4

[BP91] G. Baym and C.J. Pethick. *Landau Fermi-Liquid Theory.* John Wiley, New York, 1991. 5.2

[BPS10] G. Bertaina, L. Pitaevskii, and S. Stringari. First and Second Sound in Cylindrically Trapped Gases. *Physical Review Letters*, 105(15):150402, October 2010. 1, 6

[BSTH95] C. Bradley, C. Sackett, J. Tollett, and R. Hulet. Evidence of Bose-Einstein Condensation in an Atomic Gas with Attractive Interactions. *Physical Review Letters*, 75(9):1687, August 1995. 1.1

[CA80] D.M. Ceperley and B.J. Alder. Ground State of the Electron Gas by a Stochastic Method. *Physical Review Letters*, 45(7):566, August 1980. 2, 2.6

[CA84] D.M. Ceperley and B.J. Alder. Quantum Monte Carlo for molecules: Green's function and nodal release. *The Journal of Chemical Physics*, 81(12):5833, 1984. 2.6

[CB88] D.M. Ceperley and B. Bernu. The calculation of excited state properties with quantum Monte Carlo. *The Journal of Chemical Physics*, 89(10):6316, 1988. 2.6

[CB00] J. Casulleras and J. Boronat. Progress in Monte Carlo Calculations of Fermi Systems: Normal Liquid ^3He. *Physical Review Letters*, 84(14):3121, April 2000. 2.5.1

[CCHL07] C.-C. Chien, Q. Chen, Y. He, and K. Levin. Superfluid Phase Diagrams of Trapped Fermi Gases with Population Imbalance. *Physical Review Letters*, 98(11):110404, March 2007. 5.1

[CCK77] D. Ceperley, G.V. Chester, and M.H. Kalos. Monte Carlo simulation of a many-fermion study. *Physical Review B*, 16(7):3081, October 1977. 2.3, 2.3.1, 2.3.1, 2.5, 2.7

[CCPS03] J. Carlson, S.-Y. Chang, V.R. Pandharipande, and K.E. Schmidt. Superfluid Fermi Gases with Large Scattering Length. *Physical Review Letters*, 91(5):050401, July 2003. 2.7, 2.7.3, 2.7.3, 2.7.4, 4.5

[CCS08] G. Conduit, P. Conlon, and B. Simons. Superfluidity at the BEC-BCS crossover in two-dimensional Fermi gases with population and mass imbalance. *Physical Review A*, 77(5):053617, May 2008. 4.1

[Cep03] D.M. Ceperley. Metropolis Methods for Quantum Monte Carlo Simulations. In *AIP Conference Proceedings*, number 1, page 85. AIP, 2003. 2.3, B

[CFH+98] P. Courteille, R.S. Freeland, D.J. Heinzen, F.A. van Abeelen, and B.J. Verhaar. Observation of a Feshbach Resonance in Cold Atom Scattering. *Physical Review Letters*, 81(1):69, 1998. 1.3

[CG95] S. Chib and E. Greenberg. Understanding the Metropolis-Hastings Algorithm. *The American Statistician*, 49(4):327, 1995. 2

[CG01] A. Csordás and R. Graham. Finite-temperature hydrodynamic modes of trapped quantum gases. *Physical Review A*, 64(1):13619, June 2001. 6.4

[CGJT10] C. Chin, R. Grimm, P. Julienne, and E. Tiesinga. Feshbach resonances in ultracold gases. *Reviews of Modern Physics*, 82(2):1225, April 2010. 1.2

[CGS09] G.J. Conduit, A.G. Green, and B.D. Simons. Inhomogeneous Phase Formation on the Border of Itinerant Ferromagnetism. *Physical Review Letters*, 103(20):207201, November 2009. 3.1, 3.3

[Che06] F. Chevy. Universal phase diagram of a strongly interacting Fermi gas with unbalanced spin populations. *Physical Review A*, 74(6):063628, December 2006. 5.2

[Chi90] S. Chin. Quadratic diffusion Monte Carlo algorithms for solving atomic many-body problems. *Physical Review A*, 42(12):6991, December 1990. 2.5.1

[CKL81] D. Ceperley, M.H. Kalos, and J.L. Lebowitz. The Computer Simulation of the Static and Dynamic Properties of a Polymer Chain. *Macromolecules*, (14):1472, 1981. 2.3.1, 2.5

[CPCS04] S. Chang, V. Pandharipande, J. Carlson, and K. Schmidt. Quantum Monte Carlo studies of superfluid Fermi gases. *Physical Review A*, 70(4):043602, October 2004. 4.4

[CRLC07] R. Combescot, A. Recati, C. Lobo, and F. Chevy. Normal State of Highly Polarized Fermi Gases: Simple Many-Body Approaches. *Physical Review Letters*, 98(18):180402, May 2007. 5.2

[CRT10] S.-Y. Chang, M. Randeria, and N. Trivedi. Ferromagnetism in repulsive Fermi gases: upper branch of Feshbach resonance versus hard spheres. *arxiv*, 1004.2680, April 2010. 3.4

[CSL05] Q. Chen, J. Stajic, and K. Levin. Thermodynamics of Interacting Fermions in Atomic Traps. *Physical Review Letters*, 95(26):260405, December 2005. 6.3

[CVFT06] P. Capuzzi, P. Vignolo, F. Federici, and M. Tosi. Sound propagation in elongated superfluid fermionic clouds. *Physical Review A*, 73(2):021603, February 2006. 6.2

[CZ10] X. Cui and H. Zhai. Stability of a fully magnetized ferromagnetic state in repulsively interacting ultracold Fermi gases. *Physical Review A*, 81(4):041602, April 2010. 3.3

[De 66] P.G. De Gennes. *Superconductivity of Metals and Alloys*. W. A. Benjamin, Inc., New York, 1966. 1.1

[DGS99] F. Dalfovo, S. Giorgini, and S. Stringari. Theory of Bose-Einstein condensation in trapped gases. *Reviews of Modern Physics*, 71(3):463, April 1999. 1.1

[DM05] R. Duine and A. MacDonald. Itinerant Ferromagnetism in an Ultracold Atom Fermi Gas. *Physical Review Letters*, 95(23):230403, November 2005. 3.1

[DMA+95] K. Davis, M. Mewes, M. Andrews, N. van Druten, D. Durfee, D. Kurn, and W. Ketterle. Bose-Einstein Condensation in a Gas of Sodium Atoms. *Physical Review Letters*, 75(22):3969, November 1995. 1.1

[Ein25] A. Einstein. Quantentheorie des einatomigen idealen Gases. Zweite Abhandlung. *Sitzungber. Preuss. Akad. Wiss.*, page 3, 1925. 1.2

[ER92] J. Engelbrecht and M. Randeria. Low-density repulsive Fermi gas in two dimensions: Bound-pair excitations and Fermi-liquid behavior. *Physical Review B*, 45(21):12419, June 1992. 4.3.2

[ERZ92] J.R. Engelbrecht, M. Randeria, and L. Zhang. Landau f function for the dilute Fermi gas in two dimensions. *Physical Review B*, 45(17):10135, May 1992. 4.3.2, 4.5

[FC01] H. Forbert and S. Chin. Fourth-order diffusion Monte Carlo algorithms for solving quantum many-body problems. *Physical Review B*, 63(14):144518, March 2001. 2.5.1, B

[FMNR01] W. Foulkes, L Mitas, R. Needs, and G. Rajagopal. Quantum Monte Carlo simulations of solids. *Reviews of Modern Physics*, 73(1):33, January 2001. 2.4, B

[FOTG07] N. Fukushima, Y. Ohashi, E. Taylor, and A. Griffin. Superfluid density and condensate fraction in the BCS-BEC crossover regime at finite temperatures. *Physical Review A*, 75(3):033609, March 2007. 6.3

[GBC99] S. Giorgini, J. Boronat, and J. Casulleras. Ground state of a homogeneous Bose gas: A diffusion Monte Carlo calculation. *Physical Review A*, 60(6):5129, December 1999. 2.5.1, 2.2, 2.7

[GBC02] V. Grau, J. Boronat, and J. Casulleras. Zero-Temperature Equation of State of Two-Dimensional ^3He. *Physical Review Letters*, 89(4):045301, July 2002. 2.7.2

[Geo07] A. Georges. Ultracold Fermi Gases. In W. Ketterle, M. Inguscio, and C. Salomon, editors, *Proceedings of the Varenna "Enrico Fermi" Summer School, Course CLXIV*, Bologna, 2007. Società Italiana di Fisica. 3.1

[GKG+04] K. Góral, T. Köhler, S.A. Gardiner, E. Tiesinga, and P.S. Julienne. Adiabatic association of ultracold molecules via magnetic-field tunable interactions. *Journal of Physics B: Atomic, Molecular and Optical Physics*, 37(17):3457, September 2004. 1.2

[GPS08] S. Giorgini, L. Pitaevskii, and S. Stringari. Theory of ultracold atomic Fermi gases. *Reviews of Modern Physics*, 80(4):1215, October 2008. 1.1, 3.1, 4.1, 5.1, 6.3

[Gro61] E.P. Gross. Structure of a quantized vortex in boson systems. *Il Nuovo Cimento*, 20(3):454, May 1961. 1.1

[Gua98] R. Guardiola. *Monte Carlo methods in quantum many-body theories*, page 269. Springer, 1998. 2.4, 2.4

[GWS97] A. Griffin, W.-C. Wu, and S. Stringari. Hydrodynamic Modes in a Trapped Bose Gas above the Bose-Einstein Transition. *Physical Review Letters*, 78(10):1838, March 1997. 6.4

[Has70] W.K. Hastings. Monte Carlo Sampling Methods Using Markov Chains and Their Applications. *Biometrika*, 57(1):97, 1970. 2, 2.2

[HCCL07] Y. He, Q. Chen, C.-C. Chien, and K. Levin. First- and second-sound-like modes at finite temperature in trapped Fermi gases from BCS to BEC. *Physical Review A*, 76(5):051602, November 2007. 6.1

[HFS+97] M. Houbiers, R. Ferwerda, H. Stoof, W. McAlexander, C. Sackett, and R. Hulet. Superfluid state of atomic ^6Li in a magnetic trap. *Physical Review A*, 56(6):4864, December 1997. 3.1

[HLD10] H. Hu, X.-J. Liu, and P.D. Drummond. Universal thermodynamics of a strongly interacting Fermi gas: theory versus experiment. *New Journal of Physics*, 12(6):063038, June 2010. 6.3, 6.4

[HLR94] B.L. Hammond, W.A. Jr Lester, and P.J. Reynolds. *Monte Carlo Methods in Ab Initio Quantum Chemistry*. World Scientific, Singapore, 1994. 2.4

[HNUM10] M. Horikoshi, S. Nakajima, M. Ueda, and T. Mukaiyama. Measurement of universal thermodynamic functions for a unitary Fermi gas. *Science (New York, N.Y.)*, 327(5964):442, January 2010. 6.1, 6.3

[Ho04] T.-L. Ho. Universal Thermodynamics of Degenerate Quantum Gases in the Unitarity Limit. *Physical Review Letters*, 92(9):090402, March 2004. 6.3

[HPS72] P.G. Hoel, S.C. Port, and C.J. Stone. *Introduction to stochastic processes*. Houghton Mifflin Company, 1972. 2.2

[HS05] N. Hatano and M. Suzuki. *Finding Exponential Product Formulas of Higher Orders*, volume 679, page 37. Springer, June 2005. 2.4

[HTL+10] H. Hu, E. Taylor, X.-J. Liu, S. Stringari, and A. Griffin. Second sound and the density response function in uniform superfluid atomic gases. *New Journal of Physics*, 12(4):043040, April 2010. 6.2, 6.3

[HY57] K. Huang and C. Yang. Quantum-Mechanical Many-Body Problem with Hard-Sphere Interaction. *Physical Review*, 105(3):767, February 1957. 1.1, 1.4, 3.2

[HZ08] L. He and P. Zhuang. Phase diagram of a cold polarized Fermi gas in two dimensions. *Physical Review A*, 78(3):033613, 2008. 4.1

[IAS+98] S. Inouye, M.R. Andrews, J. Stenger, H.-J. Miesner, D.M. Stamper-Kurn, and W Ketterle. Observation of Feshbach resonances in a Bose-Einstein condensate. *Nature*, 392:151, 1998. 1.3

[IS08] M. Iskin and C. Sá De Melo. Fermi-Fermi mixtures in the strong-attraction limit. *Physical Review A*, 77(1):013625, January 2008. 5.1

[JCL+07] J. Joseph, B. Clancy, L. Luo, J. Kinast, A. Turlapov, and J. Thomas. Measurement of Sound Velocity in a Fermi Gas near a Feshbach Resonance. *Physical Review Letters*, 98(17):170401, April 2007. 6.1

[JLC+09] G.-B. Jo, Y.-R. Lee, J.-H. Choi, C.A. Christensen, T.H. Kim, J.H. Thywissen, D.E. Pritchard, and W. Ketterle. Itinerant ferromagnetism in a Fermi gas of ultracold atoms. *Science (New York, N.Y.)*, 325(5947):1521, September 2009. 3.1, 4.1

[Kal62] M. Kalos. Monte Carlo Calculations of the Ground State of Three- and Four-Body Nuclei. *Physical Review*, 128(4):1791, November 1962. 2

[Kal70] M. Kalos. Energy of a Boson Fluid with Lennard-Jones Potentials. *Physical Review A*, 2(1):250, July 1970. 2

[Kha65] I.M. Khalatnikov. *An Introduction to the Theory of Superfluidity.* W. A. Benjamin, New York, 1965. 1.1, 6.1, 6.2

[KLV74] M. Kalos, D. Levesque, and L. Verlet. Helium at zero temperature with hard-sphere and other forces. *Physical Review A*, 9(5):2178, May 1974. 2.5

[Kos96] I. Kosztin. Introduction to the diffusion Monte Carlo method. *American Journal of Physics*, 64(5):633, February 1996. 2.4

[KW08] M.H. Kalos and P.A. Whitlock. *Monte Carlo Methods.* Wiley-VCH, 2 edition, 2008. 2.1, 2.1

[KZ08] W. Ketterle and M.W. Zwierlein. Making, probing and understanding ultracold Fermi gases. *Rivista Del Nuovo Cimento*, 31(05-06):247, January 2008. 1.1

[Lan41] L. Landau. Theory of the superfluidity of Helium II. *J. Phys. USSR*, 5:71, 1941. 6.1, 6.2

[Lan57] L.D. Landau. Theory of Fermi-Liquids. *Sov. Phys. JETP*, 3:920, 1957. 2.7.2

[Leg80] A.J. Leggett. *Diatomic molecules and cooper pairs*, page 13. Springer-Verlag, Berlin, 1980. 1.3, 2.7.3

[Leg01] A. Leggett. Bose-Einstein condensation in the alkali gases: Some fundamental concepts. *Reviews of Modern Physics*, 73(2):307, April 2001. 1.1

[LL87] L.D. Landau and E.M. Lifshitz. *Course of Theoretical Physics, vol.6 - Fluid Mechanics*. Pergamon Press, 2nd edition, 1987. 6.1

[LRGS06] C. Lobo, A. Recati, S. Giorgini, and S. Stringari. Normal State of a Polarized Fermi Gas at Unitarity. *Physical Review Letters*, 97(20):200403, November 2006. 3.1, 3.3, 5.1, 5.2

[LSKC81] M. Lee, K. Schmidt, M. Kalos, and G. Chester. Green's Function Monte Carlo Method for Liquid ^3He. *Physical Review Letters*, 46(11):728, March 1981. 2.6

[LTBP09] L. LeBlanc, J. Thywissen, A. Burkov, and A. Paramekanti. Repulsive Fermi gas in a harmonic trap: Ferromagnetism and spin textures. *Physical Review A*, 80(1):013607, July 2009. 3.1

[LY57] T. Lee and C. Yang. Many-Body Problem in Quantum Mechanics and Quantum Statistical Mechanics. *Physical Review*, 105(3):1119, February 1957. 3.2

[LZC01] C. Lin, F. Zong, and D. Ceperley. Twist-averaged boundary conditions in continuum quantum Monte Carlo algorithms. *Physical Review E*, 64(1):016702, June 2001. 2.9, 3.2

[MC09] C. Mora and Y. Castin. Ground State Energy of the Two-Dimensional Weakly Interacting Bose Gas: First Correction Beyond Bogoliubov Theory. *Physical Review Letters*, 102(18):180404, May 2009. 4.3.3, 4.5

[MC10] C. Mora and F. Chevy. Normal Phase of an Imbalanced Fermi Gas. *Physical Review Letters*, 104(23):230402, June 2010. 3.3

[McM65] W. McMillan. Ground State of Liquid ^4He. *Physical Review*, 138(2A):A442, April 1965. 2, 2.3, 2.7

[Miy83] K. Miyake. Fermi Liquid Theory of Dilute Submonolayer ^3He on Thin ^4HeII Film. *Progress of Theoretical Physics*, 69(6):1794, June 1983. 4.1, 4.3.1, 4.5, 4.5

[MKv09] R. Meppelink, S. Koller, and P. van Der Straten. Sound propagation in a Bose-Einstein condensate at finite temperatures. *Physical Review A*, 80(4):043605, October 2009. 6.1

[MMT10] K. Martiyanov, V. Makhalov, and A. Turlapov. Observation of a Two-Dimensional Fermi Gas of Atoms. *Physical Review Letters*, 105(3):030404, July 2010. 4.1

[MRR+53] N. Metropolis, A.W. Rosenbluth, M.N. Rosenbluth, A.H. Teller, and E. Teller. Equation of State Calculations by Fast Computing Machines. *The Journal of Chemical Physics*, 21(6):1087, 1953. 2, 2.2

[MT05] J.-P. Martikainen and P. Törmä. Quasi-Two-Dimensional Superfluid Fermionic Gases. *Physical Review Letters*, 95(17):170407, October 2005. 4.1

[MU49] N. Metropolis and S. Ulam. The Monte Carlo Method. *Journal of the American Statistical Association*, 44(247):335, 1949. 2

[MVA95] A.J. Moerdijk, B.J. Verhaar, and A. Axelsson. Resonances in ultracold collisions of ^6Li, ^7Li, and ^{23}Na. *Physical Review A*, 51(6):4852, June 1995. 1.3

[NG98] T. Nikuni and A. Griffin. Hydrodynamic modes and pulse propagation in a cylindrical Bose gas above the Bose-Einstein transition. *Physical Review A*, 58(5):4044, November 1998. 6.4

[NNCS10] N. Navon, S. Nascimbène, F. Chevy, and C. Salomon. The Equation of State of a Low-Temperature Fermi Gas with Tunable Interactions. *Science (New York, N.Y.)*, 328(5979):729, April 2010. 4.1

[NNJ+10] S. Nascimbène, N. Navon, K.J. Jiang, F. Chevy, and C. Salomon. Exploring the thermodynamics of a universal Fermi gas. *Nature*, 463(7284):1057, February 2010. 3.1, 6.3, 6.3, 6.4

[NP89] P. Noziéres and D. Pines. *The Theory of Quantum Liquids*. Addison-Wesley, Reading, MA, 1989. 2.7.2

[OP01] M. Olshanii and L. Pricoupenko. Rigorous Approach to the Problem of Ultraviolet Divergencies in Dilute Bose Gases. *Physical Review Letters*, 88(1):010402, December 2001. 1.1

[PBGT10] S. Pilati, G. Bertaina, S. Giorgini, and M. Troyer. Itinerant Ferromagnetism of a Repulsive Atomic Fermi Gas: A Quantum Monte Carlo Study. *Physical Review Letters*, 105(3):030405, July 2010. 1, 3

[PBS03] D. Petrov, M. Baranov, and G Shlyapnikov. Superfluid transition in quasi-two-dimensional Fermi gases. *Physical Review A*, 67(3):031601, March 2003. 4.1, 4.3.3, 4.5

[PG08] S. Pilati and S. Giorgini. Phase Separation in a Polarized Fermi Gas at Zero Temperature. *Physical Review Letters*, 100(3):030401, January 2008. 2.7.2, 2.7.4, 4.5, 5.1, 5.2, 5.2, 5.2, 5.2, 5.4, 5.5

[Pit61] L.P. Pitaevskii. Vortex lines in an imperfect Bose gas. *Sov. Phys. JETP*, 13(2):451, 1961. 1.1

[PLK+06] G.B. Partridge, W. Li, R.I. Kamar, Y.-A. Liao, and R.G. Hulet. Pairing and phase separation in a polarized Fermi gas. *Science (New York, N.Y.)*, 311(5760):503, January 2006. 5.1

[PLL+06] G. Partridge, W. Li, Y. Liao, R. Hulet, M. Haque, and H. Stoof. Deformation of a Trapped Fermi Gas with Unequal Spin Populations. *Physical Review Letters*, 97(19):190407, November 2006. 5.1

[PRB78] C. Pangali, M. Rao, and B.J. Berne. On a novel Monte Carlo scheme for simulating water and aqueous solutions. *Chemical Physics Letters*, 55(3):413, May 1978. 2.3.1

[PS01] D.S. Petrov and G.V. Shlyapnikov. Interatomic collisions in a tightly confined Bose gas. *Physical Review A*, 64(1):012706, June 2001. 4.2, 4.6

[PS02] C. Pethick and H. Smith. *Bose-Einstein Condensation in Dilute Gases*. Cambridge University Press, Cambridge, U.K., 2002. 1.1

[PS03] L. Pitaevskii and S. Stringari. *Bose-Einstein Condensation*. Oxford University Press, Oxford, 2003. 1.1

[PS06] P. Pieri and G. Strinati. Trapped Fermions with Density Imbalance in the Bose-Einstein Condensate Limit. *Physical Review Letters*, 96(15):150404, April 2006. 5.1

[PS08] N. Prokof'ev and B. Svistunov. Fermi-polaron problem: Diagrammatic Monte Carlo method for divergent sign-alternating series. *Physical Review B*, 77(2):020408(R), January 2008. 3.1, 5.2, 5.2

[PTVF92] W.A. Press, S.A. Teukolsky, W.T. Vettering, and B P. Flannery. *Numerical Recipes in Fortran*. Cambridge University Press, Cambridge, 2nd edition, 1992. 2.1, 2.1, 2.1, 2.3

[RDF78] P J. Rossky, J.D. Doll, and H.L. Friedman. Brownian dynamics as smart Monte Carlo simulation. *The Journal of Chemical Physics*, 69(10):4628, 1978. 2.3.1

[RDS89] M. Randeria, J.-M. Duan, and L.-Y. Shieh. Bound states, Cooper pairing, and Bose condensation in two dimensions. *Physical Review Letters*, 62(9):981, February 1989. 4.1, 4.5, 4.5

[RDS90] M. Randeria, J.-M. Duan, and L.-Y. Shieh. Superconductivity in a two-dimensional Fermi gas: Evolution from Cooper pairing to Bose condensation. *Physical Review B*, 41(1):327, January 1990. 4.1, 4.3.1, 4.5, 4.5

[Rey82] P.J. Reynolds. Fixed-node quantum Monte Carlo for molecules. *The Journal of Chemical Physics*, 77(11):5593, 1982. 2, 2.4, 2.6, 3.2, B

[RGJ04] C.A. Regal, M. Greiner, and D.S. Jin. Observation of Resonance Condensation of Fermionic Atom Pairs. *Physical Review Letters*, 92(4):040403, January 2004. 1.1

[RLS08] A. Recati, C. Lobo, and S. Stringari. Role of interactions in spin-polarized atomic Fermi gases at unitarity. *Physical Review A*, 78(2):023633, August 2008. 5.1, 5.2

[SBC02] A. Sarsa, J. Boronat, and J. Casulleras. Quadratic diffusion Monte Carlo and pure estimators for atoms. *The Journal of Chemical Physics*, 116(14):5956, 2002. 2.5.1, 2.6, 2.8, B

[Sor05] S. Sorella. Wave function optimization in the variational Monte Carlo method. *Physical Review B*, 71(24):241103, June 2005. 2.3

[SPPR00] L. Salasnich, B. Pozzi, A. Parola, and L. Reatto. Thermodynamics of multi-component Fermi vapours. *Journal of Physics B: Atomic, Molecular and Optical Physics*, 33(19):3943, 2000. 3.1

[SSSK08a] Y.-I. Shin, A. Schirotzek, C. Schunck, and W. Ketterle. Realization of a Strongly Interacting Bose-Fermi Mixture from a Two-Component Fermi Gas. *Physical Review Letters*, 101(7):070404, August 2008. 5.1, 5.4, 5.4

[SSSK08b] Y.-I Shin, C.H. Schunck, A. Schirotzek, and W. Ketterle. Phase diagram of a two-component Fermi gas with resonant interactions. *Nature*, 451(7179):689, February 2008. 5.1, 5.4, 5.4

[Sto33] E.C. Stoner. LXXX. Atomic moments in ferromagnetic metals and alloys with non-ferromagnetic elements. *Philosophical Magazine Series 7*, 15(101):1018, 1933. 3.1

[SWSZ09] A. Schirotzek, C.-H. Wu, A. Sommer, and M. Zwierlein. Observation of Fermi Polarons in a Tunable Fermi Liquid of Ultracold Atoms. *Physical Review Letters*, 102(23):230402, June 2009. 3.1

[SY02] T. Sogo and H. Yabu. Collective ferromagnetism in two-component Fermi-degenerate gas trapped in a finite potential. *Physical Review A*, 66(4):043611, October 2002. 3.1

[SZS+06] Y. Shin, M. Zwierlein, C. Schunck, A. Schirotzek, and W. Ketterle. Observation of Phase Separation in a Strongly Interacting Imbalanced Fermi Gas. *Physical Review Letters*, 97(3):030401, July 2006. 3.1, 5.1

[Tan08a] S. Tan. Energetics of a strongly correlated Fermi gas. *Annals of Physics*, 323(12):2952, December 2008. 1.4, 4.5

[Tan08b] S. Tan. Large momentum part of a strongly correlated Fermi gas. *Annals of Physics*, 323(12):2971, December 2008. 1.4, 4.5

[TG05] E. Taylor and A. Griffin. Two-fluid hydrodynamic modes in a trapped superfluid gas. *Physical Review A*, 72(5):053630, November 2005. 6.1

[TGO07] E. Taylor, A. Griffin, and Y. Ohashi. Spin-polarized Fermi superfluids as Bose-Fermi mixtures. *Physical Review A*, 76(2):023614, August 2007. 5.1

[THL+09] E. Taylor, H. Hu, X.-J. Liu, L. Pitaevskii, A. Griffin, and S. Stringari. First and second sound in a strongly interacting Fermi gas. *Physical Review A*, 80(5):053601, November 2009. 6.1, 6.4

[THLG08] E. Taylor, H. Hu, X.-J. Liu, and A. Griffin. Variational theory of two-fluid hydrodynamic modes at unitarity. *Physical Review A*, 77(3):033608, March 2008. 6.3, 6.4

[TTHK99] E. Timmermans, P. Tommasini, M. Hussein, and A. Kerman. Feshbach resonances in atomic Bose–Einstein condensates. *Physics Reports*, 315(1-3):199, July 1999. 1.2

[TW05] M. Troyer and U.-J. Wiese. Computational Complexity and Fundamental Limitations to Fermionic Quantum Monte Carlo Simulations. *Physical Review Letters*, 94(17):170201, May 2005. 2.6

[UNR93] C.J. Umrigar, M.P. Nightingale, and K.J. Runge. A diffusion Monte Carlo algorithm with very small time-step errors. *The Journal of Chemical Physics*, 99(4):2865, 1993. 2.5, 2.6, B

[VR86] J. Vrbik and S. Rothstein. Quadratic accuracy diffusion Monte Carlo. *Journal of Computational Physics*, 63(1):130, March 1986. 2.5.1

[WC10] F. Werner and Y. Castin. Exact relations for quantum-mechanical few-body and many-body problems with short-range interactions in two and three dimensions. *arxiv*, 1001.0774, January 2010. 1.4, 4.5

[Yan62] C. Yang. Concept of Off-Diagonal Long-Range Order and the Quantum Phases of Liquid He and of Superconductors. *Reviews of Modern Physics*, 34(4):694, October 1962. 1.2

[Zha09] H. Zhai. Correlated versus ferromagnetic state in repulsively interacting two-component Fermi gases. *Physical Review A*, 80(5):051605, November 2009. 3.1

[ZLD08a] W. Zhang, G.-D. Lin, and L.-M. Duan. BCS-BEC crossover of a quasi-two-dimensional Fermi gas: The significance of dressed molecules. *Physical Review A*, 77(6):063613, June 2008. 4.1

[ZLD08b] W. Zhang, G.-D. Lin, and L.-M. Duan. Berezinskii-Kosterlitz-Thouless transition in a trapped quasi-two-dimensional Fermi gas near a Feshbach resonance. *Physical Review A*, 78(4):043617, October 2008. 4.1

[ZSS+04] M.W. Zwierlein, C.A. Stan, C.H. Schunck, S.M.F. Raupach, A.J. Kerman, and W. Ketterle. Condensation of Pairs of Fermionic Atoms near a Feshbach Resonance. *Physical Review Letters*, 92(12):120403, March 2004. 1.1

[ZSSK06a] M.W. Zwierlein, A. Schirotzek, C.H. Schunck, and W. Ketterle. Fermionic superfluidity with imbalanced spin populations. *Science (New York, N.Y.)*, 311(5760):492, January 2006. 5.1

[ZSSK06b] M.W. Zwierlein, C.H. Schunck, A. Schirotzek, and W. Ketterle. Direct observation of the superfluid phase transition in ultracold Fermi gases. *Nature*, 442(7098):54, July 2006. 5.1